Astroteilchenphysik

On a prototype detector
for the radio emission from air showers
at the South Pole

DISSERTATION

zur Erlangung des Doktorgrades

Fachbereich C – Mathematik und Naturwissenschaften

Arbeitsgruppe Prof. Dr. Klaus Helbing

Dem Fachbereich Physik vorgelegt von

Jan Auffenberg

im

März 2010

Diese Dissertation kann wie folgt zitiert werden:

urn:nbn:de:hbz:468-20100923-124332-7

[http://nbn-resolving.de/urn/resolver.pl?urn=urn%3Anbn%3Ade%3Ahbz%3A468-20100923-124332-7]

Contents

Chapter 1

Introduction

As an introduction of this thesis some historically important persons for the particular field of science, comic ray physics and its detection methods, and there groundbreaking results will be sketched. Nevertheless one should never forget that science is not a chain reaction, where one element induces all the others, or is only dependent of a small number of important scientists, but a puzzle, where every new piece of knowledge is important on the way to see the whole picture, explored by a large number of scientists. However, this thesis about research and development (R&D) in astroparticle physics might rely most importantly on the work of three physicists and their experimental discoveries in particular:

- Victor F. Hess discovered from 1911 to 1912 "cosmic rays" during balloon flights. He found that the number of charged particles increases with rising altitude of his balloon and thus this "natural radiation" was presumed not to originate from the Earth but from space.

- The second experimental physicist is Pierre V. Auger. He found that cosmic radiation events on the Earth's surface are frequently coincident in time, meaning that they can be associated with a single event which happens to be cosmic particle induced. This primary cosmic particle hits a particle in the atmosphere and induces secondary particles, which themselves induce further particles, and so on. This events become known as cosmic ray induced "air shower".

- In 1965 J. V. Jelley et al. discovered that extensive air showers (EAS), initiated by high-energy cosmic rays, produce strongly pulsed radio emission at frequencies around 44 `MHz`. This was based on theories of strong Cherencov radiation of electrons and positrons by Askaryan [9].

There is a large number of possibilities to detect EAS with currently known detection techniques. A less common technique is the detection of pulsed radio signals. The large number of electromagnetic charged particles are diverted in the Earths' magnetic field and emit synchrotron radiation. If this emission is coherent, the emission of the individual particles can add up. In case of full coherence the field strength $E(\omega)$ of the emission grows with N^2 where N is the number of charged particles. The coherence is strongly frequency dependent as it is only possible at frequencies where the wavelength of the emission is at most on the order of the thickness of the air shower particles distribution. The air showers "pancake", a thin disc where all the particles of the air shower are moving through the earths' atmosphere, has typically a thickness of a few meters. Thus we are limited to frequencies not higher than ≈ 100 `MHz`. This requires a place on Earth where the electromagnetic interferences (EMI) are as small as possible in the frequency band from a few `MHz` to about 100 `MHz`. The South Pole is expected to be an ideal place with low EMI in the relevant frequency band.

In this thesis we will describe the first surface radio measurements at the South Pole to detect air showers by their radio emission. Together with the described simulations of the signal strengths detectable with a proposed test setup, this can be the fundament for prospective radio air shower detection efforts. Ultimately, this can lead to a large surface radio air shower detector as an enhancement of the IceCube observatory and becoming a multi component cosmic particle detector.

After this introduction, the thesis starts with a theoretical overview (Chapter 2) about the sources of cosmic particles, their importance in the universe, and their propagation to Earth. The properties of EAS will be discussed ending with an introduction to the synchrotron radio emission of EAS in the Earth's magnetic field.
Chapter 3 describes a selection of currently existing astroparticle detectors, starting with radio air shower detection effort of LOPES, describing the neutrino telescope, IceCube, and the radio detection efforts at the South Pole.
Chapter 4 describes our first surface radio measurements at the South Pole and their results.
In Chapter 5, our results of the measurements are discussed together with results from simulations of air shower radio emissions at the South Pole.
And, finally, Chapter 6 estimates the possibility of radio EAS detection with one exemplary test facility and motivates simulation studies of a large radio EAS array.

Chapter 2

COSMIC RAYS, NEUTRINOS, AND AIR SHOWERS

For thousands of years humans have been observing the light of stars and are asking for their place in the Universe. The nature and origin of Cosmic Rays is only a small fraction of this picture. Since the observations of Victor Hess in 1912 [25] we know that not only the light of cosmic sources reaches the Earth, but also other kinds of rays with higher energies. Of course, there was much progress on this topic during the last century, which not only revealed important answers in particle and astro physics but also new questions. The first observation of the muon, for example, was made by observations of cosmic rays (C. D. Anderson 1936 [8]). The following chapter gives a brief overview of our knowledge about cosmic ray particles in terms of their observation on Earth – or within Earth's atmosphere.

2.1   Cosmic Ray Particles as Part of the Universe

Due to our knowledge about the Universe, we are trying to formulate models and making expectations on its nature. Having a prediction or model means that we can try to make predictions for example on the cosmic ray flux. Presently the most popular model of our Universe is the Λ Cold Dark Matter model (ΛCDM) that tells us what the nature of the Universe is thought to be. Besides the known matter of the standard model, expressed as a baryonic matter density Ω_b, there is a contribution of non-baryonic cold dark matter, Ω_{dm}. Together, they are described as the total matter density Ω_M. Finally, the cosmological constant $\Lambda \neq 0$ is introduced, which can be considered as an energy term with the energy density Ω_Λ. The ΛCDM-model additionally assumes that the Universe is flat, ($\Omega_k = 0$), and the energy density parameter Ω_{total}. All Ω are in units of the critical energy density Ω_{crit} of the

Universe where the Universe is flat. Summing over the different energy densities the total density can be written as:

$$\Omega_{total} = \Omega_M + \Omega_\Lambda + \Omega_k, \tag{2.1}$$

where these parameters can be measured by experiments.

With $\Omega_{dm} \approx 0.23$ and $\Omega_\Lambda \approx 0.73$ the Universe is being filled up to 96 % with something that is unknown in origin and is not part of the standard model of particle physics. From the "Wilkinson Microwave Anisotropy Probe" (WMAP) satellite mission, the parameters for the ΛCDM model can be constrained [59], which gives a value for the baryonic matter density of $\Omega_b = 0.0444^{+0.0042}_{-0.035}$. Together with complemetary measurements from high redshift supernovae [37], X-ray gas mass fraction of galaxy clusters [5], or from weak gravitational lensing observations [12], the parameter range can be further constrained. This is illustrated in Fig. 2.1 which shows the density Ω_Λ against the matter density Ω_M as the sum of baryonic matter and cold dark matter. The remaining 4 % of the well known baryonic matter can be found all over our Universe in many different energetic states and compositions.

2.2   Cosmic Rays

A small fraction of the known standard model matter consists of gravitationally unbound particles or nuclei with high kinetic energy. The constant bombardment of the Earth with these particles is called cosmic radiation. Single events are cosmic rays (CR). The following section briefly describes the nature, possible origin, and interaction of these particles on Earth.

2.2.1   Origin of cosmic rays

The nearest source for particles hitting the Earth from outer space is the Sun. It dominates the CR energy spectrum below 10^9 eV. As "cosmic" implies radiation not coming from our solar system, we focus on particle energies above this energy. Of course, there are cosmic particles with lower energies, too, but they are still strongly influenced by the Sun.

The energy range covered by the non solar CR flux is enormous. It starts with energies of some GeV (MeV for the CR flux of the sun) and reaches up to more than 10^{20} eV for the highest energetic events observed so far [13]. While the CR flux at the lowest energies can be explained with solar flares (up to 10^{10} eV), the CR flux up to the so called "knee" at about 10^{16} eV is supposed to stem from supernova remnants or massive black holes with an accretion disc (microquasars).
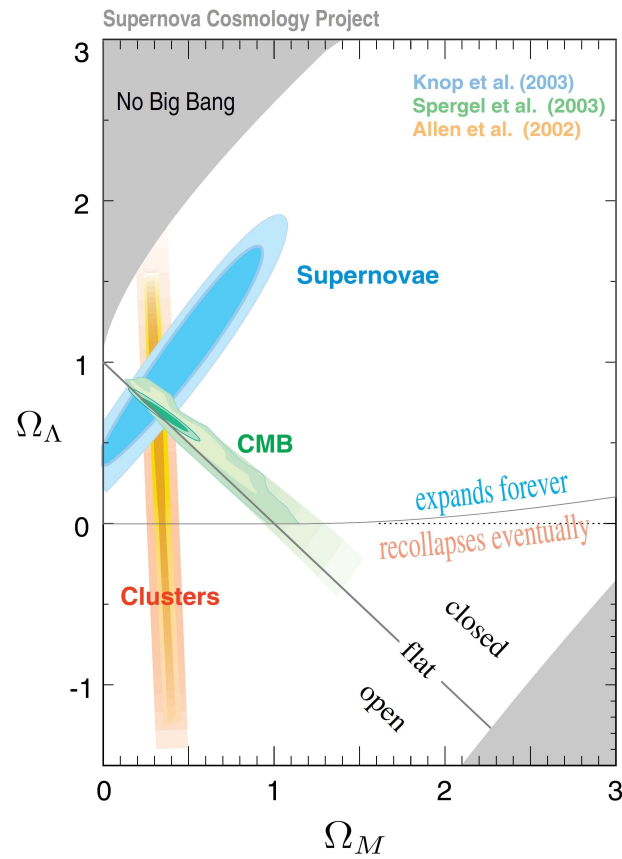
Figure 2.1: Relation of the energy densities Ω_Λ and Ω_M from various measurements [37]. With complementary measurements of the *Cosmic Microwave Background* (CMB) and supernovae the parameter space is well constrained.

Possible candidates for CRs at even higher energies are neutron stars and binary star systems or active galactic nuclei (AGNs).

At energies higher than $10^{18} - 10^{19}$ `eV` the acceleration of the particles should be extra galactic, as the gyro magnetic radius r_l exceeds the size of the galaxy itself ($100\,000$ `ly` diameter):

$$r_l = \frac{pc}{ZeB}, \tag{2.2}$$

where p is the particle's momentum, Ze the charge of the particle, and B the galactic magnetic field on the order of μ`G`.

It is hard to find a model to explain the origin of CR at the highest energies as the acceleration of particles needs more and more time, stronger potentials or more space. The more exotic class of top-down models explains ultra high energy cosmic rays (UHECR) as decay products of extremely massive particles. These massive particles are either emitted by topological defects from the early Universe, or are themselves relics from the early Universe, surviving until today. There are models using SUSY (SUper SYmmetric) predictions, nonstandard neutrinos or Lorentz invariance, as well. All these models use the assumption to have the high energy source near by the Earth as they are relics from the early Universe, and thus are reacting due to their short path length to the Earth less probably with the cosmic microwave background (CMB) or interstellar matter.

More common theories are the so called bottom-up scenarios trying to use the standard model to explain UHECRs. They suggest violent classic extra galactic astrophysical sources to be producers and accelerators of the bombardment of particles, such as gamma ray bursts or AGN. Considering AGNs as sources of UHECRs, one can search for anisotropies in the CRs' arrival directions and try to correlate these with known AGN locations, as was done with data from the AUGER experiment [1]. AGNs are discussed in more detail in Section 2.2.5.

2.2.2   Acceleration mechanisms of cosmic rays

Where the top-down models do not need acceleration mechanisms, the bottom-up scenarios have to explain both, the acceleration of particles to high energies and the propagation mechanisms through the Universe as the sources are expected to be far away.

In 1949, Fermi postulated a method to accelerate particles to high energies following a power law in the energy spectrum [18]. This so called "second order Fermi acceleration" relates to the idea of energy gained during the motion of a charged particle in the presence of randomly moving "magnetic mirrors" in interstellar clouds. If the

magnetic mirror is moving toward the particle, the particle will end up with increased energy upon reflection. The opposite holds if the mirror is receding. Fermi figured out that the average gain per collision with the shock front is

$$\left\langle \frac{\Delta E}{E} \right\rangle = \frac{8}{3} \left(\frac{V}{c} \right)^2, \tag{2.3}$$

where V is the velocity of the mirror. The quadratic term $\left(\frac{V}{c} \right)^2$ is the reason for the name *second* order Fermi acceleration. Due to the low velocity of interstellar magnetic clouds, this acceleration process is slow. This leads to unrealistic long times to accelerate particles to very high energies.

However there is a second acceleration mechanism, the "first order Fermi acceleration". It follows the average gain in energy with a first order term $\left(\frac{V}{c} \right)$:

$$\left\langle \frac{\Delta E}{E} \right\rangle = \frac{4}{3} \left(\frac{V}{c} \right). \tag{2.4}$$

The mechanism is based on acceleration at shock fronts for example from SNRs (**S**uper **N**ova **R**emnants). The idea is that isotropically distributed particles are accelerated in every cycle through the shock front with statistically the same amount $\frac{\Delta E}{E}$. When they are in front of the shock front (upstream) they get first accelerated in the part of the shock front with high velocity. Then, every single particle will be multiple scattered in the turbulent back part of the shock front with lower velocity and the particles get isotropized again. In the downstream case the situation is quite similar. Now the particles are isotropic behind the shock front and can get accelerated while moving toward the shock front [69]. This mechanism can not explain the origin of highest energetic flux, as it is strongly limited in the maximum energy by

$$E_{max} = Ze\beta_s BtV_s, \tag{2.5}$$

where $\beta_s = \frac{V_s}{c}$ and V_s is the velocity of the shock front, Z is the number of charges, and e is the electron charge. That makes it difficult to explain particle energies above 10^{17} eV as the magnetic field strength B, the propagation time t or the velocity V_s would have to be unrealistically large for SNRs. To accelerate iron to 10^{17} eV for example, one needs nT magnetic field strength for 1000 y with 98% β_s what are typical values for SNRs. It is evident that both mechanisms describe general possibilities how to accelerate particles in the Universe.

2.2.3 Propagation mechanism

Between the Earth and the source, the CRs have to propagate through our galaxy. The isotropy in direction of the galactic CRs measured on Earth implies that

they are not immediately escaping from our galaxy or the sources are isotropic distributed themselves. Our galaxy contains a "galactic" magnetic field with different components, a large-scale regular and a chaotic irregular component, known from observations in our as well as other galaxies [11]. Accelerated particles injected into our galaxy undergo an interaction with this magnetic field. The gyro-radii of high energetic particles above 10^{18} `eV` are larger than the extension of our galaxy, which is about 30 `kpc` in diameter. The propagation is a diffusive one and the mean free path length is much larger than the size of our galaxy, which leads to residence times of about 10^7 years for particles with 10^{18} `eV` energy. With models such as the leaky box model [14], the propagation of the CRs in our galaxy is described and is an important part to reproduce the observed CR flux at Earth.

Several aspects have to be considered when the CR particles propagate, which finally determines the measured composition and fluxes. There are the interactions with magnetic and also electric fields that can lead to re-acceleration. Furthermore the particles lose energy due to ionization and inelastic scattering. The composition will change after spallation or radioactive decay of the CRs. It is derived from observation of the boron to carbon ratio that higher energetic particles traverse less intergalactic matter and thus escape earlier from the galaxy. That is an example showing that the measurement of the composition of CRs can help to understand the processes involved during propagation.

2.2.4   Energy spectrum of cosmic rays

One of the most important experimental quantities to test the theories of acceleration, propagation, and origin of the CRs is the energy spectrum (Fig. 2.2) of the CRs and their composition.

The energy spectrum of the CRs is almost featureless. Extending from 10^9 `eV` up to 10^{20} `eV` the spectrum follows a power law $E^{-\gamma}$ with a spectral index of $\gamma \approx 3.0$. In order to point out deviations from the power law fall off, the flux shown in Fig. 2.2 has been multiplied by $E^{2.5}$. A power law is expected in the case of a stochastic acceleration, such as those proposed by Fermi which are motivated in Section 2.2.2. However, the CR spectrum has some features which are the basis of an ongoing physics discussions. Around 3×10^{15}`eV` [64] there is the so called "knee" where the CR spectrum gets steeper ($\gamma = 3.1$). This change in the spectral index might be due to changing acceleration mechanisms, as discussed in Section 2.2.1, when the highest possible acceleration energy E_{max} of SNRs is reached. Furthermore, the escape probability in the galaxy for CR increases with higher energy which leads to a lower CR flux. Some theories use propagation models of CRs in our galaxy to
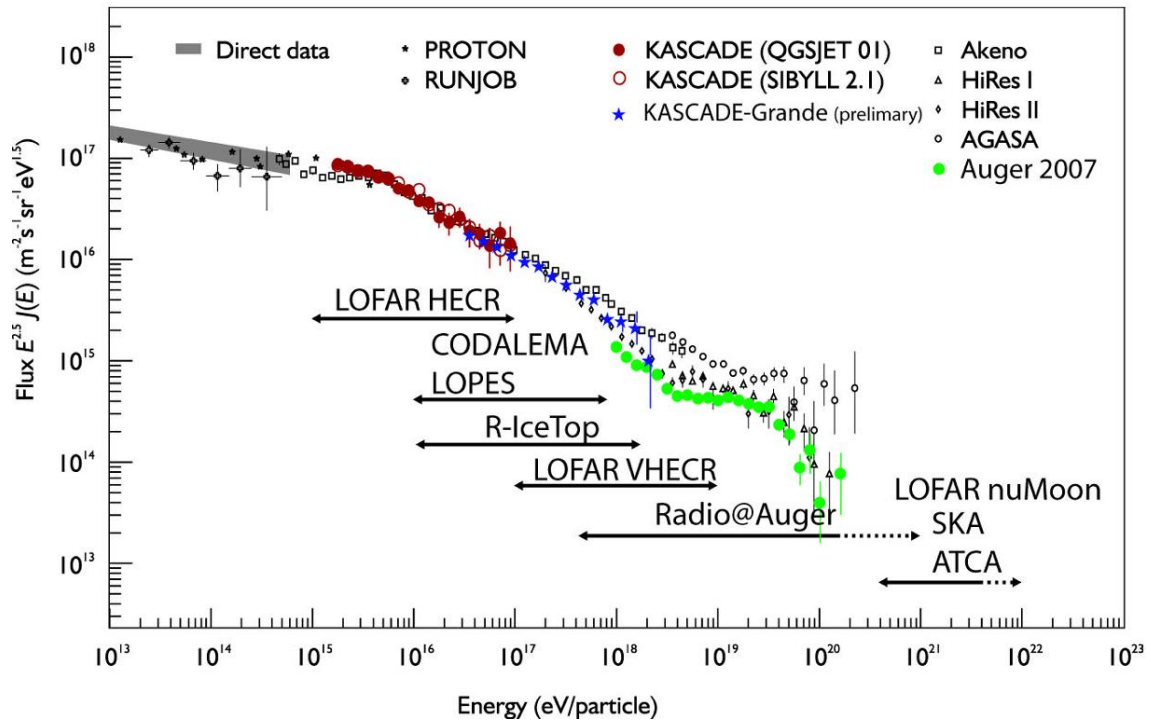
Figure 2.2: The flux spectrum of CRs. Possible detection ranges in energy for proposed experiments based onto radio detection technique are plotted with black arrows. For better presentation of the features the spectrum is weighted with $E^{2.5}$.

explain the change in the spectral index at the knee, too [55]. The steepening at the (first) "knee" could be a charge number, Z, dependent effect due to magnetic fields. As the energy E_{max} for Fermi shock acceleration is proportional to $Z \cdot B \cdot L$ where B is the magnetic field strength in the acceleration region, and L the Larmor radius, E_{max} is proportional to Z. This would lead to a change of the composition of the CRs to higher Z with increasing energy. Such a change of the composition in the CR flux around the "knee" has been observed by the KASCADE experiment [63]. There might be also a second steepening of the spectral index around 10^{17}eV called the "second knee" [48]. This region requires more experimental investigation in order to learn more about its origin. KASCADE-Grande, IceTop and other experiments will help to clarify the characteristics of this energy region in the near future.

The next feature at 4×10^{18}eV is called the "ankle". The experimental evidence is less strong than at the knee as the flux at these energies is already very low and needs extremely large detectors such as the Pierre Auger Observatory. However, the spectral index seems to decrease at this point. It is assumed that the extragalactic component starts to dominate the flux of particles at this point and the galactic component dies out, due to missing acceleration mechanisms in our galaxy at these energies.

The last feature of the CR energy spectrum is the overall cut-off at highest energies, which was already predicted by Greisen [20], Zatsepin, and Kuz'min [67], the so-called GZK-effect. This will be discussed together with direct sources for cosmic particles in the following Section.

2.2.5   UHECR sources

Whereas the classical definition of comic rays is the charged part of comic particles based on Hess's observations, neutrinos and gamma rays are also considered part of ultra high energy CRs (UHECR) in this section. Several theoretical models for sources will be discussed.

Where the charged CRs are explored by a large number of different experiments in space, in air, and on the ground and the gamma ray flux is explored up to several `TeV`, the cosmic neutrino flux is still to a high extent unexplored. The first and currently only established cosmic neutrino source – Supernova SN1987A – was detected with Kamiokande II, IMB and Baksan. The main problems when measuring cosmic neutrinos is the low interaction probability with matter at low energy but also the huge background from neutrinos induced by extensive air showers discussed in Section 2.3.
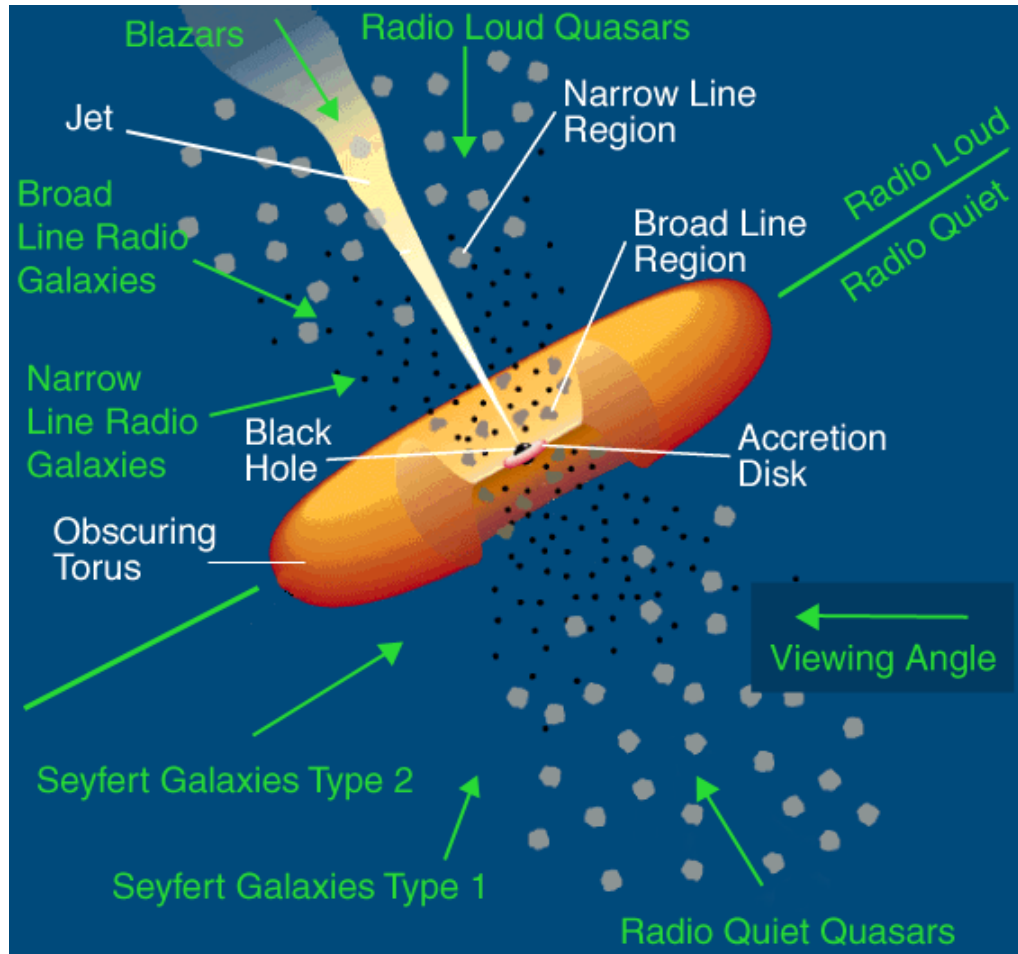
Figure 2.3: Unified model of an AGN [74]. Depending on the observer's position the AGN is classified as different cosmological objects such as galaxies with broad emission lines (Seyfert), blazars, or quasars.

Active Galactic Nuclei

The AGN model is a unified model for a number of cosmological observations. It includes Seyfert galaxies, blazars, and quasars [46]. AGNs are spiral galaxies with a super massive black hole at the center ($10^7 - 10^9$ solar masses), which accretes matter from its host galaxy. First order Fermi acceleration (Sec. 2.2.2) is a possible mechanism to produce UHECRs in jets built out in the AGN, which are created perpendicular to the accretion disc.

Figure 2.3 shows a simplified illustration of an Active Galactic Nucleus. Depending on the orientation of the accretion disc to the observer, the spectrum of the AGN will show various prominent features. If the accretion disc is observed edge-on all visible light is usually absorbed in molecular clouds in and around the disc, and a
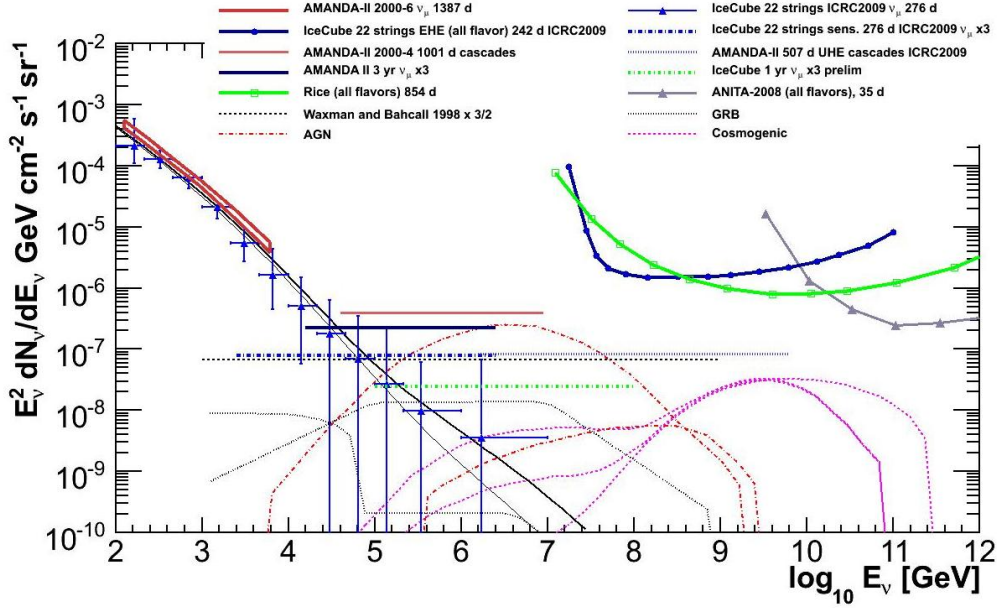
Figure 2.4: Measured neutrino atmospheric neutrino fluxes and flux limits from different experiments are shown together with a number of models for astrophysical neutrinos [38].

strong radio source with no optical counterpart is measured. If the AGN is observed in the direction of the jet, a very luminous object with high variability, a blazar, is seen. As the light of blazars is to a high degree polarized, theories using synchrotron mechanisms in a magnetic field of the jets are preferred to explain the photon emission.

As AGNs are first order Fermi accelerators and photon sources, it is natural to presume AGNs to be UHE neutrino sources. Similar to the GZK mechanism, described in Section 2.2.5, $p + \gamma$ collisions can produce a Δ resonance that decays into pions and neutrons (cf. Eq. 2.10). Of course, also direct hadronic jets can be induced by $p + \gamma$ or *nucleus + nucleus* (e.g. $p + p$) collisions:

$$\gamma + p \rightarrow \Delta^+_{1232} \quad \rightarrow \quad n + \pi^+ \tag{2.6}$$

$$\rightarrow \quad p + \pi^0 \tag{2.7}$$

$$\gamma + p \quad \rightarrow \quad n_+ \cdot \pi^+ + n_- \cdot \pi^- + n_0 \cdot \pi^0 + \dots \tag{2.8}$$

$$nucleus + nucleus \quad \rightarrow \quad hadrons, \tag{2.9}$$

where n_-, n_+, and n_0 indicate the number of produced pions. In the following, pion and neutron decay produce neutrinos (Eq. 2.12 and 2.14). One of the first predictions for the neutrino flux from AGNs was derived in 1991 by Steckter et al. [60] assuming a hidden-core model where all hadronic energy is transformed into neutrinos, and the

AGN can thus only be observed in neutrinos. A compilation of some neutrino flux predictions together with experimental limits and measured atmospheric neutrino fluxes is shown in Fig. 2.4. The dashed curve labeled as "AGN" is a model prediction for Blazars [61].

Gamma-ray bursts

A Gamma-ray Burst (GRB) is a sudden, very short (from milliseconds up to a few seconds) and very intense flash of gamma-rays. They where first observed in the late 1960s by the Vela military satellites monitoring the Nuclear Test Ban Treaty [40]. It was found that GRBs are accompanied by an afterglow in the X-ray, optical, and radio band and are isotropically distributed in space. Analysis of the afterglow have shown that they have high redshifts. With luminosities of 10^{52} `erg` to 10^{54} `erg` GRBs belong to most energetic phenomena ever observed.

It is still under discussion what the cause of GRBs is. Candidates include collapses of massive stars with high rotation frequency [47], millisecond proto-magnetars [62], mergers of neutron star binaries, or black hole-neutron star systems [32]. The short time scales of the burst limit the possible extension to a sphere of $c\Delta t \approx 100$ `km` $-$ 1000 `km` diameter. In this region a so called "fireball" is expected (Fig. 2.5) [48]. The fireball model can explain the γ spectrum of GRBs via synchrotron radiation of electrons and positrons from pair production (Eq. 2.15). In addition it predicts highly energetic CRs due to first order Fermi acceleration in the interstellar medium of up to 10^{20} `eV`. The accelerated protons can again produce Δ_{1232}^{+} and decay into neutrinos as described in the reactions 2.10-2.14. Thus the fireball model predicts GRBs to be also UHE neutrino and CR sources.

GZK effect

The Cosmic Microwave Background (CMB) consists of photons (γ_{CMB}) with the spectrum of a black body radiator with a temperature of 2.7 `K` and fill the universe with an isotropic background radiation, first measured by Penzias & Wilson [54]. It is a relict from the early Universe, where the Universe got transparent for electromagnetic emission [6]. Kenneth Greisen, Vadim Kuz'min and Georgiy Zatsepin predicted that CR protons with energies above the threshold energy of $5 \cdot 10^{19}$ `eV` would interact with CMB photons to produce pions via the Δ resonance [20] which would lead to a cutoff in the CR spectrum:

$$\gamma_{CMB} + p \rightarrow \Delta_{1232}^{+} \quad \rightarrow \quad n + \pi^{+} \tag{2.10}$$

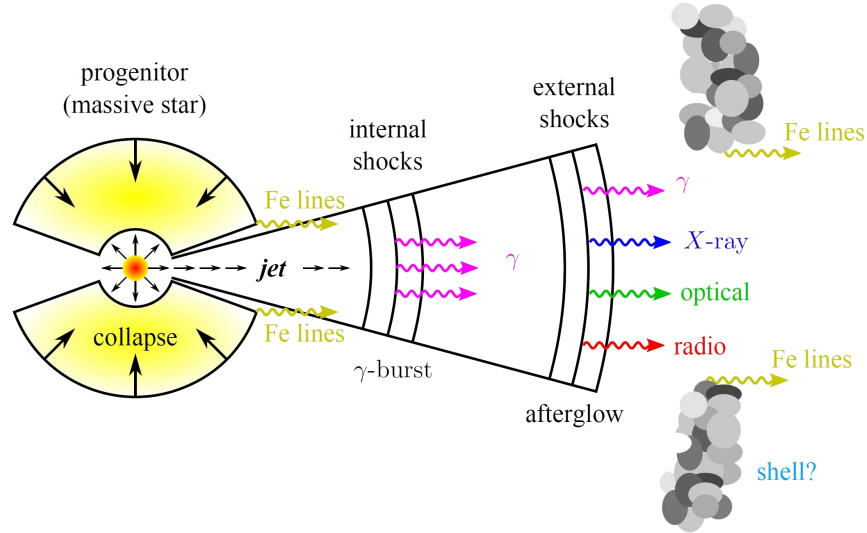$$\rightarrow \quad p + \pi^{0}, \tag{2.11}$$
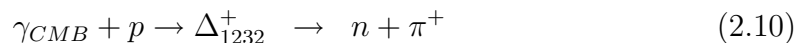
Figure 2.5: Schematic view of the fireball model [49]. The model can explain the γ spectrum and predicts GRBs to be a UHE neutrino and UHECR source.

where the π^+ and π^0 decay after a very short time ($2.6 \cdot 10^{-8}$ s or $8.4 \cdot 10^{-17}$ s) to a positron and neutrino pair or a pair of photons:

$$\pi^+ \rightarrow e^+ + \nu_e + \overline{\nu_\mu} \tag{2.12}$$

$$\pi^0 \rightarrow \gamma + \gamma, \tag{2.13}$$

and the neutron decays in a leptonic part, too:

$$n \rightarrow p + e + \overline{\nu_e}. \tag{2.14}$$

As the neutrinos from the pion and neutrino decay are not part of the GZK theory, they are often not called "GZK-neutrinos" but "cosmogenic neutrinos". However, the GZK mechanism is a source for high energy νs and γs. Detection of this cosmogenic neutrino flux could lead to a strong argument for "bottom up" models, together with the cutoff in the CR flux itself. The Pierre Auger observatory measured, there is indications that the highest energy CR are not protons but heavier nuclei [2]. This would lead too viewer neutrinos, as iron has to be 56 times higher in energy to allow a single nucleus produce the Δ resonance with γ_{CMB}. In addition photodisintegration with CMB photons would lead to daughter nuclei with lower energy without producing neutrinos leading to a cutoff. Of course, another explanation for the cutoff but GZK mechanism could be die out of acceleration mechanisms. Nevertheless the cosmic neutrino flux produced by the highest energy CRs, is sometimes called the "guaranteed neutrino flux". Figure 2.4 shows a flux prediction of

the cosmogenic neutrino flux induced by the GZK effect as derived by Engel, Seckel and Stanev [16]. The detection of this small neutrino fluxes at energies up to 10^{20} `eV` requires detectors with very large effective areas. Experiments like RICE (Section 3.3) and ANITA (Section 3.4) have set flux limits in this energy region.

2.3 Extensive air showers

After discussing the origin of CRs we want to discuss the interaction with the Earth's atmosphere. Starting point is a particle with a high enough cross section to react with the surrounding nuclei and high enough energy to create secondary particles [1]. When a high energy particle reaches the atmosphere, the atmosphere can be seen as a (inhomogeneous) calorimeter in a fixed target experiment. After the particle has traversed an energy and individual particle type-dependent mean atmospheric depth, the air shower primary interacts with a nucleus of the atmosphere and initiates a cascade of particle reactions producing secondary particles which themselves initiate further sub-cascades. The leading particle front propagates through the atmosphere with almost the (vacuum) speed of light, while at the same time evolving to a maximum in particle number and then diminishing again. There are in general three components describing a CR induced air shower:

- The electromagnetic part, e^+, e^-, and γ, which has $\approx 95\%$ of the energy,

- The muonic part, μ^+, μ^-, with $\approx 4\%$ of the energy,

- The hadronic part, mostly π^+, π^-, π^0, with $\approx 1\%$ of the energy,

where the energy fraction of the components varies from shower to shower due to its primary particle, energy, arrival angle, and statistical fluctuations.
An important property of the air shower is that the shower particles remain concentrated in a thin "pancake" of only a few meters thickness. The lateral extent of the pancake is mostly due to multiple scattering of the particles and varies for the different components in the air shower. The cascade particles arriving at the ground can then be measured by particle detector arrays with increasing effective collecting areas for increasing primary particle energy. Figure 2.6 gives a schematic view of an extensive air shower. In the following subsections we will briefly discuss the components of extensive air showers (EAS).

---

[1]Of course most of the particles are hadrons, but also photons, leptons, and neutrinos can induce air showers but they are much rarer.
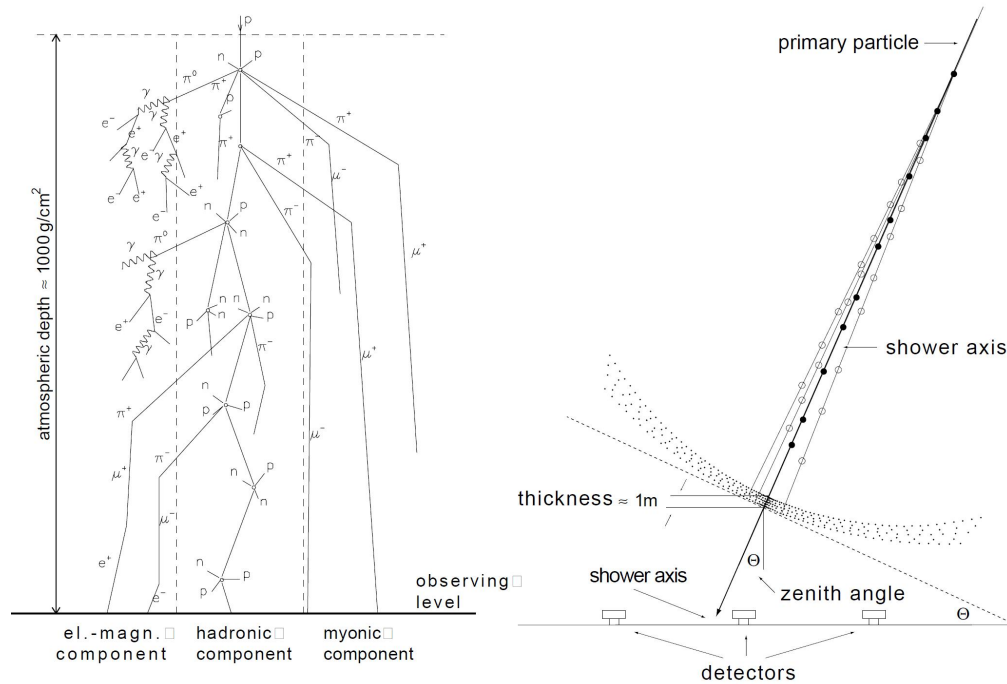
Figure 2.6: Schematic view of an hadron induced extensive air shower [68].

2.3.1   Components of extensive air showers

The three components of an EAS can be distinguished by means of particle physics detection. The hadronic component adds particles to the muonic and electromagnetic-component. Regardless, all three components have typical evolution processes.

Hadronic component

The pions or other mesons, and baryons represent the hadronic component of the EAS comprising about 1% of all particles detected at ground level. The first collision of a primary hadronic nucleus typically produces more than fifty secondaries and they carry most of the energy in the early shower stage. Due to their high longitudinal momentum they are emitted close to the original particle direction and the lateral spread is only a few tens of meters if one stretches the path length to the observation level. Fluctuations in the hadronic component can significantly influence the development of the other two components as they evolve from it. For electrons or gammas as air shower primary the hadronic component is of course much smaller, as the first interaction only leads to electromagnetic cascades.

Muonic component

The hadronic component leads to large numbers of different mesons, with extremely short lifetimes (e.g. 10^{-17} s for the π^0). If they do not interact during their propagation through the atmosphere, they will decay into lighter mesons or directly into leptons. Though it is only a small fraction of the possible reactions, the most frequent ones are given here with their branching ratio (BR) and mean lifetime τ:

$$
\begin{aligned}
\pi^{\pm} &\rightarrow \mu^{\pm} + \nu_{\mu}(\overline{\nu}_{\mu}) & (BR\,99.99\%) & \quad \left(\tau\,2.6 \cdot 10^{-8}\,\mathbf{s}\right) \\
K^{\pm} &\rightarrow \mu^{\pm} + \nu_{\mu}(\overline{\nu}_{\mu}) & (BR\,64\%) & \quad \left(\tau\,1.2 \cdot 10^{-8}\,\mathbf{s}\right) \\
&\rightarrow \pi^0 + \pi^{\pm} & (BR\,21\%) & \\
&\rightarrow 3\pi^{\pm} & (BR\,5\%) & \\
&\rightarrow \pi^0 + \mu^{\pm} + \nu_{\mu}(\overline{\nu}_{\mu}) & (BR\,3\%) & \\
\mu^{\pm} &\rightarrow e^{\pm} + \overline{\nu}_e(\nu_e) + \nu_{\mu}(\overline{\nu}_{\mu}) & (BR\,21\%) & \quad \left(\tau\,2.2 \cdot 10^{-6}\,\mathbf{s}\right).
\end{aligned}
$$

As the lifetime of muons is much longer than those of most hadrons, and due to time dilatation, they can reach ground level if they have relativistic speed. Muons can lose their energy by ionization and by radiative processes such as, bremsstrahlung, and photo nuclear interactions. The mean free path length of muons in matter is much larger than the path length of electrons caused by its higher mass. This leads to the idea to measure the muonic component of air showers using material shielding (e.g. iron or earth) to filter out the electron component. This is applied in lots of experiments.

Electromagnetic component

About 90% of the total number of charged particles are electrons and positrons. Together with the photons, they are the so called "electromagnetic component" of the air shower. Most of the particles of the electromagnetic component are produced in electromagnetic cascades, an interplay of electrons/positrons and photons:

$$
\gamma \rightarrow e^+e^- \tag{2.15}
$$

$$
e^{\pm} \rightarrow e^{\pm} + \gamma. \tag{2.16}
$$

A typical starting point of electromagnetic cascades in an air shower is a photon (e.g. from π^0 decay reaction 2.13). From there the cascade develops through repeated cycles of pair production (Eq. 2.15) and bremsstrahlung: The γ decays into e^+e^- pairs via Eq. 2.15 and they build a new photon (Eq. 2.16). The cascade continues until the energy has fallen below a critical energy E_C (for air $E_C \approx 80$ `MeV`). Then the energy loss via ionization becomes dominant and no new particles are produced in the cascade. At this stage, the cascade will start to die out and an exponential decrease for the number of particles takes effect, with $N \propto$ `exp` $\frac{X_{max}-X}{\lambda}$, where x is the atmospheric depth.

The total number of particles in a shower relates logarithmically to the primary energy, until a certain particle specific threshold energy is reached and beyond which no new particles will be created anymore. At a certain height of the EAS development a maximum N_{max} for the number of particles in the shower disc is reached, and afterwords the number decreases exponentially. In terms of atmospheric depth X (in g `cm`$^{-2}$) the EAS at the shower maximum has a depth X_{max}. The longitudinal shower development can be described with the Gaisser-Hillas function [19]:

$$N\left(X\right) = N_{max} \cdot \left(\frac{X - X_0}{X_{max} - X_0}\right)^{\frac{X_{max}-X_0}{\lambda}} \text{exp} \frac{X_{max} - X}{\lambda}. \qquad (2.17)$$

The number of charged particles N at a given atmospheric depth X in this relation also depends on the parameters X_0 (radiation length) and λ that determine the shape of the shower. The number of particles increases with atmospheric depth up to the value X_{max} and decreases exponentially afterwords.

Besides the creation and loss of particles in the longitudinal direction, the electromagnetic component is gradually spread in the lateral direction by means of Coulomb scattering. This spread is described by Moliere theory [52] and has a characteristic quantity, the Moliere radius R_m:

$$R_m = X_0 E_s / E_c, \qquad (2.18)$$

where X_0 is the radiation length of the atmosphere, E_s the scale energy (21 `MeV`), and E_c, the critical energy ($\propto a/(Z+b)$), with some scale parameters a,b. Nishimura, Kamata, and Greisen found the lateral distribution of electrons at observation level were described by the so called "NKG" [36] function:

$$\rho\left(d_{axis}\right) = \frac{N_e}{2\pi R_m^2} \cdot \left(\frac{d_{axis}}{R_m}\right)^{s-\alpha} \cdot \left(1 + \frac{d_{axis}}{R_m}\right)^{s-\beta} \cdot \frac{\Gamma\left(\beta - s\right)}{\Gamma\left(s\right)\Gamma\left(\beta - \alpha \cdot s\right)}, \qquad (2.19)$$

where the electron density $\rho(d_{axis})$ is calculated from the measured number of electrons N_e at the observation level and d_{axis} is the distance to the shower axis. The shower age s is fitted to the lateral particle distribution on sea level and describes the lateral shape, whereas the parameters α and β are used as normalization factors.

2.4 Radio Emission of Extensive Air Showers

As a large fraction of the extended air shower (EAS) particles are charged, not only energy loss through secondary particles in matter is expected, but also other effects like fluorescence, ionization, Cherenkov, and synchrotron radiation. In the following the synchrotron mechanism will be described as it is the basis for the detection technique discussed in this thesis.

2.4.1 Geo-synchrotron emission

The geomagnetic field of our Earth influences the trajectories of the charged particles of extensive air showers. The large electromagnetic component of the air shower that moves through the Earths' magnetic field, is subjected to the Lorentz force. The Lorentz force is given by:

$$\mathbf{F} = q(\mathbf{v} \times \mathbf{B}), \tag{2.20}$$

where q is the charge, $\mathbf{v}$ the velocity, and $\mathbf{B}$ the magnetic field vector. Positive and negative charges are deflected in opposite directions as illustrated in Fig. 2.7. The acceleration of the charges leads to emission of radiation in the direction of motion. For highly relativistic particles with a high Lorentz factor γ the original dipole emission is focused into a narrow emission cone with an opening angle of order of $2\gamma^{-1}$. This causes short pluses with frequency components significantly higher than the gyration frequency of the particle. As this synchrotron radiation is produced in the Earths' magnetic field, it is called "geo-synchrotron radiation".

2.4.2 Analytical description of the emission process

The analytical calculations from Huege and Falcke [27] take as starting point the radiation of a single particle in the frequency domain. The electrical field of a particle moving through the magnetic field can be expressed via the vector potential $\mathbf{A}(\mathbf{R}, \omega)$
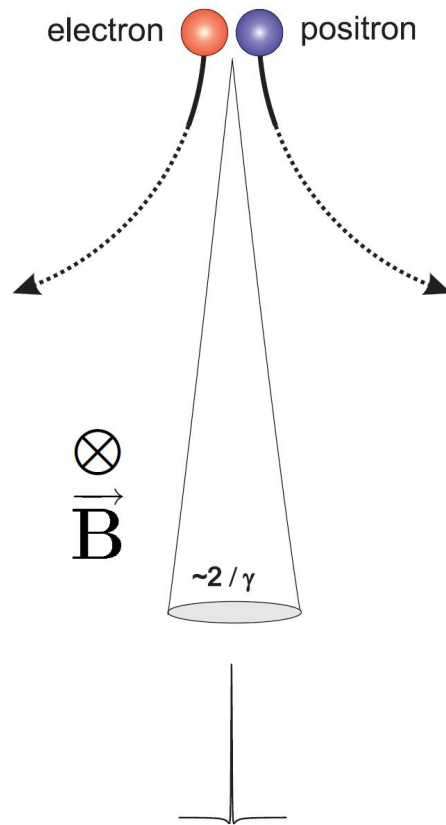
Figure 2.7: Electrons and positrons (or $\mu^{\pm}$) propagate through the magnetic field **B** of the Earth and are deflected due to Lorentz force. Thus the accelerated relativistic moving charge emits electromagnetic radiation in the direction of motion. The emission is coherent in frequencies of 1 `MHz` to 150 `MHz` and leads to strong radio pulses of some 10 `ns` length.
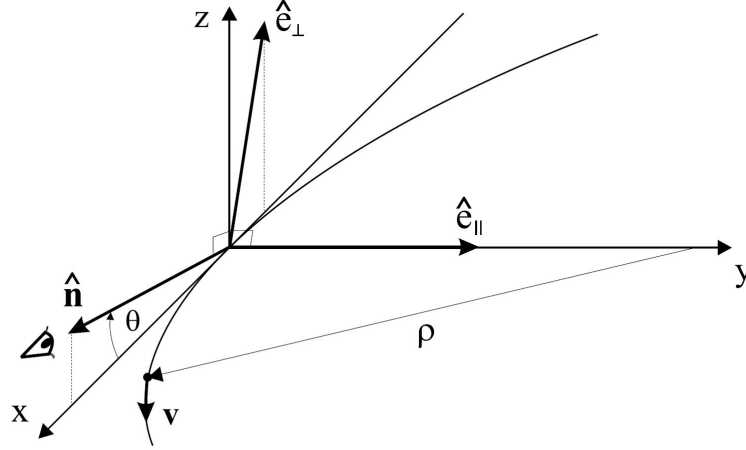
Figure 2.8: Geometry of single particle synchrotron radiation for an observer with line-of-sight vector $\hat{\mathbf{n}}$ enclosing a minimum angle θ to the instantaneous particle velocity vector $\mathbf{v}$. The equivalent curvature radius is given by ρ, and the emission can be conveniently divided into the components $\hat{e}_\perp$ and $\hat{e}_\parallel$. The particle trajectory lies in the x-y plane [27].

(Jackson [33]), where $\mathbf{R}$ is the vector from the particle to the observer and ω is the frequency component of the electrical field normalized to unit solid angle Ω. For large distances to the observer, $\mathbf{A}(\mathbf{R}, \omega)$ can be separated into two perpendicular components $\hat{e}_\perp$ and $\hat{e}_\parallel$:

$$\mathbf{A}(\mathbf{R}, \omega) = \frac{\omega e}{\sqrt{8c\pi}} \exp\left(i\left(\omega\frac{R}{c} - \frac{\pi}{2}\right)\right)\left[-\hat{e}_\parallel(\omega) \pm \hat{e}_\perp\right], \qquad (2.21)$$

where e is the unit charge, while the $\pm$ sign distinguishes electrons $(+)$ and positrons $(-)$. The geometry of the problem corresponds to Fig. 2.8. The origin of the coordinate system is set to the point on the particle trajectory where the angle between instantaneous particle velocity $\mathbf{v}$ and line of sight vector $\hat{n}$ reaches its minimum θ. Together with far field approximations using modified Bessel-Functions K_a of the order a and the assumption that the observing frequency ω is high compared to the gyrating frequency ($\mathtt{kHz} < \mathtt{MHz}$) of the particle, Jackson [33] calculates the energy spectrum per unit solid angle of a single particle retaining phase information as:

$$\begin{aligned}
\frac{d^2I}{d\omega d\Omega} = 2\left|\mathbf{A}(\mathbf{R}, \omega)\right|^2 &= \frac{e^2}{3\pi^2 c}\left(\frac{\omega\rho}{c}\right)^2\left(\frac{1}{\gamma^2} + \theta^2\right)^2 \\
&\times \left[K_{2/3}^2(\xi) + \frac{\theta^2}{\gamma^{-2} + \theta^2}K_{1/3}^2(\xi)\right],
\end{aligned} \qquad (2.22)$$

where the curvature radius ρ is:

$$\rho = \frac{\nu \gamma m_e c}{e B sin(\alpha)}, \tag{2.23}$$

with the observing frequency $\omega = 2\pi \cdot \nu$. θ is the observing angle relative to the plane of the curvature radius ρ and ξ is:

$$\xi = \frac{\nu \omega \rho}{3c} \left(\gamma^{-2} + \theta^2\right)^{3/2}. \tag{2.24}$$

Given a specific distance to the observer R, the frequency component of the E-field can be calculated as

$$\mathbf{E}\left(\mathbf{R}, \omega\right) = \sqrt{\frac{4\pi}{c}} \frac{1}{R} \mathbf{A}\left(\mathbf{R}, \omega\right), \tag{2.25}$$

for a specific distance to the observer R. For a given distribution of gyrating particles during the evolution of a CR air shower, the corresponding $\mathbf{E}\left(\mathbf{R}, \omega\right)$ can then be superimposed to calculate the total emission.

In the case of fully coherent superimposition of the emitting particles the energy spectrum grows $\propto |\mathbf{A}\left(\mathbf{R}, \omega\right)|^2$ which itself grows as N^2 with the number of particles N. This gives us an upper limit for the growth of the energy spectrum.

The emission of the electric field scales linear with the primary particle energy of the air shower, in the case of full coherence. In the coherent regime, the field strength directly scales with the number of emitting particles. (The emitted power consequently scales as the squared number of particles.) Since the number of particles electrons and positrons grows approximately linearly with primary particle energy, the linear scaling directly translates to a linear scaling of the field strength with primary particle energy.

Another interesting correlation is the dependence of the emission on the track length. The more inclined the air shower the longer is the track length of the charged particles through the magnetic field. This leads to broadening of the emission to larger distances to the shower core. One effect occurring when the air shower is inclined is the projection on the detector plane. The other broadening effect is that the air shower maximum for inclined showers is much further away from the ground than for vertical showers. This leads to a lager footprint of the emission on the ground. This correlation with inclination angel makes inclined air showers an especially interesting target for observation with radio techniques.

2.4.3 Radio emission of CORSIKA simulated air showers

With the air shower particle simulation package CORSIKA [24], the evolution of the different shower stages can be described directly. It simulates the trajectories (especially electrons and positrons) of different, individual air showers.

Based on the CORSIKA simulated trajectories of the charged EAS particles the REAS2 code [29] calculates the geo-synchrotron emission of these particles with a specific magnetic field, observation height, and distribution of observers on the observation plane like motivated in Sec. 2.4.2. This Monte Carlo simulation enables us to investigate in detail the radio emission from EAS for single air showers responding environmental conditions such as the atmospheric properties at the South Pole. Figure 2.10 shows the discrete Fourier transformation of a REAS2 Monte Carlo simulation of a proton induced air shower with 10^{17} eV primary energy with South Pole conditions. The spectrum was calculated for different distances of the observer to the shower center (from $25\,\mathrm{m}$ up to $325\,\mathrm{m}$ north)[1] and exhibits a drop down of the spectra toward higher frequencies. More simulation results will be discussed together with experimental results and assumptions in Section 5.

The Monte Carlo simulations calculate the radio pulse in the time domain. An example of these simulations is shown in Fig. 2.9, where the development of the pulse height for different distances to the shower core is shown. The pulse height has been calculated for a vertical shower with a primary energy of 10^{17} eV. The E-field strength at different distances to the center of the shower exhibits a decreasing of the amplitude combined with a broadening. Note that the field strength of the pulses in Fig. 2.9 have been scaled with different factors for a better visibility. One has to combine these pulses with the properties of the instrumental response of the experimental devices to make a prediction of a realistic pulse shape in experimental measurements. This will be shown in Section 5.

Comparisons of REAS2 simulations with experimental results of the LOPES experiments have shown that the simulation is able to describe the radio emission from air showers only qualitatively (Fig. 2.11). However this simulation offers currently the most realistic description of the radio emission of EAS [50] and will be used for further simulations of EAS radio emission measurements at the South Pole (Chapter 6).

---

[1]The direction "north" at the geografic South Pole is in this case relative to the geomagnetic South Pole, currently $78°$ South, $110°$ East.
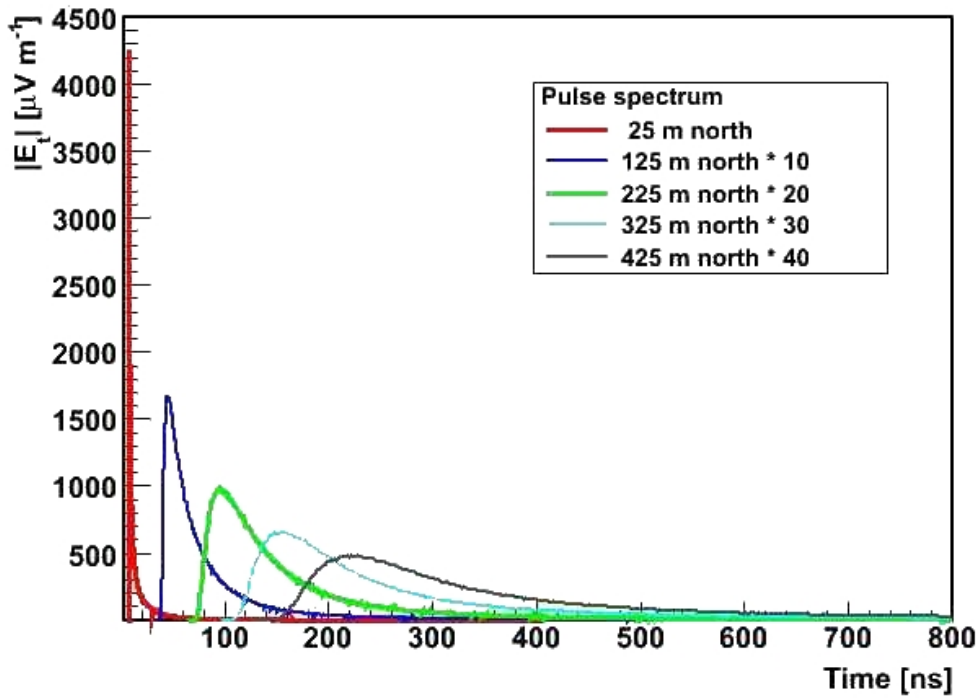
Figure 2.9: The electric field strength and time profile of REAS2 simulated pulses for different distances from the shower center with South Pole conditions. The observer is north of the center and the Monte Carlo simulation was performed for a vertical 10^{17} eV shower. The pulses are scaled for better presentation.
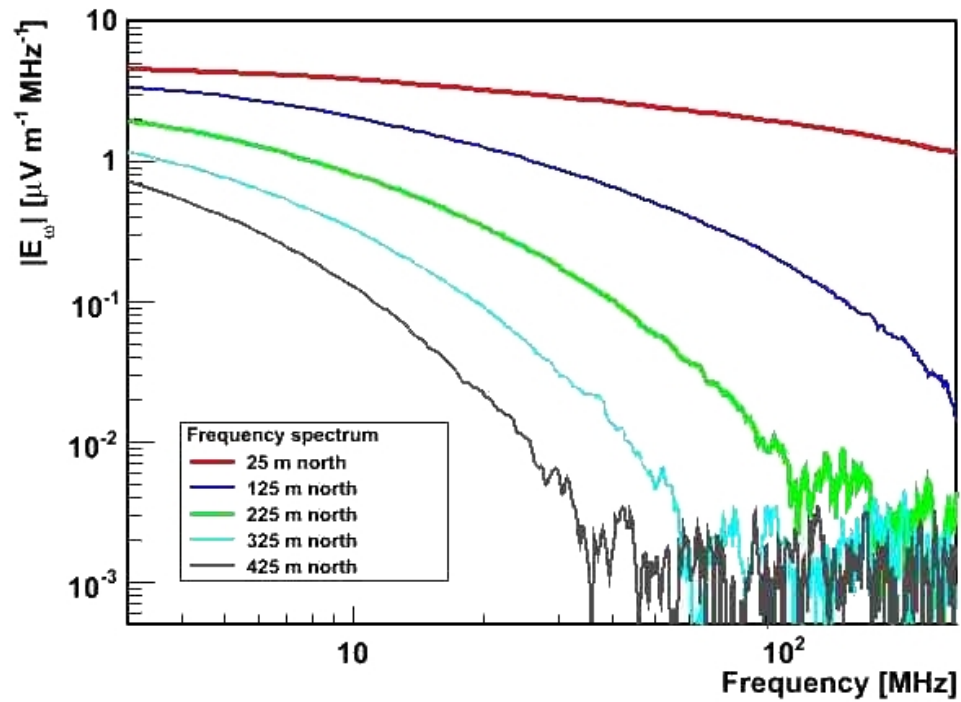
Figure 2.10: REAS2 spectrum of the electric field $|E_\omega|$ with South Pole conditions. A vertical 10^{17} eV proton induced air shower observed at different distances to the shower core was simulated. The spectrum decreases very fast (note the log-log scale) until numeric noise at larger frequencies becomes dominant (right bottom).
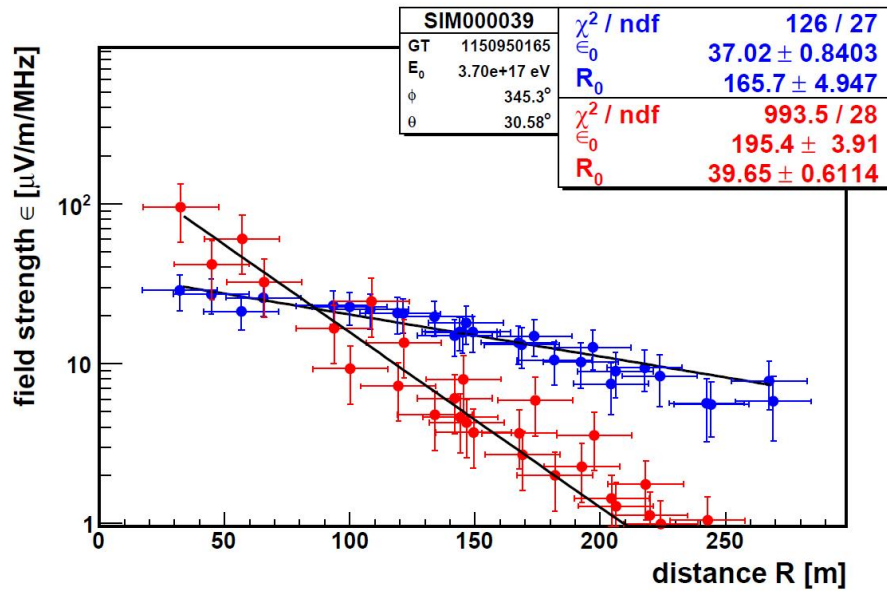
Figure 2.11: Calibrated measurements of the lateral distribution of air showers by the LOPES experiment (blue) together with REAS2 simulations of geo-synchrotron emission of a CORSIKA simulated air shower with the same inclination θ, declination ϕ, and energy E_0. The picture was taken from [50].

Chapter 3

ASTROPARTICLE DETECTORS

Most of the techniques used to detect cosmic ray induced air showers and also neutrinos are based on photo multipliers. They detect light emission of electromagnetic charged particles reacting in dense media. To find complementary signatures of air showers one has to look for different physical mechanisms or detection techniques. With regards to the very different properties of the different types of cosmic rays one wants to detect, the astroparticle detectors vary in size and detection strategy. Notwithstanding, some various techniques and several experiments to detect cosmic rays or neutrinos are discussed in this chapter. Some experiments designed to measure radio emissions of air showers and other cosmic radiation will be discussed in more detail.

3.1 LOPES

The LOPES experiment is mentioned as an example for a radio air shower detector [17] (Fig. 3.1). The LOPES (LOfar PrototypE Station) experiment consists of 41 antennas of different types distributed over the area of the KASCADE-Grande experiment in the Forschungszentrum Karlsruhe, Germany (Fig. 3.1). KASCADE-Grande is the extension of the smaller KASCADE-array. Both will be described in the following. The first installed antennas were designed as prototypes for the LOFAR experiment [58], a large antenna array for astronomical purposes. LOFAR is presently being built in the Netherlands. The initial idea for LOPES was to test the potential of the LOFAR setup for the measurement of cosmic rays and to investigate the properties of the radio component of an extensive air shower. The applicability of the detection method to large scales is being tested especially with self-triggered antennas, $LOPES^{STAR}$. Another experiment, CODALEMA [4], at the Nancay radio
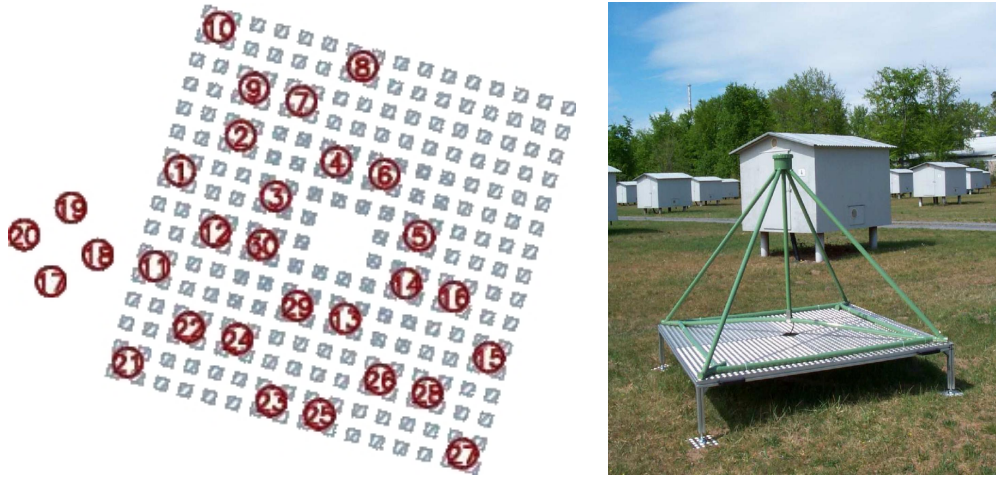
(a) Layout of LOPES on the KASCADE array. The red dots indicate 30 different antenna positions.

(b) Example of a LOPES inverted-V dipole antenna.

Figure 3.1: LOPES is installed on the field of the KASCADE-array. KASCADE consists mainly of 252 stations (white huts) with scintillation detectors.

observatory is also investigating the radio component.

3.1.1 LOPES hardware system

LOPES consists at present of 30 LOFAR-type low band antennas as well as newly designed antennas forming the $LOPES^{STAR}$ array [21]. All antennas and the electronics are optimized to measure in the relatively noise-free frequency range from 40 MHz to 80 MHz in Karlsruhe.

The initial LOPES antennas are inverted-V dipoles and are installed inside the KASCADE-experiment [3]. In Figure 3.1b one of the LOPES antennas at the KASCADE-array is shown. The geometry of the frame keeping the inverted-V dipole antenna is a four-sided pyramid made out of PVC tubes. The height of the pyramid is 1.4 m and the base length is 2.0 m. An active balun on top of the antenna performs the unbalanced to balanced conversion, what is the transformation of the antenna impedance to the 50 Ω impedance of the transmitting cable. Also, the balun amplifies the received signal.

The antennas are connected to low noise amplifiers (LNA). The signal is then transmitted via a coaxial cable to one of three stations where it is again amplified, filtered and digitized. Figure 3.2 shows a scheme of the LOPES electronics.
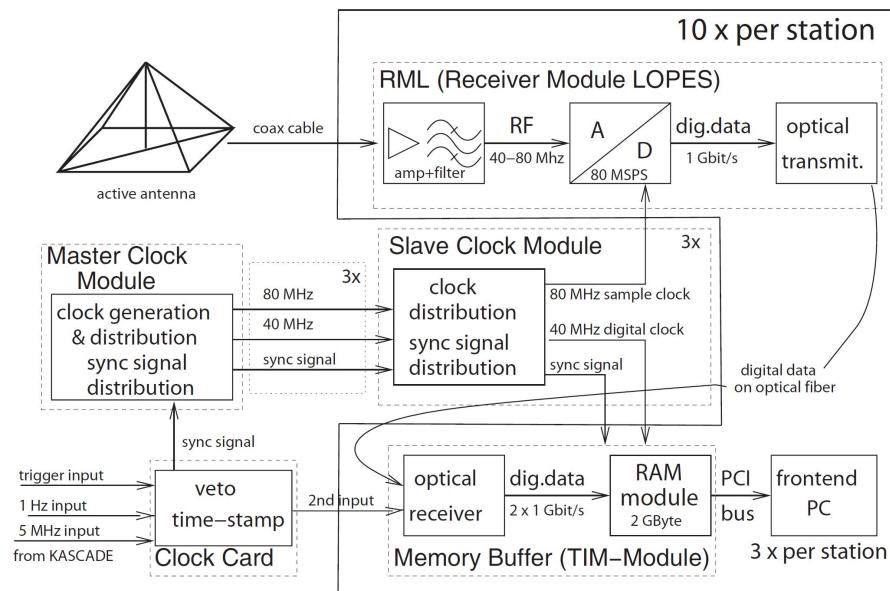
Figure 3.2: Incoming signals are received with the active inverted-V dipole antenna and transmitted via a long coaxial cable (RG-213) to the receiver module. The amplified and bandpass filtered analog signals are digitized with a 12-bit analog to digital (A/D) converter. After the optical fiber transmission to the A/D converter, the signals are stored in a memory buffer. Trigger from KASCADE-Grande are distributed by a master clock module to each station and finally transmitted to the front-end PC for data read-out [3].

3.1.2   Trigger strategy

The aim of the LOPES experiment is to correlate the observables of the radio measurements with the shower properties provided by the particle air shower experiment KASCADE-Grande. For this reason LOPES is triggered by KASCADE-Grande and uses the reconstructed shower data as input for the pulse analysis. KASCADE-Grande consists mainly of stations equipped with scintillation detectors, where 256 stations compose the KASCADE-array, and further 37 large stations the Grande array see Figure 3.3. The KASCADE-array is a regular grid of detector stations with a spacing of 13 m.

The LOPES experiment is triggered via a KASCADE trigger or a KASCADE-Grande trigger:

- The KASCADE array consists of 16 clusters, 4×4 detector "huts" in a square each. If 8 of the 16 detector huts achieve the trigger condition, the cluster has a trigger. The KASCADE trigger for LOPES is given if 10 of the 16 KASCADE clusters have a trigger.

- The KASCADE-Grande array has another cluster strategy. A cluster trigger is given if 7 detector stations have a trigger, one station surrounded by the six direct neighbors. The trigger condition for LOPES is that all detector stations of the 3 hexagons near the KASCADE array have a trigger.

3.1.3   LOPES STAR

In addtion to the array of 30 inverted-V dipole antennas, there are 10 LPDAs (Logarithmic Periodic Dipole Antennas) installed in the south-east part of the KASCADE-Grande array. The aim is to investigate self-trigger strategies for radio air shower detectors [7]. The suppression of radio background events at places with a lot of anthropogenic background sources is of great importance for self-trigger strategies. The strategy of the $LOPES^{STAR}$ array is to cut away pulses which have a long signature in the time domain. Where signals are recorded in the frequency range from 40 MHz to 80 MHz, the envelope of the recorded signal has to be shorter than 300 ns above the threshold. This can be the basis for a surface radio air shower detector as part of the Pierre Auger Observatory.
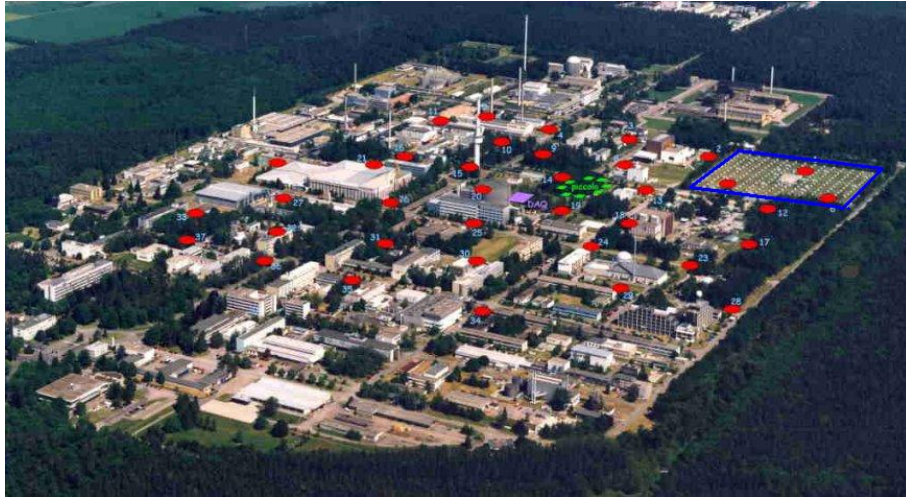
Figure 3.3: Aerial view of the KASCADE-Grande array on the area of the Forschungszentrum Karlsruhe. The red dots indicate KASCADE-Grande stations. The smaller KASCADE array, where the LOPES antennas are, is marked with a blue rectangle.

3.2 IceCube

One of the main scientific goals of IceCube is the detection of neutrinos at energies above 100 `GeV`. Charged massive particles undergo absorption and deviation effects in interstellar matter and magnetic fields when propagating through the interstellar space and photons are absorbed by intergalactic matter. In contrast, cosmic neutrinos can directly reach the Earth without being strongly affected in their propagation between the source and the detector. This is a seductive argument for neutrino astronomy and led to approaches like AMANDA, ANTARES or IceCube. The general detection strategy is to use a large, dense, light transparent media and to detect the Cherenkov light of leptons produced by the interaction of neutrinos with matter.

In the final state, IceCube will consist of about 5160 photo multipliers (PMTs) distributed in $\approx 1\,\text{km}^3$ antarctic ice. The photo multipliers are deployed on up to 86 strings with 60 PMTs each in a depth between $1450\,\text{m}$ and $2450\,\text{m}$ in the antarctic ice at the geographic South Pole (Fig. 3.4). The distance between the digital optical module (DOM) of the standard IceCube strings, which are housing the PMTs, is $17\,\text{m}$ vertical. Each of theses strings is the corner of an equilateral triangle with $125\,\text{m}$ side length. In addition, IceCube has so called "DeepCore" strings. These strings are deployed in the middle of the IceCube detector between the standard strings. There, the DOMs are located at a depth from $2107\,\text{m}$ to $2450\,\text{m}$ and have a $7\,\text{m}$ vertical spacing. The air shower array IceTop covers a surface area of $1\,\text{km}^2$ above the in-

ice detector. IceTop will measure cosmic ray air showers in the energy range from 300 TeV to above 1 EeV. It consists of 160 ice tanks detecting Cherenkov radiation of the charged air shower particles. The in-ice detector is designed to detect neutrinos of all flavors (ν_e, ν_μ, and ν_τ) in the energy range from 10^{11} eV with DeepCore to beyond 10^{18} eV. The PMTs measure the Cherenkov radiation of leptons that are produced as a result of neutrino-nucleon interaction in the ice. The Cherenkov cone is detected by several PMTs. This is the basis to reconstruct the energy, flight direction and type of the primary particle. One of IceCubes main goals is the search for sources of high energy astrophysical neutrinos which provide important clues for understanding the origin of high energy cosmic rays (cf. Section 2.2.5).

At primary neutrino energies $< 10^{12}$ eV, the DeepCore strategy is to use IceCube as a veto detector. Leptonic tracks starting in the IceCube or DeepCore volume are a clear signature for a neutrino induced cascade. These signatures can be distinguished from air shower induced background, as the tracks from air showers are starting outside the IceCube detector. At low neutrino energies $> 10^{12}$ eV the effective total flux of neutrinos interacting direct in IceCube gets low. At these energies the strategy is to measure up-going events. The primary particles of these events have to traverse the Earth, which is only possible for particles with large free path length. But the cross section of neutrinos increases with increasing energy, thus, for EHE neutrinos (Extremly High Energy) with energies > 300 TeV using the nucleon total cross section Eq. 3.1 from [56],

$$\sigma_{tot} = 1.2 \cdot 10^{-32}~\text{cm}^2 \left(\frac{E_\nu}{10^9 \text{GeV}} \right)^{0.4}, \tag{3.1}$$

the Earth becomes opaque and IceCube has to use down-going or inclined events from the southern hemisphere. The signal of down-going neutrinos from the southern hemisphere is unterminated by the muonic background from cosmic ray air showers. This is interesting for composition studies of air showers, where IceTop detects the signal of electrons and muons both together and IceCube only the muonic component of the air shower. In contrast, it is a huge problem for UHE neutrino detection to get a huge amount of background from CR induced muons. A possible strategy to veto the muonic background with a large surface geo-synchrotron radio air shower detector around IceCube is discussed in Section 6.2.1.

In addition, the IceCube infrastructure hosts several other R&D projects and smaller experiments to investigate new detection techniques for air showers and EHE neutrinos, for example cosmogenic neutrinos as discussed in Section 2.2.4. New detection strategies are the detection of electromagnetic signatures in the radio frequency regime from 200 MHz to 1.3 GHz. Also acoustic pulses of the thermonuclear interaction of a neutrino induced hadronic cascade in ice are a promising UHE neutrino

IceCube Lab

50 m

IceCube

IceTop
80 Strings each with
2 IceTop Cherenkov Detector Tanks
2 Optical Sensors per tank
320 Optical Sensors

2004	Project Start	1 Hole
2009	Current Status	59 Holes
2011	Projected Completion	86 Holes

IceCube In-Ice Array
86 Strings, 60 Sensors
5160 Optical Sensors

1450 m

Deep Core
6 Strings - Optimized for low energies
360 Optical Sensors

324 m

2450 m
2820 m

Bedrock

Figure 3.4: Schematic of the IceCube detector in its final configuration. The low energy array DeepCore will be placed in the bottom middle of the fully deployed IceCube detector. IceTops position is on top of each IceCube string without the DeepCore strings. The 59 colored strings are in operation since 2009 [75].

(a) Every IceTop station consists of two Ice-Top tanks. The picture shows the two tanks of station 21 before refilling.
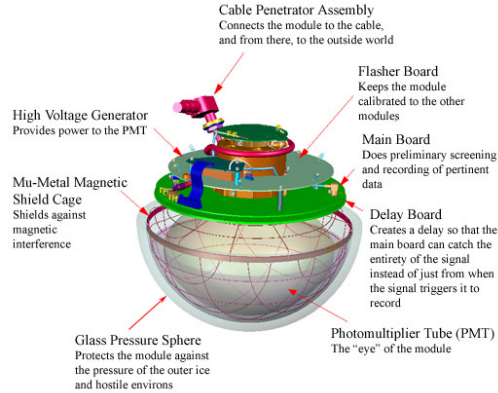
(b) Schematic view of a Digital Optical Module (DOM) used for IceCube and IceTop. The photomuliplier signals measured in-ice are already digitized in the DOMs. The digital signal is than send to the IceCube Counting Laboratory (ICL).

Figure 3.5: While the DOMs of IceCube are directly deployed into the antarctic ice, the IceTop modules are held in-ice tanks on the surface. An IceTop detector station is situated on top of every IceCube String. [75]

signature [15]. Acoustic properties of the antarctic ice and the acoustic noise environment at the South Pole are currently under investigation with SPATS (South Pole Acoustic Test Setup) [65]. Some possible new radio frequency based detection techniques will be discussed in Section 3.3 (RICE, NARC and ARA).

3.3   RICE and NARC

Every large radio detector system needs suitable environmental conditions. The most important conditions for radio detectors are quietness in the frequency range of interest and large homogeneous radio transparent media as target volumes. As Antarctica is mostly uninhabited, it is probably one of the most radio quiet areas in the world. In addition, the huge ice cap of Antarctica is a large radio transparent medium promising for radio detection techniques. Due to this unique conditions there are several approaches to measure radio signals of cosmic rays.

One of the first approaches to use Antarctica for radio detection techniques in the frequency range from `MHz` to `GHz` is RICE, the Radio Ice Cherenkov Experiment. It consists of 18 radio antennas deployed at the IceCube site at the South Pole. The antennas are spread over a $200 \times 200 \times 200\,\mathrm{m}^3$ cube in a depth of $100\,\mathrm{m}$ to $300\,\mathrm{m}$. The

effective frequency range of RICE in-ice is 200 `MHz` to 500 `MHz`. Figure 3.6 gives an overview of the Rice antenna positions in ice.

The idea of RICE is to detect radio pulses of neutrinos induced in ice due to the so called "Askaryan effect". It is named after Gurgen Askaryan and it stands for coherent Cherenkov radiation of electromagnetic cascades in a dielectric medium [9]. High energy processes such as Compton, Bhabba, and Moller scattering, along with positron annihilation rapidly lead to a $\approx 20\%$ negative charge excess in the electromagnetic part of the cascade. In a dense medium like ice the shower charge bunch is largely contained within a several `cm` core. At wavelength of 10 `cm` and more, much larger than the characteristic shower bunch size, the relativistic shower bunch appears as a single charge moving through the dielectric medium over a distance of several meters. Since the power of Cherencov emission grows quadraticaly with the charge of the emitter, the coherent power in the `cm` to `m` wavelength regime is orders of magnitudes larger than that emitted incoherently. This Asakaryan effected emission in ice has been measured by the ANITA collaboration at the SLAC accelerator [22].

As the RICE DAQ is also used for surface measurements at the South Pole (this thesis), we will describe the system in more detail in the following section.

3.3.1   RICE DAQ

The aim of the RICE DAQ is to self trigger radio signals of Askaryan pulses induced in ice.

DAQ analog part

Every in-ice antenna has a 36 `dB` low noise amplifier (LNA) directly attached to the antenna in the ice. The signal comes to the surface via coaxial cable. Then it is high pass filtered at 200 `MHz` and additionally amplified by 62 `dB`. The power supply of the LNAs is sent via bias-tees trough the signal cable. This signal is read out via digital oscilloscopes.

Digital part

In 2010, RICE consists of 7 oscilloscopes with 4 channels each. The oscilloscopes have a sampling rate of 1 `GHz` with 12 `bit` digitization and 8192 samples per channel. The signal input to these oscilloscopes are via BNC connection at the front. They are externally triggered by the RICE trigger logic. At the base of
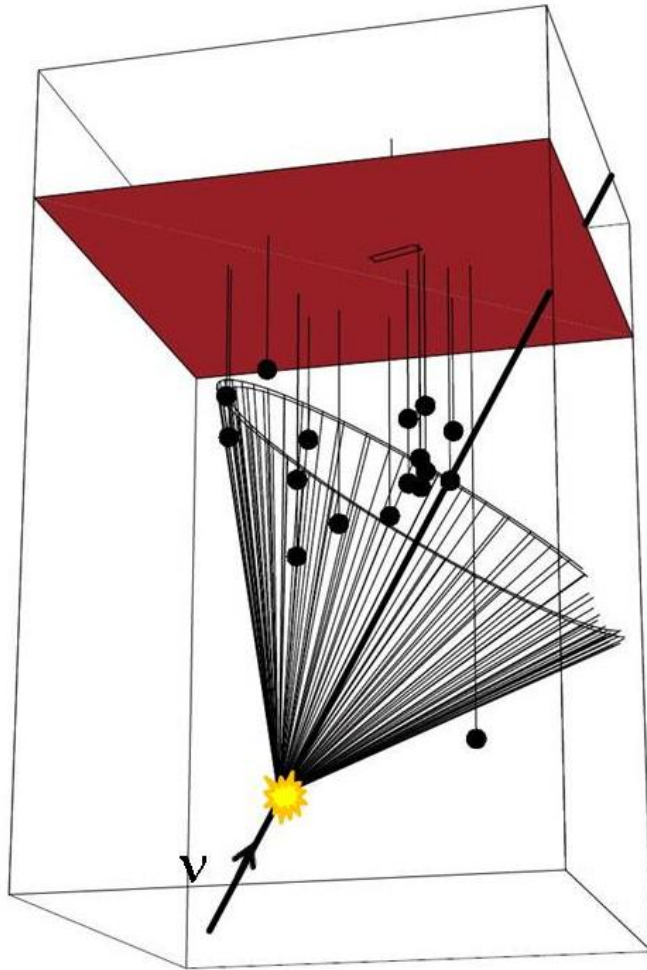
Figure 3.6: RICE schematic. The black dots indicate antenna positions of RICE under the ice. The rectangle on the red plane indicates the position of the MAPO building which houses the DAQ. The front of the cone shows the wave front of a typical Askaryan pulse of a lepton shower induced by an up-going neutrino.
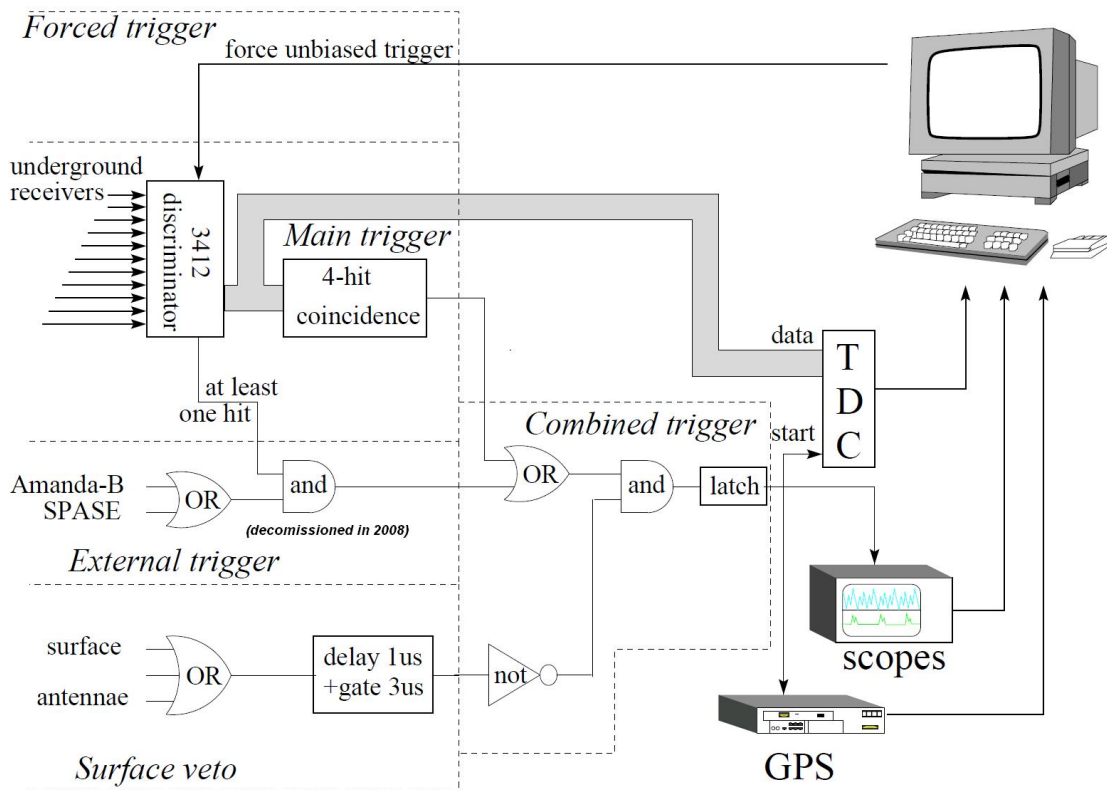
Figure 3.7: Schematic view of the RICE event trigger logic. The external trigger part was decommissioned in 2008. The main trigger system is a 4 coincidences logic [43].

the self trigger logic are LeCroy 3412E discriminators with a threshold range of $-15\,\mathrm{mV}$ to $-1.0\,\mathrm{V}$ in $5.5\,\mathrm{mV}$ steps. The LeCroy module MALU 4532 builds the trigger decision. A trigger is forced if $\geq N$ antennas have a signal over threshold within $1.25\,\mu\mathrm{s}$. The number of coincidences N is typically set to 4. It has to be set manually. A 16 channel digital delay unit provides a delay of up to $1.5\,\mu\mathrm{s}$ and allows to make in-ice trigger decisions. The TDC unit LeCroy 3377 combines the hit over threshold with the GPS times of a GPS CAMAC unit. The accuracy is $\approx 100\mathrm{ns}$. A schematic view of the RICE trigger electronics is given in Fig. 3.7.

Trigger strategy and event types

There are four different types of events recorded with the RICE DAQ:

- The RICE "self trigger", which is formed if ≥ 4 signal antennas receive a signal above threshold within a $1.25\,\mu\mathrm{s}$ time window. This event type is called

"General".

- A coincidence trigger with external experiments is possible. In the past this facility was used to trigger RICE together with SPASE and AMANDA. This event type is called "External".

- A random noise trigger which is read out every 10 minutes or after 100 triggers. It is a forced readout of all channels to set the dynamic threshold based on the RMS of the background level. This data will be used for background measurements of the surface antennas. This event type is called "Unbiased".

- There are two different possibilities to veto a RICE event. A "hardware surface trigger" (HST) is used to decide whether an event is background noise recorded from surface antennas or an in-ice event. The detector dead time caused by the surface trigger is 1.5 μs. More sophisticated veto logic is possible with a software veto. It is possible to program veto conditions due to timing or length of pulses over threshold. The detector dead time due to software veto events is about 8 ms per surface event. This event type is called "veto".

Data output stream

The RICE data is stored in an ASCII data format. It is send as a part of the IceCube data stream to the northern hemisphere and stored in the IceCube data storage system. The data is divided into "Event Loops" where every Event Loop is stored in a seperate file. Each Event Loop typically ends with a forced trigger event to calculate the threshold for the next Event Loop. One event loop is max 10 min or minimal 10 events long. A detailed description of an Event Loop file is given in Appendix B.
The RICE neutrino flux limit for all flavors is given in Fig. 2.4 together with measured atmospheric neutrino flux. It uses 854 days of RICE data and is currently the lowest flux limit at neutrino energies between $10^{17.5}$ eV and 10^{19} eV until ANITA sensitivity is getting strong. Nevertheless, the flux limit has to be 50 times lower to test cosmogenic neutrino predictions.

3.3.2   The NARC project AURA

AURA stand for "Askaryan Under-ice Radio Array" and is a radio frequency extension to IceCube [44]. It builds on the experience of the RICE experiment with its electronic design based on the radio frequency specific electronic applications developed by the ANITA collaboration [66]. It uses the communication and time calibration systems developed for IceCube and relies on the experience within

the IceCube collaboration to develop hardware and procedures for building and deploying highly sensitive electronic equipment in the extreme environment at the South Pole. Scheme 3.8b in Fig. 3.8 is a map of the existing AURA deployments on the IceCube footprint.

Each AURA unit, called a "cluster", consists of 4 receiver antennas, equally spaced over 40 m, a transmitting antenna for calibration and a sphere containing the electronics, called a Digital Radio Module (DRM), which is a modification of the IceCube DOMs. Six cables are connected to the DRM: One for power and communication going to the surface for data transmission; an additional cable that holds the Array Calibration Unit (ACU) and four cables connected to receiver antennas. A schematic of the AURA cluster is shown in Fig. 3.8a. A set of front-end electronics, including a chain of amplifiers and filters is mounted in front of each of the four receivers between the antennas and the DRM. The fast and broadband nature of the Askaryan radio signal is exploited for background reduction. Once the voltage measured on an antenna crosses an adjustable threshold, the digitization is triggered and the signal is split into four frequency bands $(200 - 400$ MHz, $400 - 650$ MHz, $650 - 880$ MHz, and $880 - 1200$ MHz) with the LABRADOR chip developed for the ANITA detector described in Section 3.4. If 3 of the 4 frequency bands are above threshold, the channel associated with this antenna will trigger.

The main tasks of AURA is to study the noise conditions at the South Pole and the attenuation of radio waves in ice. Due to the comparable size to RICE and AURA, neutrino analysis is not anticipated to significantly improve the RICE flux limits. As AURA uses IceCube timing, coincident studies between the two experiments are possible.
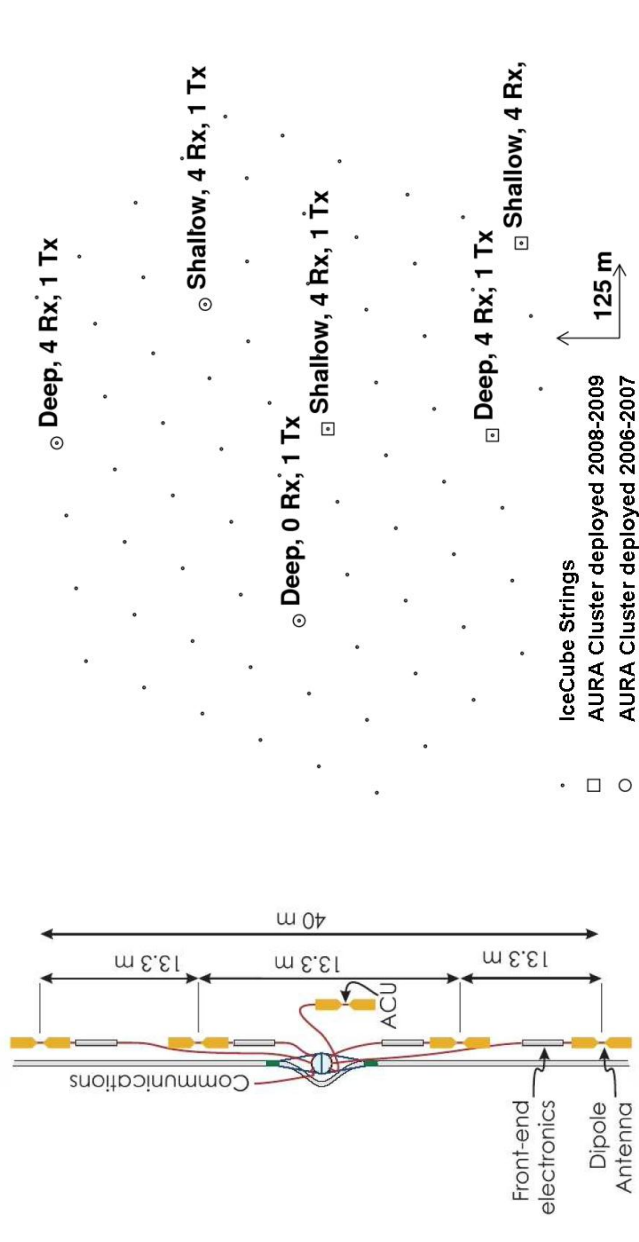
(a) The radio cluster, consists of a DRM (Digital Radio Module), and 5 antennas (4 receivers and a transmitter called ACU).

(b) Map of the existing AURA deployments, plotted on top of the full IceCube array. The distance between adjacent strings is 125 m. "Deep" corresponds to 1400 m depth, and "Shallow"' to 300 m depth. The number of receiving channels (Rx) and transmitting ACU channels (Tx) in each clusters are mentioned.

Figure 3.8: AURA deployments [44].
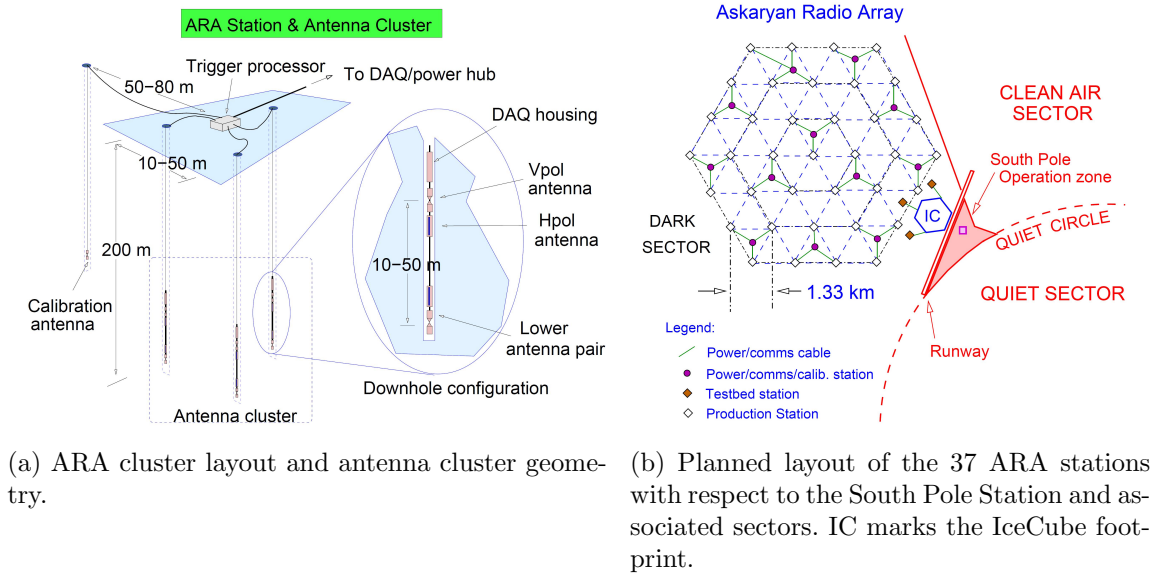
(a) ARA cluster layout and antenna cluster geometry.

(b) Planned layout of the 37 ARA stations with respect to the South Pole Station and associated sectors. IC marks the IceCube footprint.

Figure 3.9

3.3.3 Askaryan Radio Array

Due to the very low flux predictions on cosmogenic UHE neutrinos a detector has to have orders of magnitude higher effective volumes than RICE or AURA. An new approach on this at the South Pole is a large plane radio detector to detect UHE neutrinos. The Askaryan Radio Array (ARA) bases on experiences with RICE, ANITA, and AURA. ARA is aimed to detect Askaryan signals from high energy neutrinos. The frequency range of the array is proposed to be $200 - 650\,\mathtt{MHz}$. With 37 clusters and 4 antennas on each of the three strings per cluster, this leads to 444 antennas for detection plus 37 antennas for calibration. It is planed to deploy a large in-ice array up to $200\,\mathrm{m}$ below the surface. This relatively low depth will make cheap drilling methods with high air pressure possible and thus will lead to a good cost per effective area efficiency. Compared to existing instruments like RICE, it will increase the sensitivity by a factor of 100 in the energy range from $10^{17}\,\mathtt{eV}$ to $10^{20}\,\mathtt{eV}$. While at higher energies ANITA is more efficient, IceCube is specialized on energies up to $10^{17}\,\mathtt{eV}$ neutrino energy. Thus ARA covers the intermediate range. Figure 3.9 shows one cluster and the full array near IceCube as proposed. Construction shall commence in the end of the year 2010. One of the problems of neutrino detection with ARA could be to distinguish neutrino Askaryan signals from other possible sources with similar signature. Possible noise sources are Askaryan signals from air showers like detected with ANITA [23] or human made electromagnetic interferences.

(a) Drawing of the planned design of the ANITA detector. [51]

(b) The ANITA detector in 2008 configuration ready to fly.
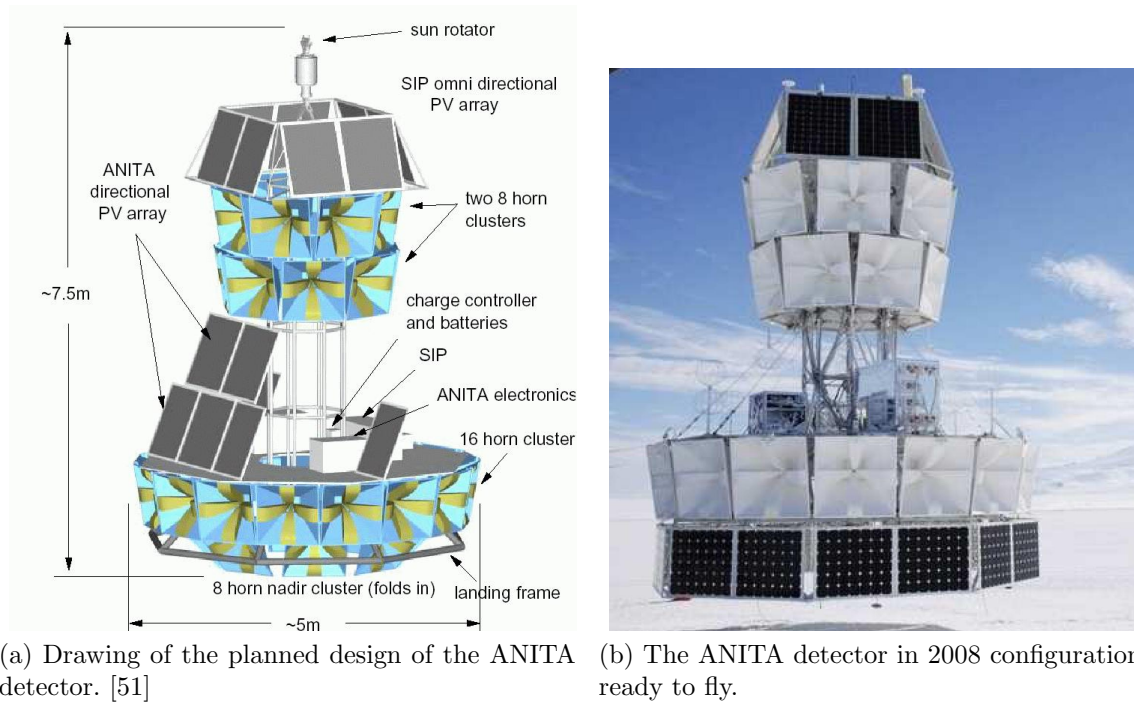
Figure 3.10: The balloon experiment consists of horn antennas specialized to frequencies from $200 - 1280$ MHz. At altitudes of $35 - 37$ km it observes the Antarctic ice sheet for broad band Askaryan pulses. The difference of the planned and final configurations are the positions of the lower solar panels. The final configuration makes it unnecessary to rotate ANITA toward the sun.

3.4   ANITA

The "Antarctic Impulsive Transient Antenna Ultra-high Energy Neutrino Detector" (ANITA) [23] instrument is a balloon experiment designed to fly over the continent of Antarctica. By using the circular winds of Antarctica ANITA is able to observe the ice sheet at an observation hight of ≈ 37 km for up to several weeks.

ANITA is, like AURA and RICE, specialized to measure the pulses of Askaryan pulses from high energy neutrinos in the Antarctic ice. ANITA searches for cascades initiated by a primary neutrino interacting in the Antarctic ice sheet within its field of view from the Long-Duration Balloon altitude of $35 - 37$ km. The observed area of ice from these altitudes is in the order of $15\,000\,000$ km^2. Combining this with the electromagnetic field attenuation length of ice which is of order of 1 km at ANITA's observation frequency range of $200 - 1280$ MHz, ANITA is sensitive to a target volume of order of $1\,000\,000$ km^3. A schematic view and a picture of the 2008 configuration are shown in Fig. 3.10. ANITA's trigger strategy is similar to AURA and bases on the same hardware, originally designed for ANITA. The
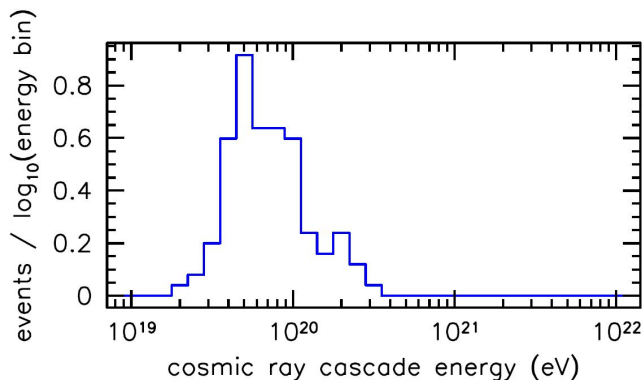
Figure 3.11: Differential energy distribution of simulated events. The simulation bases on pulses that are detected by ANITA-I. [23].

full bandwidth is divided in 4 frequency bands to trigger on broad band pulses and not narrow band radio frequency interferences. After two ANITA flights and 34 observation days in total, there is still no evidence for an UHE neutrino. The current flux limit extracted from ANITA measurements is shown in Fig. 2.4. It is currently the best limit for cosmic neutrinos above 10^{19} eV. Irrespective there is evidence for the detection of UHE cosmic rays with ANITA. During ANITA-I flight, 6 impulsive horizontally polarized radio signals where detected. Where neutrino induced impulsive radio signals are supposed to have a strong vertically polarized signal, air showers emit negligible synchrotron radio signals parallel polarized to the Earths' magnetic field. Thus radio signals from air shower should have strong signals in horizontal – but only weak signals vertical polarization. Detailed simulation studies show ANITA is adequate to detect these signals [23]. Where the energy threshold for EAS detection is estimated to be $\approx 4 \cdot 10^{19}$ eV the uncertainties in this prediction are dominated by the uncertainties in the magnitude of partially coherent emission from EAS radio processes in the frequency band of ANITA. Figure 3.11 shows the energy distribution of Monte Carlo events calculated from detected pulses with ANITA. The low energy turn-on is due to the energy threshold of the ANITA system, and the high energy edges are shaped by the GZK cutoff.

Chapter 4

RADIO MEASUREMENTS AT THE SOUTH POLE

This chapter will describe the strategies of surface radio measurement and their results from 2007-2009 at the South Pole.

- In 2007, first background measurements were made in Argentina (Auger site) and at the South Pole with a simple configuration.

- In 2008, available long cables were tested to provide long term measurements at a quiet facility (SPASE building).

- In 2009, a long term setup was deployed with four antennas to investigate the long term behavior of the radio background at the South Pole. Tests of Fat Wire-Dipole antennas where done, to find an adequate antenna to detect air showers under Antarctic conditions.

4.1   Radio Background

One of the most important obstacle of low signal detection of electromagnetic pulses is any kind of background.
Radio background can be divided by its properties into two general groups: continuous background and transients.

4.1.1   Continuous background

The major component of Earths' continuous electromagnetic background is the 2.7 K cosmic microwave background (CMB) radiation in the GHz regime. Together

with the cosmic background from our sun and our galaxy, this is unavoidable noise. The galactic background has a non thermal distribution in our frequency band [45]. A comparable noise source is the thermal background of the electrical conductors of the antenna and read out system itself. The electrons in the conductors follow thermal motion at the surrounding temperature. Even at the South Pole this leads to a 250 K Gaussian background.

Other continuous background sources are anthropogenic. Intentional radio frequency emission is usually mono frequent, such as radar, commercial radio, and communication. Inadvertent anthropogenic electromagnetic noise can be continuous, too. Electrical motors or dynamos as well as simple light bulbs can be a source of broad band electromagnetic emissions.

4.1.2   Transient electromagnetic interferences

Another group of electromagnetic noise is transient electromagnetic interference (EMI). EMI is mostly anthropogenic. Typical sources are again communication systems, but also inadvertent emission of nearly every electrical powered device or even combustion engines. Sometimes it has a well known signature in the frequency domain, but can be very broad band. As one of the main properties of air shower radio emissions is its pulsed structure, short pulsed EMI is an important source of background.

4.2   Measurements in Argentina and at the South Pole in 2007

The concept of the measurements in 2007 was to find a simple and portable design of antenna and setup, to make comparable measurements of the continuous background at different places in the world like IceCube site at the South Pole and Pierre Auger site in Argentina. A 3 m long copper wire with 3.5 mm diameter was used as a half arm dipole antenna. The copper wire of the antenna was coated within a PVC pipe. It was connected with 30 cm RG58 cable to a Miteq AM-1464 low noise amplifier (LNA) with 38 dB amplification in the frequency range from 2 MHz to 400 MHz. The amplified signal is than submitted via 100 m RG58 cable. Then the signals were read out with an oscilloscope or a spectrum analyzer. Figure 4.1 shows the schematic design of the measuring apparatus in Argentina and at the South Pole. The main differences are the various read out systems. Figure 4.2 shows pictures of the antenna at the Pierre Auger site in Argentina and at the South

Antenna in Agentina	Antenna at South Pole	50 m RG58 Cable	Amplifier
-4dB	-7dB	-3dB	+38dB

Table 4.1: Attenuation of the cables, the antennas and amplification of the LNA. Where the negative sign indicates attenuation, the positive sign indicates amplification of the measured signal. The lower antenna gain at the South Pole is due to the snow ground, the antenna was laid on.

Pole. For comparison, measurements were also made in Wuppertal (Germany) at the Bergische Universität Wuppertal campus Grifflenberg.

The measured spectra have to be corrected by the attenuation of the antenna, the amplification of the LNA, and the attenuation of the cable. As this properties are frequency dependent, the measurements with the digital oscilloscope have to be Fourier transformed (Appendix C). Figure 4.3 shows the raw spectra measured at the South Pole and in Argentina. The larger correction factors are shown in Table 4.1. The correction for the amplifier and the cable is coming from data sheet.

The antenna simulation software EZNEC gives us the amplification of the antenna which is in our case an attenuation due to the impedance matching to the 50 Ω measurment system. The EZNEC code bases on the method of moments solution of the electric field integral equation for thin wires and the magnetic field integral equation for closed, conducting surfaces. NEC (Numerical Electromagnetic Code) is originally written in FORTRAN and is open source. The EZNEC antenna simulation software additionally has a number of standard components tabulated. Examples are coaxial cable, properties of ground properties and metal types for conductive elements. The antenna correction of the spectrum is only valid under the assumption of isotropy of the background in direction and polarization. At frequencies below 27 MHz the simulation of the antenna starts to get imprecise due to numerical limits.

Figure 4.4 shows that the corrected background spectra for Wuppertal, Argentina, and the South Pole and will be discussed in the following:

Continuous background spectrum at Pierre Auger Pampa Amarilla Argentina

At lower frequencies we see a steep fall off of the spectrum measured in Argentina before achieving the self noise of the spectrum analyzer at 35 MHz (Fig. 4.4). At 87 MHz the Argentina spectrum has clear signatures of anthropogenic radio emitters. From the last low frequency peak at 33 MHz up to 87 MHz the spectrum shows a
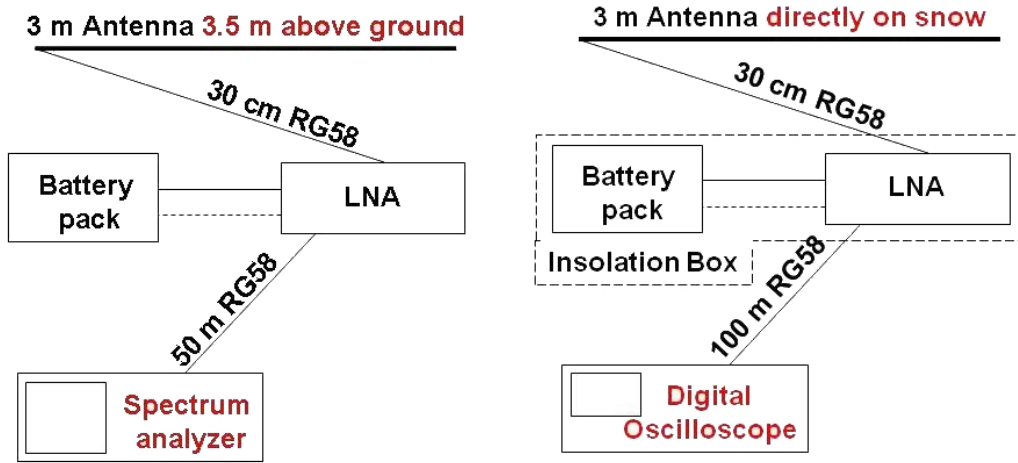
(a) The readout system of the antenna in Argentina is taken with a hand held Anritsu digital spectrum analyzer. The antenna was fixed horizontally on top of a wooden pole in 3.5 m height. After a short connection cable the signal is amplified with a 38 dB Miteq 50 Ohm LNA. The LNA was DC powered with a battery pack.

(b) The readout system of the antenna at the South Pole is taken with a 2 GHz Le Croy digital oscilloscope. The antenna was laying horizontally on the snow. After a short connection cable the signal is amplified with a 38 dB Miteq 50 Ohm LNA. The LNA was DC powered with a battery pack in an insulation Box.

Figure 4.1: Schematic view of radio background measurement setup with 3 m half arm dipole in Argentina and at the South Pole.

promisingly low background value for radio air shower detection. Thus, the LPDA antennas used for a Pierre Auger radio test array will start to measure in this region. Due to the antenna properties, the cable, and the LNA, the spectrum is valid with a systematic error of $+4.5; -5, 5$ dB above 27 MHz. The overall systematic error consists of three components. The LNA has a systematic error of $1, 5$ dB due to specification. The RG58 signal transmission cable leads to an uncertainty of 1 dB due to the connectors and cable length. The systematic error of the EZNEC antenna simulation is due to ground properties estimated to be 50% ($+2; -3$ dB)by changing the properties of the surface. For frequencies lower than 27 MHz the error increases due to numerical limits of the antenna simulation. The self noise of the hand held spectrum analyzer leads to the lowest possible value of -65 dBm/MHz depending on the settings we choose for the measurement. This explains the plateau of the spectrum in Fig. 4.3a at frequencies above 35 MHz.
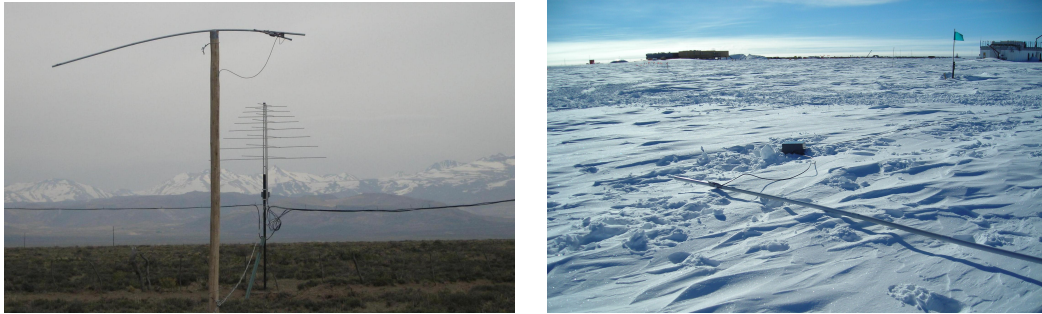
(a) The 3 m Antenna on top of a wooden pole in front of a LOPES logarithmic periodic dipole antenna.

(b) The 3 m Antenna is located on the South Pole snow, with the insulation box in the center of the picture.

Figure 4.2: Photographs of radio background measuring apparatus at the Pierre Auger site in Argentina and at the geographic South Pole in 2007.
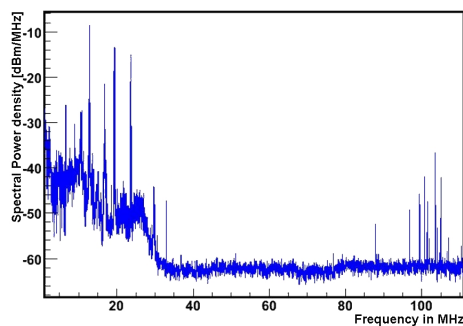
(a) Spectrum of the antenna setup in Argentina made with a hand held Anritsu digital spectrum analyzer. The lowest possible level of the spectrum analyzer was −65 dBm/MHz. Following a short connection cable the signal is amplified with a 38 dB Miteq 50 Ohm LNA. The LNA was DC powered with a battery pack.
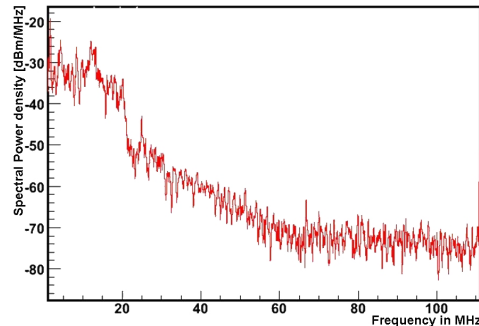
(b) Spectrum of the antenna at the South Pole made with a 1 GHz Le Croy digital oscilloscope. The antenna was laid down horizontal on the snow. Following a short connection cable the signal is amplified with a 38 dB Miteq 50 Ohm LNA. The LNA was DC powered with a battery pack in an insulation Box.

Figure 4.3: Raw spectra without antenna, cable and LNA correction of the measurements at the South Pole (right) and Pierre Auger site, Argentina (left).

Continuous background spectrum at the geographic South Pole

The main difference of the measurement at the South Pole and Argentina is the read out system. In case of the South Pole a 2 `GHz` digital oscilloscope was used to take single short time sweeps. For analysis the time sweep was Fourier transformed. From 27 `MHz` to 115 `MHz` the spectrum shows a featureless continuous fall off to thermal noise level (Fig. 4.4). Beside a peak of unknown origin at 66 `MHz` the spectrum at the South Pole is without any mono frequent noise emitters.
Except the read out device the same components where used at the South Pole and in Argentina. Thus the systematic error is comparable. The attenuation of the 100 `m` transmission cable in comparison to 50 `m` in Argentina leads to a minimal higher systematic error of $+4.7; -5.7$ `dB`. The gray band is a prediction of the galactic background from [45]. It is scaled up by 2 `dB` due to the difference between the mean antenna gain and the antenna gain in the direction of the galactic center (about 25° above the horizon). This value has an uncertainty of 4 `dB` due to unknow effects of the snow on the frequency dependent antenna gain near the horizon. In addition the position of the galactic center during the measurement is unknown. Our measurement is consistent with the galactic noise within the systematic error.

Continuous background spectrum at the Bergische Universität Wuppertal Germany

The measurement at the Bergische Universität Wuppertal is an example for the noise spectrum obtained in regions with high noise rates from civilization (Fig. 4.4). It is much higher and is dominated by various continuous radio emitting sources. The spectrum is recorded with a digital oscilloscope and has the same systematic errors as the other measurements.

4.3   Measurements at the South Pole with RICE in 2008

After measuring with one antenna at the South Pole for one day, the next step was to test a design for a permanent setup at the South Pole under the harsh weather conditions and measuring the EMI amount on the way to investigate a real test array. LNAs, for whole season tests, and antennas with horizontal directivity were installed at the South Pole to investigate the RFI conditions for air shower detection. In addition the infrastructure for future installations was tested.
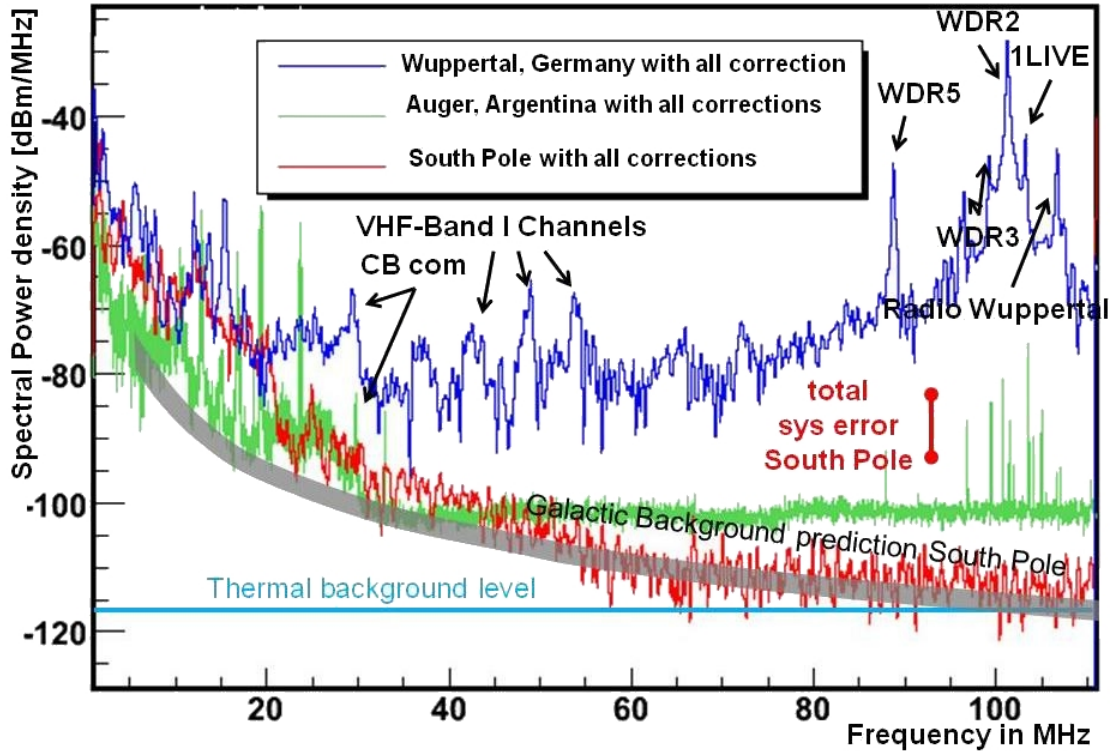
Figure 4.4: Measurements of the continuous background in Wuppertal, Germany at the Pierre Auger site, Argentina, and at the South Pole in the year 2007. The spectra in Argentina and at the South Pole are promisingly low. The spectrum measured in Argentina shows a couple of transmitters at frequencies below 27 MHz and above 87 MHz. The flatness of the Argentina spectrum is due to the self noise of the spectrum analyzer. The South Pole spectrum shows a continuous fall off to thermal noise level at 110 MHz. The spectrum at the Bergische Universität Wuppertal is an example for the background in regions with high civilization backgrounds. The error of the South Pole spectrum is $+4.7; -5.7$ dB. The gray band is a prediction of the galactic background from [45].

Cable	25 MHz				75 MHz			
	measured	length	Δ l	Δ att	measured	length	Δ l	Δ att
SP1	26.89 dB	627 m	7 m	0.3 dB	45.17 dB	652 m	32 m	2.2 dB
SP2	22.88 dB	547 m	47 m	2.1 dB	40.39 dB	579 m	79 m	5.5 dB

Table 4.2: Attenuation of the cables SP1 and SP2 connecting SPASE and MAPO building. The length is calculated from the attenuation and the specification of the cable. "Δ l" is the difference to the direct delay measurements. "Δ att" is the difference of the measured attenuation to the attenuation calculated from the measured delay and the cable specification.
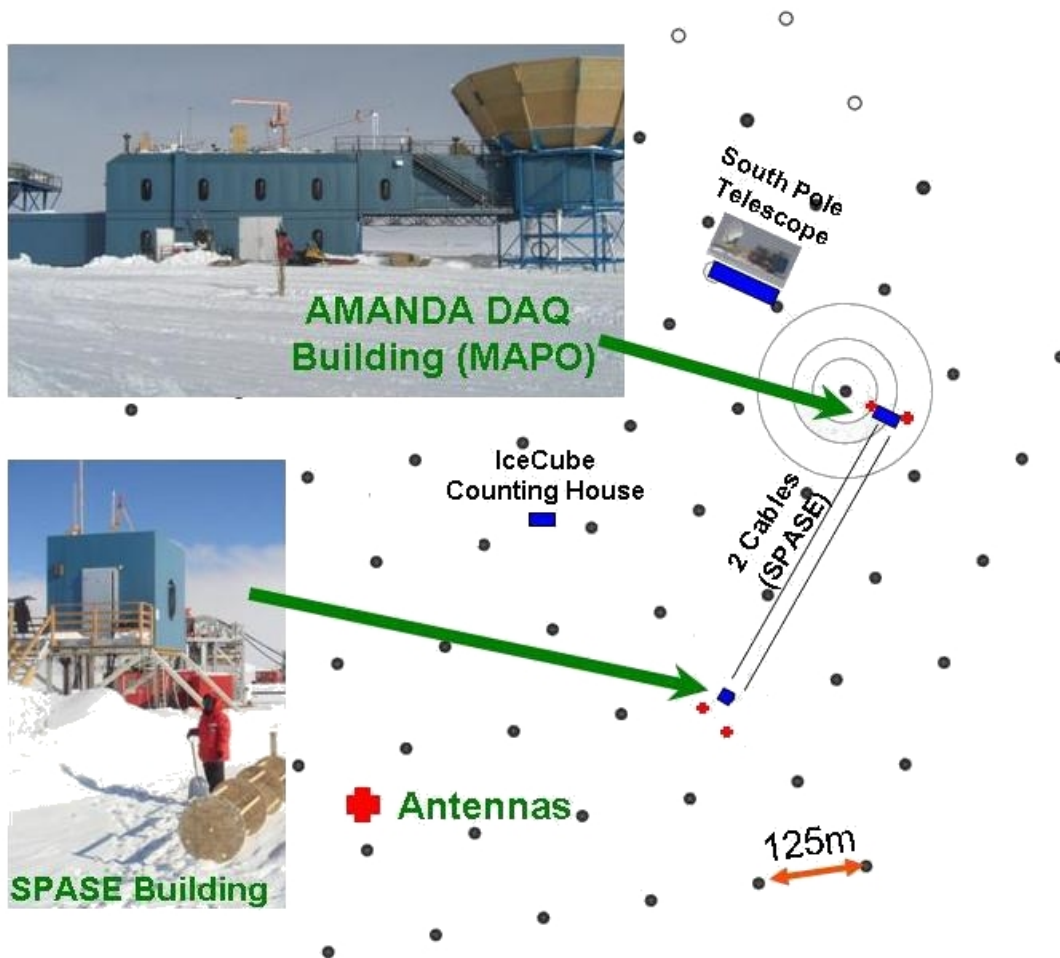
Figure 4.5: Map of the IceCube footprint with pictures of the SPASE2 and the AMANDA building. The black dots mark IceCube (Fig. 3.4) string positions. The blue rectangles mark the position of buildings on top of IceCube. The MAPO building is the housing of the RICE DAQ. The SPASE2 building is the old housing of the SPASE2 air shower detector and has two unused RG59 cable connections to the MAPO building.

Cable at frequency	Length from delay	Length from attenuation
SP1 at 25 MHz	620 ± 5 m	630 ± 2 m
SP1 at 75 MHz	620 ± 5 m	652 ± 6 m

Table 4.3: Attenuation of the cables, the antennas and amplification of the LNA. Where the negative sign indicates attenuation, the positive sign indicates amplification of the measured signal. The errors are uncertainties of the measurements and cable specifications. E.g. bad connectors of the SP2 cable during the attenuation measurement can explain the large discrepancy. The direct delay measurement was taken for time reconstruction.

Scheme 4.5 shows an overview of the present infrastructure at the South Pole. Miteq AM-1464 amplifier were installed at antennas on the roof of MAPO, which is the DAQ building of the AMANDA and RICE experiments. These MAPO roof antennas were added to the RICE DAQ as a surface hardware veto. In addition functional tests of RG59/U type Belden 1505A cables from MAPO to SPASE2 building were made for usage in the future. The delay of the two cables together was measured with single pulse runtime measurements. It is $4.48 \ \mu s \pm 0.01 \ \mu s$ with a difference of 475 ns to each other measured by the phase difference of signals through both cables shortcut. Table 4.2 gives an overview of measured attenuation with specification of the cables.

The attenuation of the cables was measured for 25 MHz and 75 MHz by sending a continuous waveform through the cables and comparing input amplitudes with output amplitudes. This measurement gives systematically higher values of the cable length than calculations from delay measurements compared with the cable specifications (see Tab. 4.2 and 4.3). For higher frequencies this effect seems to rise. Of course, the direct measurement of the cable delays was taken for time reconstruction and the direct attenuation measurements to correct on the strength of the signal. Figure 4.6 shows the measurements for the cable SP1 and SP2 at 25 MHz.

The discrepancy of this measurements with the cable specification has to be considered for future usage of the cables. The cause of the relatively high attenuation can be the age of the cables, bad connectors, or a difference from specification due to the low temperatures. This cable are used for a small test array in 2009.

4.4 Measurements at the South Pole in 2009

The antenna design for long term measurements of the radio background from $25 - 100$ MHz at the South Pole was the "Fat Wire-Dipole". Figure 4.7 shows a Fat Wire-
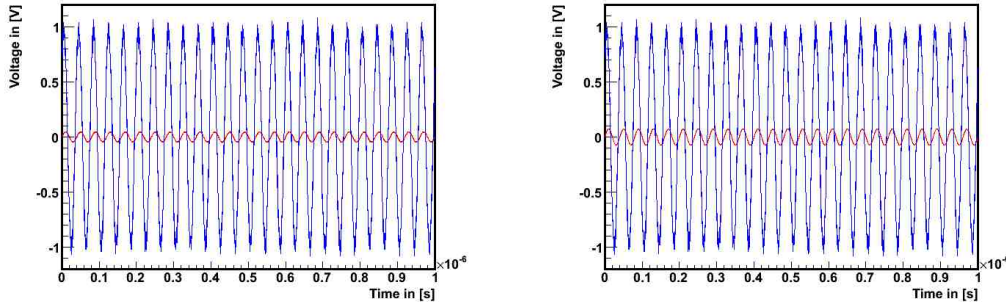
(a) Attenuation measurement of the cable SP1 between SPASE and MAPO. The attenuation is calculated to be 26.89 dB with a systematic error of ± 1 dB. The blue sine is the input signal. The red sine is the signal after passing the cable.

(b) Attenuation measurement of the cable SP2 between SPASE and MAPO. The attenuation is calculated to be 22.88 dB with a systematic error of ± 1 dB. The blue sine is the input signal. The red sine is the signal after passing the cable.

Figure 4.6: Attenuation measurements with continuous waveform.
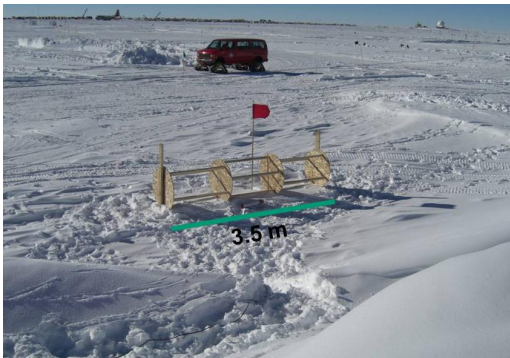
(a) Picture of a Fat Wire-Dipole at the South Pole near the SPASE2 building.
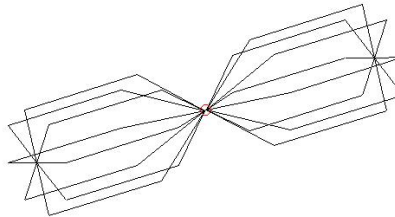
(b) Drawing of the conducting elements of the Fat Wire-Dipole for NEC simulation.

Figure 4.7: Fat Wire-Dipole of 3.5 m length.

Dipole near the SPASE building and a technical drawing of the conductive elements from NEC antenna simulations. Two Fat Wire-Dipoles were connected to the RICE DAQ together with two four half arm dipole antennas on the roof of the MAPO building (Fig. 4.5). The result is a system of four surface antennas.

4.4.1 Fat Wire-Dipole

The baseline requirements of antennas for a radio air shower detector at the South Pole lead to a number of antenna properties:

- Bandwidth: geo-synchrotron radio pulses are broad band in frequencies from $1 - 100$ MHz, where most of the power is emitted in the low frequencies as will be discussed in Sec. 5.1. Therefore the antenna should have good amplification at low frequencies.

- Polarization: As the geo-synchrotron emission of air showers has an east-west polarized and a north-south polarized but negligible vertical component, the antennas should be horizontally polarized.

- Directivity: From geo-synchrotron emission theory, the emitted signal is roughly proportional to $\mathbf{v} \times \mathbf{B}$, where $\mathbf{v}$ is the velocity vector of the electromagnetic charges. Moreover, horizontal air showers are the most important background for IceCube EHE neutrino detection (cf. Chapter 6.2). To reach a detection efficiency for horizontal air showers the antennas should have a good sensitivity in horizontal direction.

- Other: In contrast to other places on earth, the ground at the South Pole is very homogeneous and independent of weather conditions. Thus the antenna has not to be independent on the properties of the ground.

- Physical properties: An antenna at the South Pole has to withstand the extreme weather conditions at the South Pole. These are high wind speeds and extreme low temperatures under very dry conditions.

The wavelength where the antenna is sensitive scales with the size of an antenna. This means the larger the antenna the lower is the frequency it can detect. Of course engineering arguments limit the size of the antenna due to the installation procedures and transport. It was decided to have the antenna not larger than 3.5 m with a diameter of 70 cm. This corresponds to a resonance frequency of 43 MHz for a simple dipole in free space. The Fat Wire-Dipole was found to have an acceptable gain for horizontal emission (see Fig. 4.8), is relatively broad band in acceptance and has, without impedance matching, a reflection coefficient lower 0.6. The properties of antennas are discussed in more detail in Appendix A. To estimate the antenna properties of the Fat Wire-Dipole, NEC simulations with snow ground were made. The snow ground is assumed to have a dielectric constant $\epsilon = 3$ and a specific conductivity of $\sigma = 1 \cdot 10^{-9} \frac{A}{Vm}$ [72]. Figure 4.8 shows an example for the gain pattern of the Fat Wire-Dipole at 33 MHz. At $25°$ above the horizon the gain is still above -5 dBi (dB in relation to an isotropic radiator) where the maximum gain at 33 MHz is -0.04 dBi in vertical direction.

For electromagnetic waves with vertical inclination the FWD has its maximal gain.
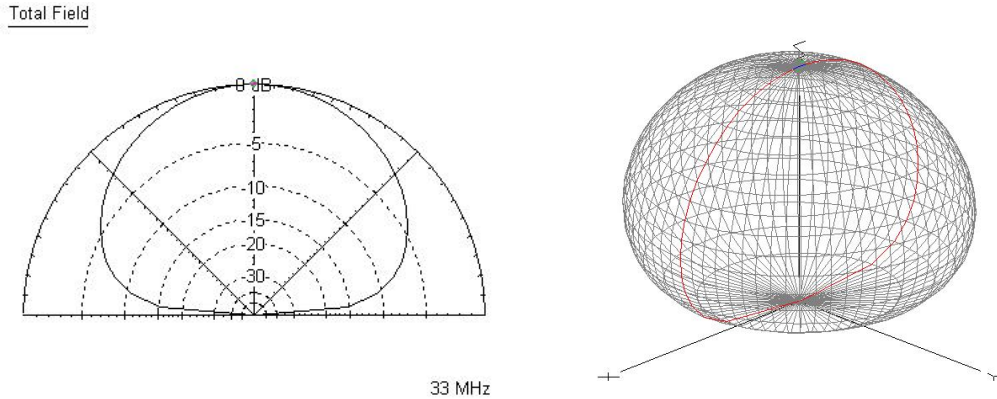
(a) Field pattern of the gain of the Fat Wire-Dipole at 90° to the dipole axis. The gain is at 25° above the horizon still -4.35 dBi.

(b) 3D field pattern of the gain of the Fat Wire-Dipole. The antenna lays in x direction on the x-y plane.

Figure 4.8: Gain pattern of the Fat Wire-Dipole at 33 `MHz`. The outer ring corresponds to -0.04 `dB` in vertical direction relative to an isotropic radiator. All values are results from NEC simulations with simulated snow ground ($\epsilon = 3$ and $\sigma = 1 \cdot 10^{-9}$ $\frac{A}{Vm}$).

The received electromagnetic wave has the same polarization as the antenna.

If a electromagnetic wave has an inclination orthogonal to the antenna axis, the component with the same polarization is still received. This signal is now influenced by reflections on the ground and gets weaker for more horizontal waves. For very inclined waves the superposition of the direct and the reflected waves lead to a strong absorption effect.

For electromagnetic waves with some inclination and not orthogonal to the antenna axis, the wave is projected on a smaller effective length of a thin dipole antenna. Thus the gain gets smaller for a the dipole in free space (cf. Fig. 4.9) compared to the gain of a wave orthogonal to the antenna axis. For the FWD with 70 `cm` diameter this effect is much weaker, as the effective length of the antenna is more constant. For more horizontal waves the signal gets weak again, due to ground reflection effects.

The overall maximum gain of the FWD is 4 `dBi` in vertical direction at 80 `MHz`.

To compare the Antenna properties at the South Pole with results from simulations the VSWR (Voltage Standing Wave Ratio) was used:

$$VSWR = \frac{V_f + V_r}{V_f - V_r},$$

(4.1)

(a) Field pattern of the gain of a thin dipole antenna in 0° elevation.

(b) 3D field pattern of the gain of thin 3.5 m dipole antenna. The Antenna lays in y direction on the x-y Plane.
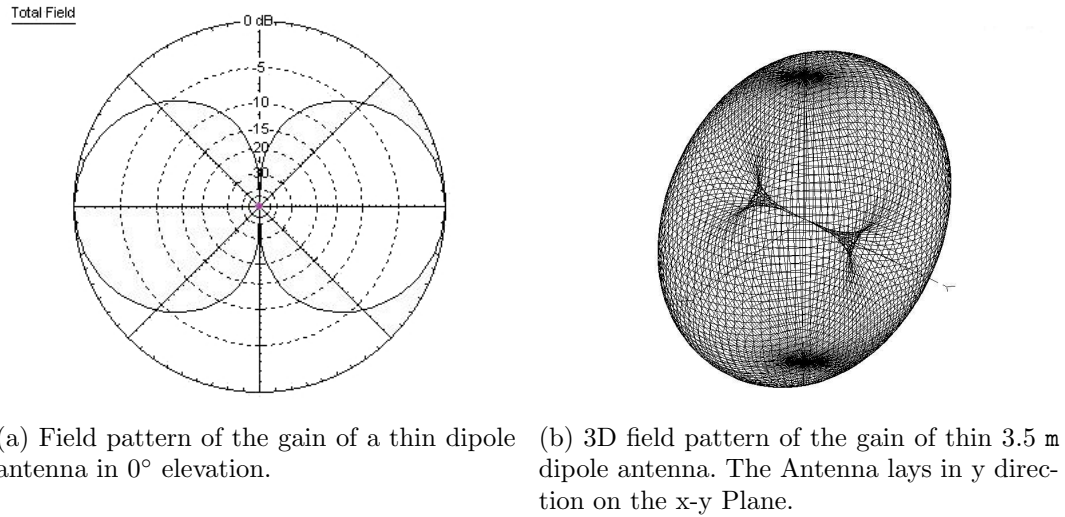
Figure 4.9: Gain pattern of a thin 3.5 m dipole antenna at 33 MHz in free space.

where V_f is the effective voltage of the incoming signal and V_r is the voltage of the reflected signal. The interference of the emitted continuous waveform and the reflected signal is a standing wave, where the maximal amplitude is $V_f + V_r$ and the minimum is $V_f - V_r$.

One can calculate the emitted power of an antenna if one knows the incoming and the reflected signal due to energy conservation. The ratio of the incoming signal to the reflected signal in the emission case is equivalent to the ratio of the received signal to the signal sent.

$$r_{ant} = \frac{V_{rsender}}{V_{antinput}} = \frac{V_{rreciver}}{V_{space}}, \tag{4.2}$$

where $V_{antinput}$ is the input voltage into the antenna in the emission case and $V_{rsender}$ is the reflected signal. V_{space} is the effective voltage of the electromagnetic wave at the antenna in the receiving case, where $V_{rreceived}$ is the reflected signal at the receiving antenna. r_{ant} is called reflection coefficient, where

$$e_{ant} = 1 - r_{ant} \tag{4.3}$$

is the emission coefficient. This is only valid, if the thermal loss by resistance is negligible, which is the case for antennas consisting of materials with low electrical resistance.

A comparison of the VSWR of a Fat Wire-Dipole measured at the South Pole with simulations shows some discrepancies (cf. Fig. 4.10). The cause for the discrepancy can be ground effects not included in the simulation, such as reflection on increasing snow density with depth. In general the results of the VSWR from simulations
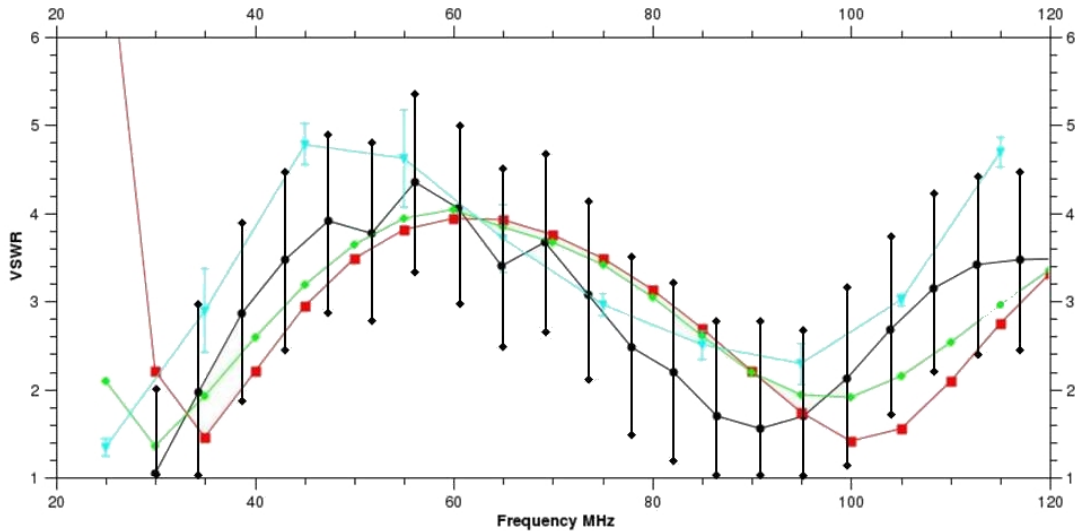
Figure 4.10: VSWR of the Fat Wire-Dipole. The Black curve shows the VSWR measured South Pole with a $Z = 50$ Ω system. Due to unknown properties of the electrical ground at the South Pole the calibration of the measurement at the South Pole leads to high uncertainties of ± 1. The green curve shows simulations with snow ground, the red curve in free space. The turquoise curve shoes the mean of several measurements in Wuppertal with statistic error. An VSWR of 4 is equivalent to a reflection coefficient of 0.6.

are in acceptable agreement with measurements at the South Pole up to 120 `MHz` within ± 1, due to uncertainties on the electric ground conditions at the South Pole. It is realistic that the VSWR of the FWD is lower at the South Pole in comparison to Wuppertal, caused by the snow ground. The systematic shift of the simulation of the VSWR to higher frequencies, hints to errors in the simulation caused by the resistance of the connections of the conductive wires on the top of the dipole arms. This was modified for newer FWD antennas.

4.4.2 Implementation into RICE

In addition to the four half arm dipole antennas deployed on the roof of the MAPO building in 2008, two Fat Wire-Dipoles were added to the RICE readout system. The antennas were installed near the SPASE2 building (Fig. 4.5). They were connected with long RG59 coax cables after the bandpass filters and amplifiers. Figure 4.11 gives a schematic view of the setup. To avoid saturation of the LNA a 25 `MHz` high pass filter was installed between antenna and amplifier. After the MITEQ AU-4A-0150 amplifier the signal has to propagate through the SPASE-MAPO RG59 cables
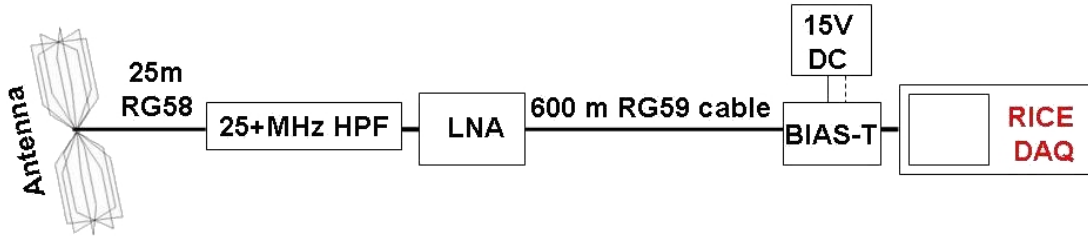
Figure 4.11: Connection scheme of the Fat Wire-Dipole to the RICE DAQ. Following the antenna, the signal is propagated through 25 m RG58 cable, the signal is attenuated with a 25 MHz high pass filter (HPF) in order not to saturate the LNA. Then the signal is amplified with a MITEQ 60 dB amplifier and after 600 m RG59 cable recorded with the RICE oscilloscopes. The power for the LNA is fed in the signal cable via a bias-T.

Antenna	x [m]	y [m]	z [m]	cable delay [ns]
MP1	47	-28.0	18	144 ±2
MP2	25	-20	18	129 ±2
SP1	-135	-366	1	2124 ±3
SP2	-148	-348	1	2729 ±3

Table 4.4: Antenna position and cable delays to the RICE DAQ. The positions of the antennas were measured by surveyor. The error of each position is estimated to be in the region of ±1 m

and is recorded by the RICE oscilloscopes. The power of 15 V DC to run the LNA is feed in the signal cable via a bias-T. Table 4.4 gives the distances of the antennas in the RICE coordinate system. The antennas connected to the SP1 and SP2 cables deployed near the SPASE2 building have a distance of 23 m to each other, where the antennas on the roof of the MAPO MP1 and MP2 antennas have a distance of 24 m to each other. The distance of SP1 antenna to MP1 antenna is 384 m. The SPASE antennas are part of the readout system, but they are not implemented into the RICE trigger system. The MAPO roof antennas are still connected to the "Hardware Veto" channels of the RICE trigger logic like in 2008.

4.4.3 Analysis and results

In 2009, RICE took 56 GB of data, 200 000 events with 10 000 minimum bias events and 50 000 HST events. In addition there are several runs with a couple of hundred events with an external source to test general functionality and source reconstruc-

tion.

Source reconstruction test

To test the event reconstruction algorithm, we used pulsed signals generated with a `GHz` horn antenna in front of the MAPO building. Figure 4.5 shows the MAPO building on the IceCube footprint. The received pulses of the pinger for all surface antennas show a characteristic signature (Fig. 4.12) saturating the ADC. In the events of the antennas near the SPASE2 building one can see two pulses per event and a drop off of the oscilloscope voltage level. The first pulse is directly fed into the RICE receiving system as RICE and the pulser use the same power supply. After that, the pulse of the horn antenna is emitted. This leads to some charge effect in the electrical ground of the MAPO building which influences the baseline of the RICE oscilloscopes. The electrical ground drops down. After the propagation time of the pulse through the air to the SPASE antennas one can observe the pulse with the antennas. This is the second pulse at the end of the time sweep.

A χ^2 minimization on time residuals can be used to reconstruct the source location of single events. The algorithm was to minimize matrix elements A_{ij} with $i \neq j$ of the 4×4 matrix $\mathbf{A}$ consisting of the signal time and positions of the antennas. Considering the cable delays and the exact antenna positions (see Table 4.4) we are able to make a 3D and time reconstruction of the events. Figure 4.13 shows that the reconstruction with pinger data is working well. It is accurate within several meters and shows clearly that the pinger is located in front of the MAPO building near the antenna MP1. The RMS of the reconstructed pinger data is 2.3 `m` corresponding to 7 *ns* time uncertainty.

Continuous background

Because of the well known properties of the single components of the SPASE antennas, it is possible to extract a spectrum of the continuous background and monitor this over a whole South Pole winter. Based on the drawing in Fig. 4.11 one can make a step by step calibration. This method takes into account each component of the device and determines a correction value $corr(f)$. Thus each electronic part has to be described as a function of frequency. The received power $P(f, \theta, \phi)_{ant}$ of the antenna can be described by Equation 4.4:

$$P(f, \theta, \phi)_{ant} = \frac{c^2}{4\pi \cdot f^2} \cdot G(f, \theta, \phi) \cdot \frac{1}{\mu_0 \cdot c} E^2, \qquad (4.4)$$
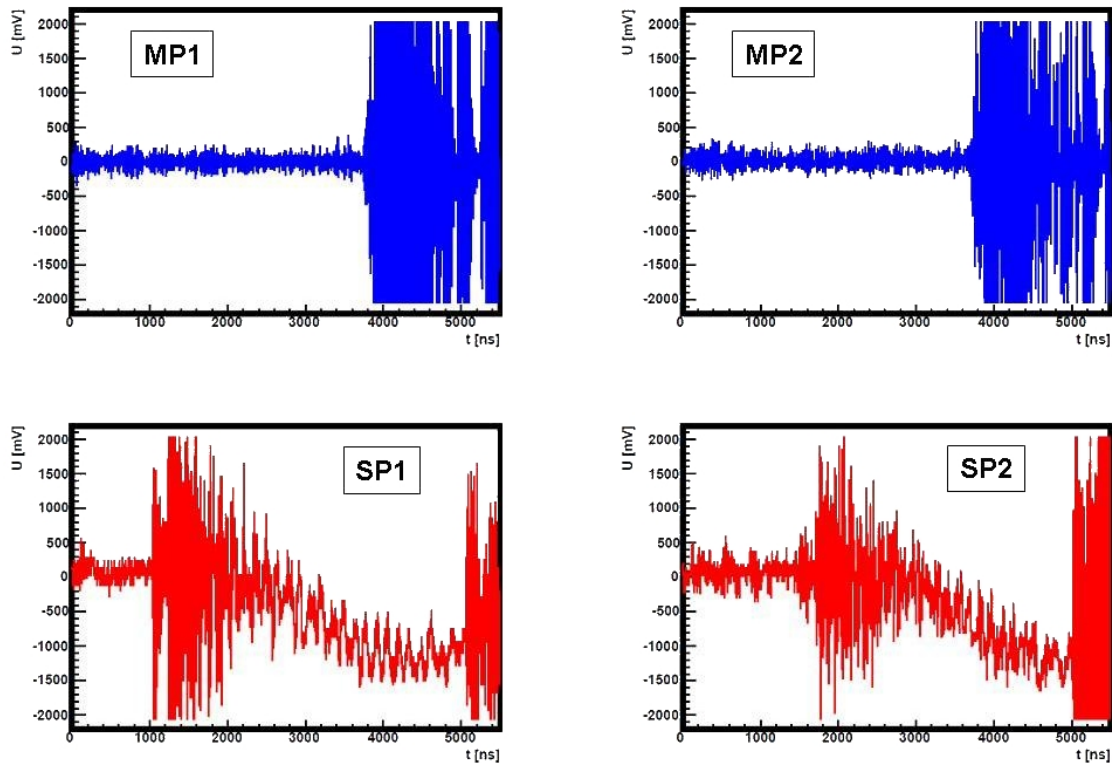
Figure 4.12: Signal from a pulse emitted through a `GHz` horn antenna observed in the surface antennas. All pulses are corrected for the cable delays noted in Table 4.4. The upper left pulse is received by the MAPO roof antenna MP1. As in the upper right picture of the signal in MP2 immediately saturates the 12 Bit RICE oscilloscope. The lower two graphs show first a prepulse of the horn antenna fed into the DAQ on a direct way via the signal cables and power supply. Then the electrical ground in the MAPO building drops down, due to the strong pulse. After the propagationtime of the pulse through the air to the SPASE antennas SP1 and SP2 the pulse saturates the RICE oscilloscopes as well in this channel.
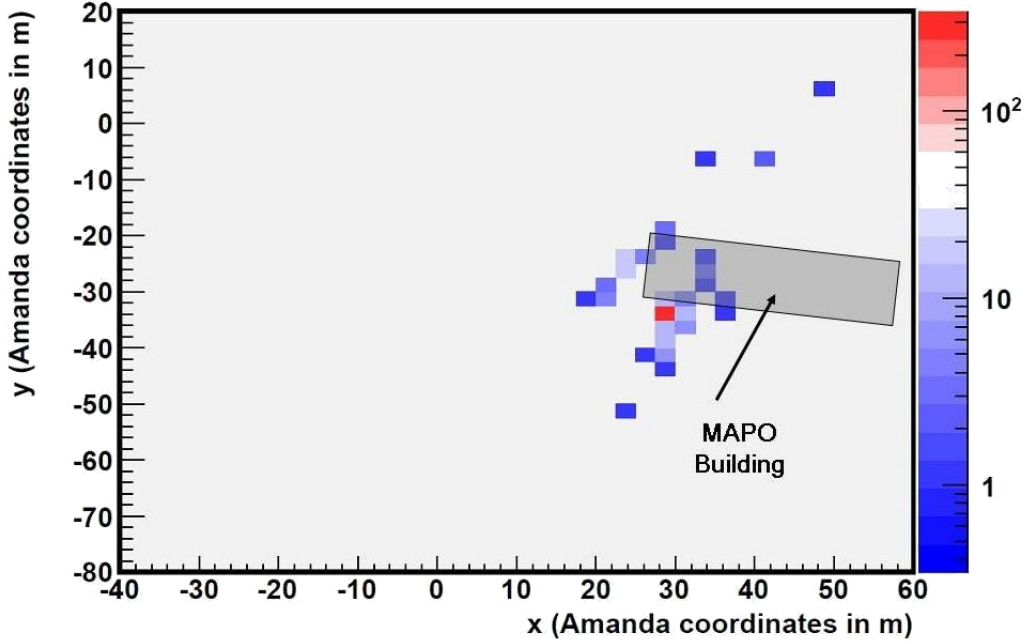
Figure 4.13: χ^2 reconstruction of the pulses from the GHz horn antenna. The pinger signals are clearly reconstructed to the position of the the horn antenna in front of the MAPO building. The color indicates the number of events in each bin.

where $G(f, \theta, \phi)$ is the gain of the antenna in dBi. The values for $G(f, \theta, \phi)$ are coming from simulation. This is discussed in some more detail in Appendix A. As we have voltage U against the impedance $Z(f)_{ant}$ of the antenna direct behind the antenna, the power is:

$$P(f, \theta, \phi)_{ant} = \frac{U^2}{Z(f)_{ant}}, \tag{4.5}$$

where $Z(f)_{ant}$ is the impedance of the Antenna. Due to the impedance match of the antenna to the measurement system with a $Z = 50\,\Omega$, the voltage at the voltmeter is reduced by the emission coefficient $e(f)_{ant}$. The emission coefficient $e(f)_{ant}$ is coming from simulation and is compared to measurements of the VSWR (Sec. 4.4.1). Thus the received power at the Voltmeter is:

$$P(f, \theta, \phi)_{ant} = \frac{U^2}{50\,\Omega} \cdot e_{ant}(f)^2. \tag{4.6}$$

In addition the signal is attenuated and amplified by all other elements in the signal path (Fig. 4.11):

$$P(f, \theta, \phi)_{total} = P(f, \theta, \phi)_{ant} \cdot \frac{a_{amp}(f)}{a_{RG58}(f) \cdot a_{HPF}(f) \cdot a_{RG59}(f) \cdot a_{Bias-T}(f)}. \quad (4.7)$$

Here $a_{amp}(f)$ is the power amplification factor of the LNA and $a_{RG58}(f)$, $a_{HPF}(f)$, $a_{RG59}(f)$, and $a_{Bias-T}(f)$ are the attenuation factors of the RG58 cable, the 25 `MHz` high pass filter, the long RG59 cable, and the Bias-Tee, which has limited impact.

In the case of isotropic radiation, one can define a mean gain of the antenna by averaging over θ and ϕ. For the cosmic background, we have to average over the hemisphere. This leads to a calibration factor independent of the direction.

Thus a spectrum of the continuous background under the assumption of isotropy can be made. A typical spectrum from an 8 μ`s` sample is shown in Fig 4.15. Due to the large uncertainties of the attenuation of the long signal cables the systematic error is estimated to be $+3$ `dB`; -5 `dB`. The gray band is a prediction of the galactic background from [45]. It is scaled down by 3 `dB` due to the difference between the mean antenna gain and the antenna gain in the direction of the galactic center at about 25° above the horizon at the South Pole. The measured signal of the galactic noise has an uncertainty of 5 `dB` due to unknow effects of the snow on the frequency dependent antenna gain near the horizon and the position of the galactic center relative to the antenna during the measurement. Our measurement is consistent with the galactic noise within the systematic error.

Figure 4.14 shows the uncorrected spectrum and the correction functions of the single components of the test setup. The high pass filter is cutting the measured spectrum at < 25 `MHz`. As the high pass filter is directly in front of the Antenna, we know that we are receiving antenna signals.

VLF antenna noise

The VLF (Very Low Frequency) antenna experiment is built to investigate properties of the ionosphere. The idea is to send very low frequency electromagnetic waves and receive the signal [57]. This signal gets reflected at the ionosphere and can be received hundreds of kilometers away to measure its properties. The VLF antenna at the South Pole (see fig. 4.16) is resonance frequency of 19.6 `kHz`; the radiated power is about 500 `W`. It is emitting every 15 `min` for a duration of 1 `min` [53]. This signal is received by the signal cables between SPASE2 and MAPO which is an important background. Figure 4.18 shows VLF signals of the transmission cables from SPASE to MAPO without an antenna connected, as compared to an open oscilloscope channel in the MAPO building at the same time. The phase transition
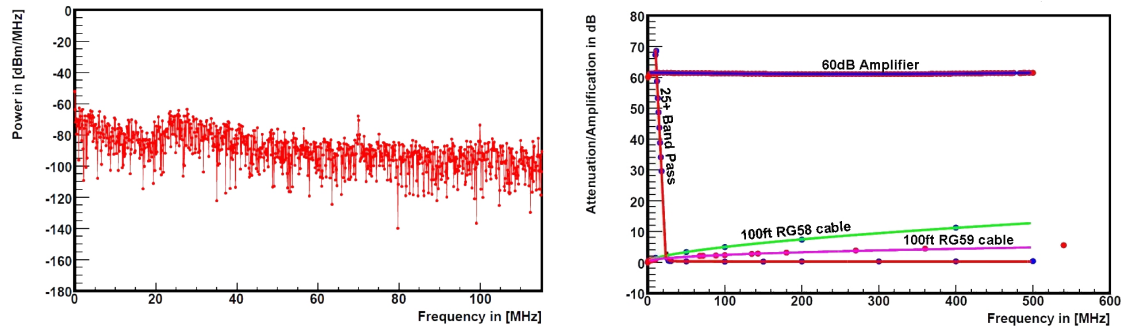
(a) Example spectrum of a RICE minimum bias 8 μs sample of the SPASE2 antenna. At 25 MHz the high pass filter is cutting into the measured spectrum.

(b) Background correction functions of the different components of the SPASE antenna setup.

Figure 4.14: Uncorrected minimum bias spectrum of the SP2 antenna from March 2009 and the background correction functions used to obtain the spectrum seen in Fig. 4.15.
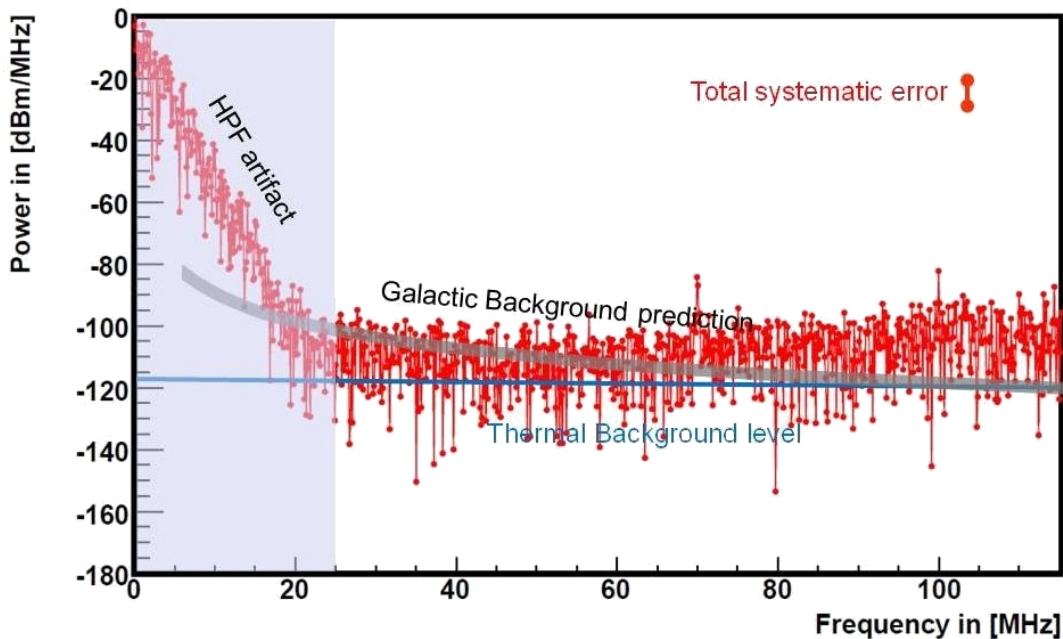
Figure 4.15: Background spectrum of a 8 μs sweep corrected for the effects of cable, filter, and amplifier. The spectrum strongly increases below 22.5 MHz since the filter correction is not valid for thermal background noise from the oscilloscope itself. Due to the large uncertainties of the attenuation of the long signal cable the systematic error is estimated to be +3 dB;−5 dB. The gray band is a galactic background prediction from [45].
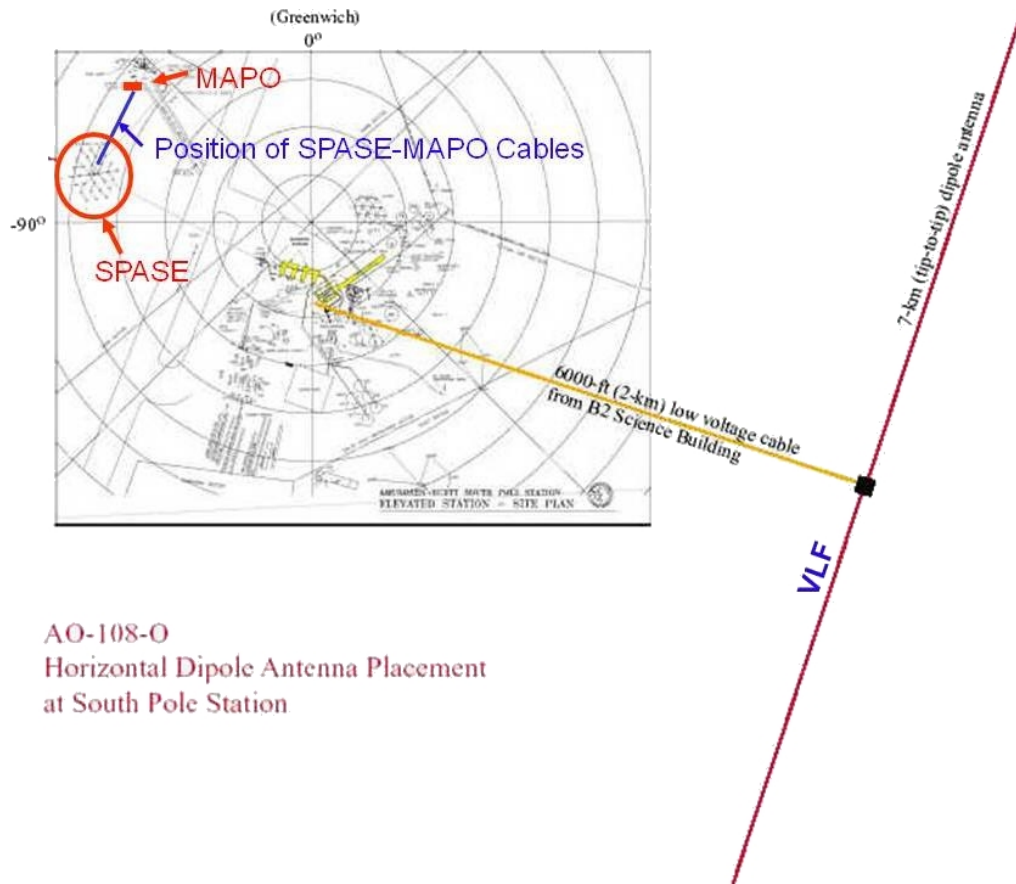
Figure 4.16: The VLF antenna layout at the South Pole. The 7 `km` long dipole transmitter of 19.6 `kHz` is used to measure the properties of the ionosphere. The strong signals every 15 `min` are inadvertent received by the signal cables from SPASE to MAPO [76].

between the two cables is due to the inductance of a cable spool of the 150 `m` longer SPASE2 cable [1]. It clearly shows the VLF signal is induced in the signal cable. Figure 4.17 shows a typical VLF event in the SPASE antenna channels. Future radio experiments with analog signal transmission over long cable distances at the South Pole have to be aware of this strong low frequency radio source.

---

[1] A oscillating circuit with $L >> C$ and negligible small impedance Z has a phase transition of $\pi/2$ compared to a balanced circuit.
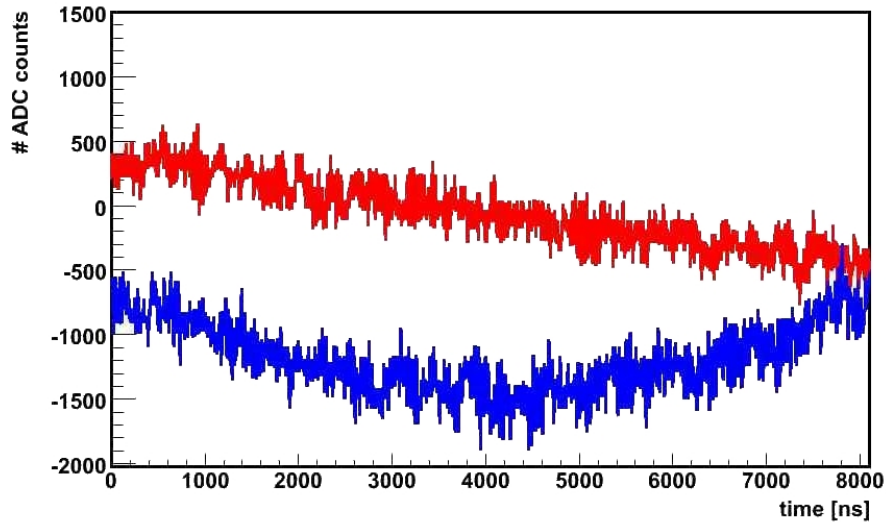
Figure 4.17: The VLF antenna at the South Pole is a strong emitter of low frequency pulses [76]. Measurements during VLF emission time show a strong low frequency component superimposed on the high frequency antenna signal. The red line is an event measured with SP1, the blue line a pulse measured with SP2.
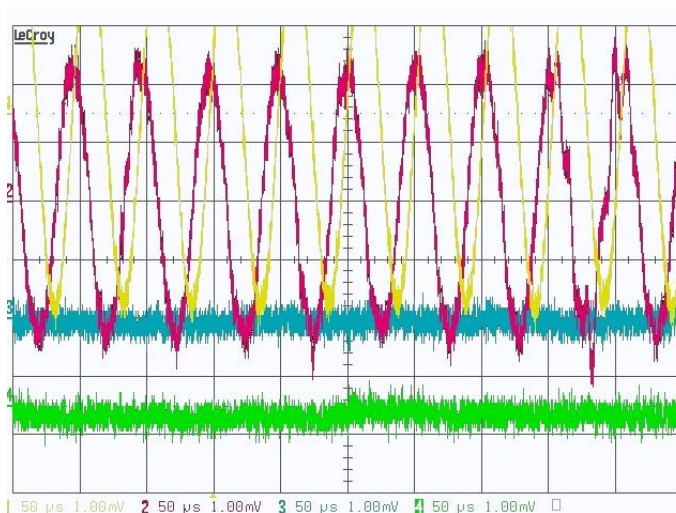
Figure 4.18: The VLF antenna at the South Pole is a strong emitter of low frequency pulses [76]. The yellow and red curve show the received signal of the open cables connecting MAPO and SPASE building. The blue and green curve are oscilloscope channels with 1 m RG58 and open channel.

Chapter 5

SIMULATION AND MEASUREMENT RESULTS

To estimate the pulse structure, the signal to noise ratio (SNR), and the duration of air shower radio pulses in a possible radio air shower detector at the South Pole, one has to have air shower pulse predictions. This pulse predictions have to be compared with given background measurements. Such background measurements in the year 2009 together with calculations with the REAS2 code are the basis of a prediction for possible air shower detections.

5.1   REAS2 Pulse Predictions

The REAS2 simulation code is currently the most realistic air shower radio emission code available. Studies [50] have shown that the REAS code is able to describe the field strength of LOPES for air showers of 10^{17} eV to 10^{18} eV in 100 m distance from the shower core within one order of magnitude (see for example Fig.2.11). The code is used as a basis to investigate signal predictions of EAS at the South Pole.

CORSIKA based REAS2 simulation

The REAS2 code is based on CORSIKA simulations and propagates charged particles, mostly electrons and positrons, through the earth magnetic field and superimposes the emitted synchrotron radiation. Basis of our simulation effort were CORSIKA simulations of proton primaries with QGSJET1 [39]. The earths magnetic field at the geografic South Pole was parametrized by: $|H| = 0.55361$ G with an inclination angle of $\theta_{incl} = -72.5423°$ relative to the detector plane. The minus indicates that the direction of the magnetic field vector at the southern hemisphere points down. The declination of the magnetic field at the South Pole, like in Fig. 5.1,

is $\phi = 14.77°$ East of North, where the North direction is set to longitude $0°$. The altitude of the observer is set to 2800 m. CORSIKA air showers -one for each set of parameters- were simulated with primary proton energy of 10^{15} eV, 10^{16} eV, 10^{17} eV, and 10^{18} eV. For each energy, inclination angles of the air shower from $\theta_{incl} = 0°$ to $45°$ in $5°$ steps were simulated, where $0°$ is vertical to the detector plane. The ϕ of the shower axis was varied between $0°$ and $180°$ due to symmetry effects. It was spaced in $25.75°$ steps.

The resulting trajectories of the leptons (only $\mu^{\pm}$ and $e^{\pm}$) are fed into the REAS2 simulation to calculate the radio emission. The REAS2 output is the electric field strength in East-West (EW), North-South (NS) and vertical (V) polarization of air showers simulated for various distances of the observer from the shower core (the impact point of the shower axis on the ground), and direction of the air shower in the time domain. In detail REAS2 simulations of each CORIKA shower were made in $d = 25$ m, 125 m, 225 m, 325 m, and 525 m distance of the observer to the shower core with the directions of the observer ϕ_{dir} in $25.75°$ steps from $0° - 180°$ and the angle of the observer to the shower axis ϑ_{ant}. Figure 5.2 shows the discussed values. An example of the REAS2 output pulses is given in Fig. 2.9.

5.2   Background Comparison

To compare the simulation results with background measurements at the South Pole and to estimate the pulse heights in a possible air shower test array, the raw radio pulses have to be corrected for the antenna response and the electronic components like high pass filter, cable and amplifier.

5.2.1   Simulated radio air shower pulses

In our case we fold the simulated pulses with the response of the antenna given by Equation 4.4, where $G(f, \theta, \phi)$ is obtained from EZNEC simulations. These simulated pulses are filtered with the response of a 25 MHz high pass filter and a 200 MHz low pass filter applied in the 2010 Test Array (cf. Section 6.1).

5.2.2   Background correction

The raw background spectra have to be corrected for the cable attenuation and the LNA amplification of the components shown in Fig. 4.11. The background spectrum has not to be corrected for the Antenna response and the electrical filters

as the simulated signals are already corrected with the Fat Wire Dipole (FWD) response function and are filtered with high and low pass filter. This was done for background spectra measured with the antennas near the SPASE building at the South Pole.

These corrected REAS2 radio pulses can be compared with the corrected realistic background spectra.

5.3   Discussion

An exemplary background signal of the SP1 antenna is shown in Fig. 5.3 together with a weak air shower pulse. The RMS of the time sweeps is typically 5.3 μV for background measurements of the SP1 and SP2 antenna at the South Pole during the Antarctic winter after correction for cables and amplifiers.

The influence of the bandpass chosen for radio detection can be seen in Fig. 5.4. For the shown pulse, the amplitude is lower by a factor of 0.6, when reducing the band pass from $25 - 200$ MHz to $50 - 200$ MHz. Pulses with amplitudes of several hundred μV are predicted at distances smaller 125 m for an air shower energy above 10^{17} eV. An example is given in Fig. 5.5.

In the energy region of 10^{17} eV and distances of about 100 m to the shower core, REAS2 predictions and measurements of LOPES are in good agreement, what confirms our estimations in Section 6.1. The amplitude of radio signals from air showers strongly dependent on the distance of the observer from the shower core. Figure 5.6 shows the signal strength of a 10^{17} eV proton induced air shower in several distances to the shower core. An exponential fit describes the data to distances up to 300 m and helps to estimate the pulse strength between 75 m and 300 m.

The pulse strength is rising with increasing inclination angle due to the longer propagation length of the particles through the magnetic field, larger $\mathbf{v} \times \mathbf{B}$ values and projection on the detector plane. Figure 5.7 shows the scaling factor on the pulse heights in the FWD antenna depending on the inclination angle of an air shower coming from South. The antenna position is $\vartheta_{dir} = 45°$. The EW polarized pulse amplitudes are increasing with inclination angle.
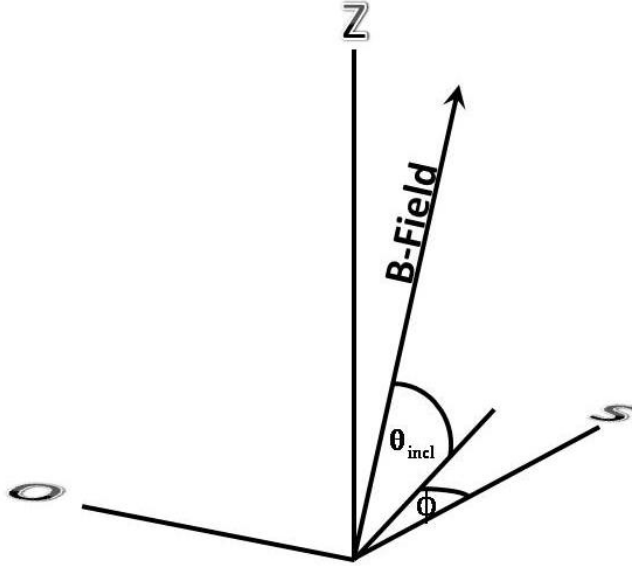
Figure 5.1: B-field vector at the South Pole relative to the detector plane. The inclination angle is $\theta_{incl} = -72.5423°$. The minus indicates that the B-field vector points down at southern hemisphere. The declination of the magnetic field at the South Pole is $\phi = 14.77°$ East of North.

The radio pulse height follows linearity with the energy of the primary particle, as can be seen in Fig. 5.8 for $E_{prim} = 10^{15}$ eV $- 10^{17}$ eV pulses. This is due to the linearly increasing number of charged particles and their coherently added pulses.

However, a complete parameterization of the radio pulse from air showers measured with an antenna array is complicated due to the large number of parameters. Hence we can only estimate the detectable flux of a radio air shower array with FWDs detecting radio signals of air showers with the following properties:

- The primary **energy** of cosmic rays should be higher than 10^{16} eV to get amplitude heights, high enough for an 6 σ amplitude threshold trigger. At primary energy of 10^{17} eV the radio signal should be strong enough to be detected at more than 100 m distance to the shower core.

- The **inclination angle** of the incoming air shower should be lager than 30° but not lager than 60°. At lager inclination angles the predictions of the REAS2 simulation get unrealistic due to a missing implementation of the earth curvature on the detector plane. Vertical air showers are estimated to have weaker radio signals due to projection effects on the detector plane and the inap-
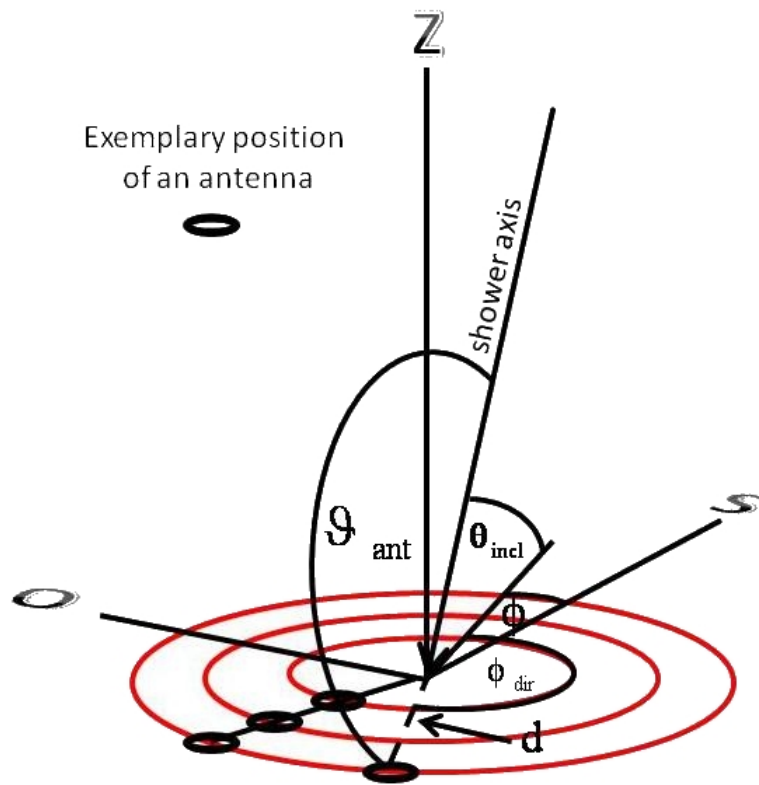
Figure 5.2: Geometrical parameters of simulated air showers and observers at the South Pole. The inclination angle is of the air shower is θ_{incl}, the longitude is ϕ. ϕ_{dir} and d define the position of the observing antenna on the ground, where d is the radius of the red circles.
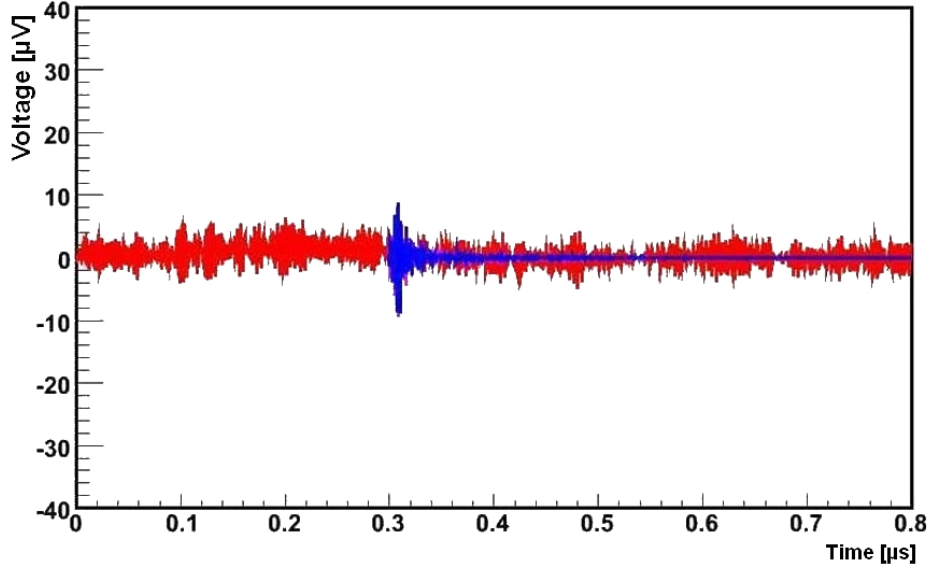
Figure 5.3: Typical waveform of the background at the South Pole measured with SP1 antenna, corrected for LNA and Cable response (red line). The blue pulse is the EW polarized radio emission part of a simulated proton induced air shower with a primary energy of 10^{17} `eV`. The distance from the shower core d is 225 `m` with $\theta_{incl} = 45°$ and $\vartheta_{ant} = 45°$. The pulse is corrected for the antenna response, a 25 `MHz` high pass filter and a 200 `MHz` low pass filter.
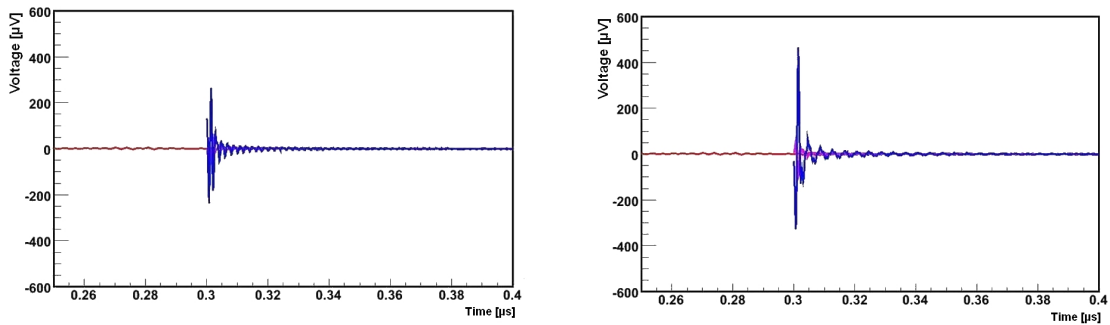
(a) Pulse after antenna and $50 - 200$ `MHz` band pass.

(b) Pulse after antenna and $25 - 200$ `MHz` band pass.

Figure 5.4: Simulated pulse of the radio EW polarized emission from a proton induced air shower in 25 `m` distance from the shower core. The primary energy of the proton is 10^{16} `eV`.
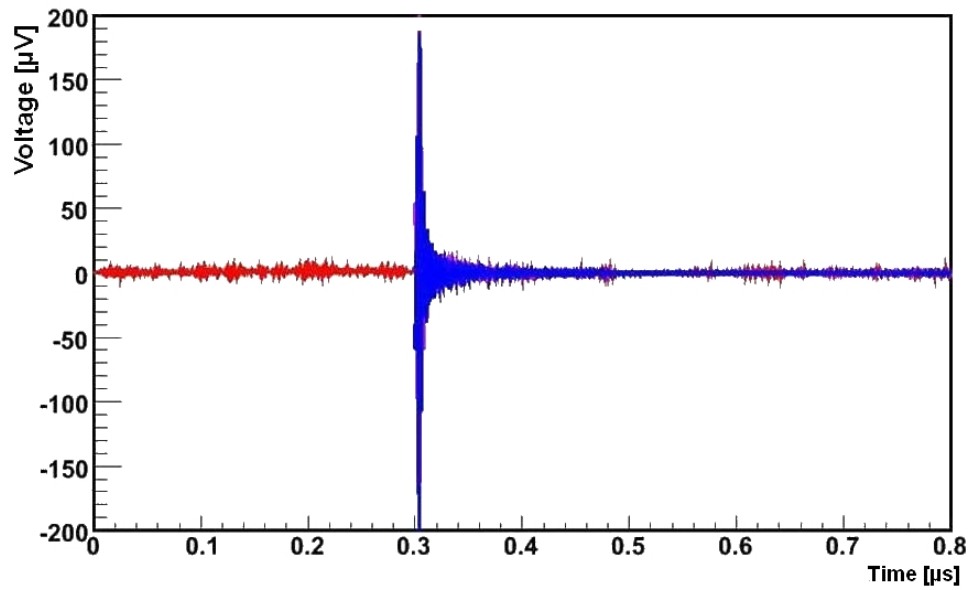
Figure 5.5: Typical background spectrum at the South Pole measured with SP1 antenna, corrected for LNA and Cable response (red line). The blue pulse is the EW polarized radio emission part of a simulated proton induced air shower with a primary energy of 10^{17} `eV`. The distance from the shower core d is 125 m with $\theta_{incl} = 45°$ and $\vartheta_{ant} = 45°$. The pulse is corrected for the antenna response, a 25 `MHz` high pass filter and a 200 `MHz` low pass filter.

propriate angle to the earth magnetic field. Nevertheless, vertical showers are measurable, too but have much lower amplitudes at lager distances to the shower core. In addition it is supposed that signals of vertical air showers can not be distinguished from RFI emitted by the MAPO building with the 2010 array (cf. Sec. 6.1). That sets the limit of the inclination angle to $< 30°$.

- The lager the **distance** to the shower core, the smaller is the predicted radio signal with REAS2 simulation. The size of this variation is in some discrepancy to calibrated measurements with LOPES [50]. Figure 2.11 is representative for most of the air showers measured with LOPES and shows systematically stronger pulses at lager distances to the shower core. Due to good agreement of the simulation with measurements at ≈ 125 m distance to the shower core, we will base our estimation of a test array on this distance.

- The optimal **frequency band** of air shower radio measurements depends on the signal to background ratio. The promising low background at low frequencies measured with SP1 and SP2 antenna lead to a detection band of $25 - 100$ MHz. The lower limit is given by the fat wire dipole antennas itself. The upper limit is due to the radio signal predictions. Signals at higher frequencies can indicate RFI.
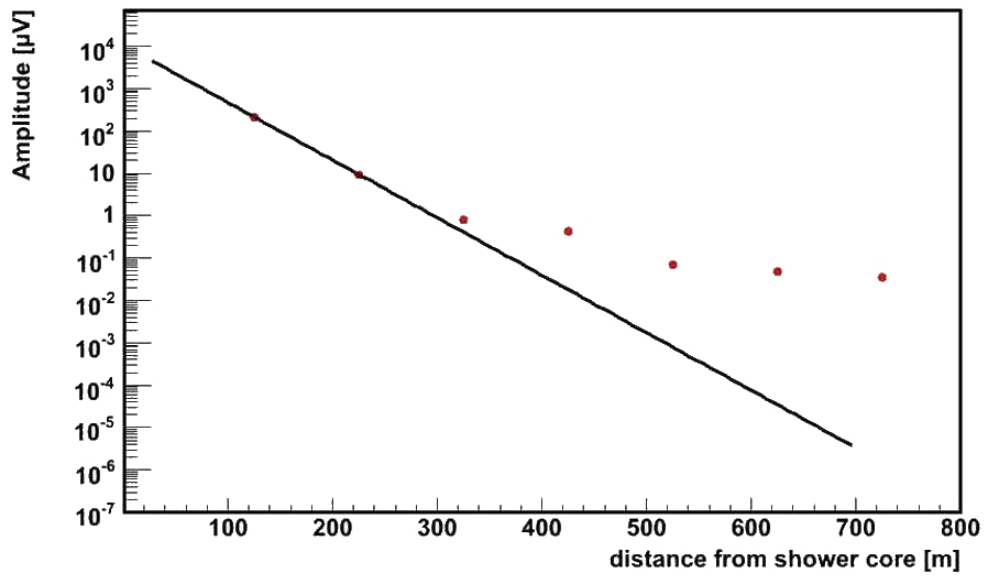
Figure 5.6: Amplitudes of a 10^{17} eV proton induced radio signal in a FWD with $25\,\texttt{MHz} - 200\,\texttt{MHz}$ bandpass at different distances from the shower core. The black line is the fit of an exponential function through the data points $< 400\,\texttt{m}$ distance, to estimate the amplitudes between $75\,\texttt{m}$ and $300\,\texttt{m}$ from the shower core.
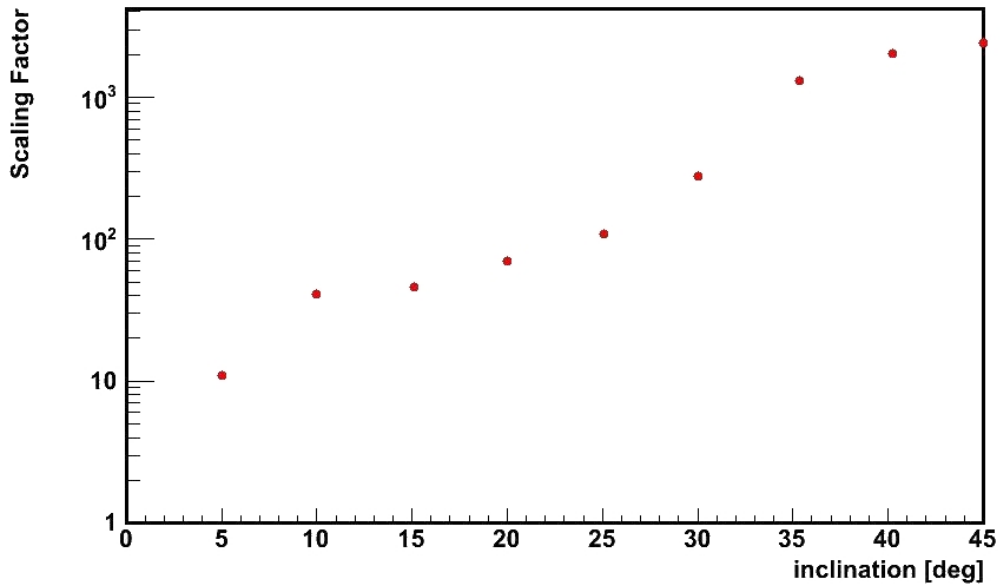
Figure 5.7: Amplitudes of proton induced radio signal in a FWD with primary energy of 10^{17} eV in 125 m distance from the shower core with increasing inclination angle and EW polarization. The air shower has an angle of $\phi = 45°$ and $\phi_{dir} = 0°$. For lager inclination angles the signal is increasing depending on the propagation length through the magnetic field, the angle due to the magnetic field and the projection on the detector plane.
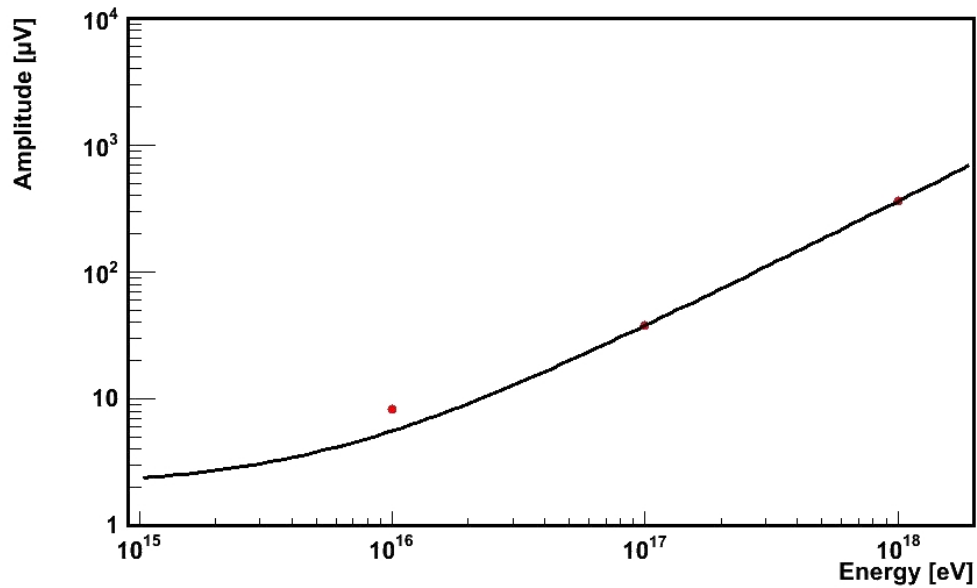
Figure 5.8: Amplitudes of proton induced radio signal in a FWD in a 25 `MHz`−200 `MHz` bandpass with primary energy of 10^{15} `eV` − 10^{17} `eV` and 45° inclination angle. The air shower has an angle of 0° to the antenna ($\phi_{dir} = \phi$). The amplitude heights are rising linearly with the primary energy if the synchrotron emission of the particle is fully coherent. The curvature of the linear fit is a scaling effect.

Chapter 6

RADIO AIR SHOWER DETECTION AT THE SOUTH POLE

6.1   2010 Test Array

The plan for the 2010 Test Array was to establish self triggers on an amplitude threshold trigger basis with analog trigger logic to measure air showers in coincidence with IceTop. It should have consisted of 6 surface antennas near the MAPO building. A schematic of the signal way of the 6 surface antennas is given in Fig. 6.2. The signal splitting for an analog trigger logic and the shorter cable length would have been the main differences to the 2009 configuration (Fig. 4.5). Three antennas could have been North-South (NS1, NS2, NS3) and 3 antennas East-West polarized (EW1, EW2, EW3). The proposed positions of the antennas are given in Fig. 6.1 relative to the MAPO building. Table 6.1 shows the suggested positions of the antennas in RICE coordinates.

For logistical reasons the 2010 Test Array was not installed in its planed position. Notwithstanding, we will describe the proposed configuration as an example for prospective Test Arrays.

6.1.1   Science case

The science case of the 2010 Test Array was twofold: The first part was to improve the background measurements of the continuous and the transient background at the South Pole in the frequency range of interest for geo-synchrotron radio air shower detection from 25 MHz to 100 MHz. The second part was the detection of radio signals

Antenna	x [m]	y [m]	z from surface [m]	cable delay (suggested) [ns]
2010EW1	-70	50	0	400
2010EW2	-60	50	0	400
2010EW3	-50	-20	0	400
2010NS1	-50	-30	0	400
2010NS2	20	70	0	400
2010NS3	30	70	0	400
SPASE	-150	-350	0	3.500
MAPO	50	-30	20	100

Table 6.1: Proposed antenna positions and cable delays to the RICE DAQ of the 2010 array antennas. The positions of the antennas would be measured by a surveyor. The x and y are calculated from the center of the MAPO building.

from air showers and transients on a self trigger basis. Offline coincidence studies with IceTop would have been possible to identify air shower radio signals.

Background measurements

The 2010 Test Array was planed to be the first self trigger surface radio system at the South Pole. Due to strong attenuation of the SP1 and SP2 antenna cables, the long term background measurements have a relatively high systematic uncertainty (cf. 4.4.3). The 2010 Test Array would have had 6 redundant antennas taking background data through the austral winter in 2010 with a significantly lower attenuation of the analog readout device due to shorter signal cables (cf. 6.1.2).

Self triggering

A self trigger logic of the 2010 Test Array would have allowed to trigger events on an amplitude threshold basis. The trigger strategy of 4 antennas with signal above a given amplitude threshold are described in Section 6.1.2. Basis of an estimation of the trigger rate with the 2010 Test Array, given in Section 6.1.3, is the assumption of Section 5 that air showers with a primary energy of 10 `PeV` will be detectable on the measured South Pole background with a Fat Wire-Dipole antenna on the Antarctic snow ground. Coincidence with IceTop would have lead to a strong evidence for air shower radio signal detection. This would have been done in offline analysis.
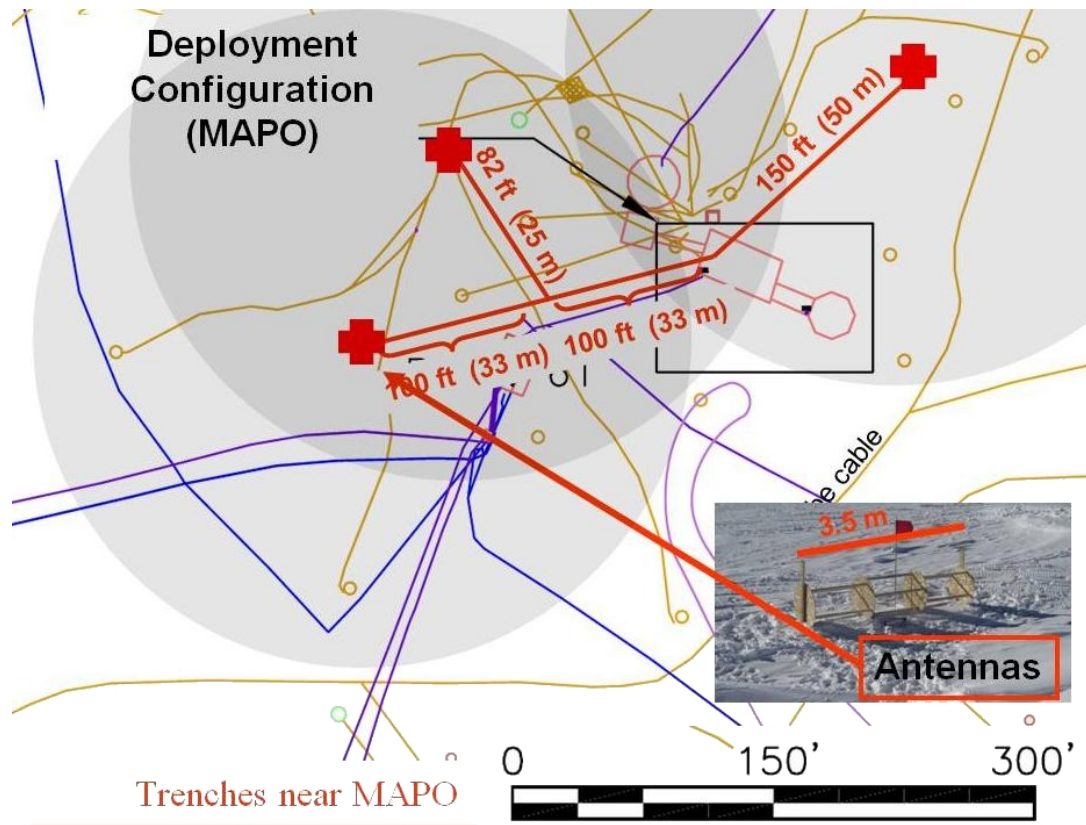
Figure 6.1: Exemplary drawing of the antenna positions of the 2010 Test Array near the MPAO building. The red lines show the cabling of the array. The gray cycles have a radius of 125 m. The overlap of two cycles indicates that four antennas are within 125 m. This is the assumed detector plain A_{detect}.
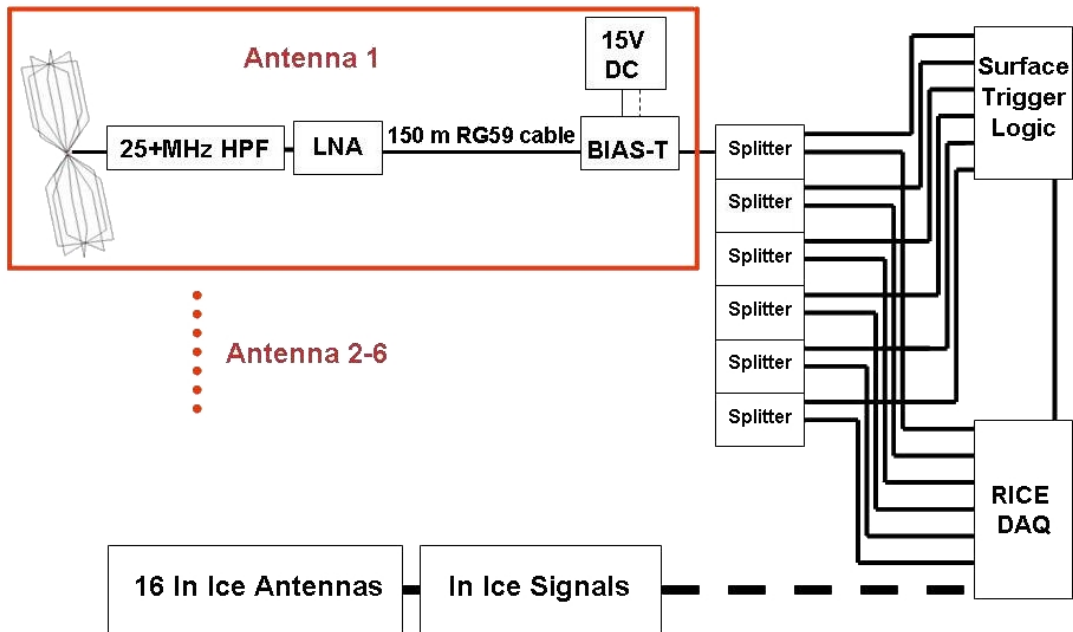
Figure 6.2: View of the signal path of the 6 surface antennas. The main difference to the 2009 configuration for each antenna is the shorter cable length and the signal splitting for the analog surface trigger logic. The trigger logic is described in more detail in Fig. 6.3.

6.1.2 Trigger strategy

In order to build a four coincidence trigger logic, we proposed to split the signal. One part of the signal would have been used to build the trigger. The other part would have been read out with a digital oscilloscope. A drawing of the trigger and signal readout device are given in Fig. 6.2 and 6.3.

Trigger threshold

Every antenna signal would have had to be discriminated to be used in the trigger logic. The threshold of a CAMAC 3412E discriminator is -15 mV, which gives us the lowest value of a possible trigger. Based on REAS2 simulations propagated trough the Fat Wire-Dipole antenna and 25 MHz high pass filter, typical RMS values of the system are 8 μV. As we wanted to set the trigger threshold to 6σ in amplitude we planed to amplify a 48 μV signal to > 15 mV. This corresponds to an amplification of 50 dB. To estimate the attenuation of the system $atten(f)_{system}$ the following calculation was done:

$$atten(f)_{system} = atten(f)_{cable} + atten(f)_{filter} + atten(f)_{bias-T} + atten(f)_{split}. \quad (6.1)$$

This formula is correct for values in dB. The attenuation of the signal cable $atten(f)_{cable}$ depends on the length of the cable and the frequency f. The length of the cable is chosen to be 150 m. This leads to a mean attenuation of 6.9 dB in the frequency band from $25 - 100$ MHz where we expect our signal. The attenuation of the 25 MHz HPF, $atten(f)_{filter}$, is 0.5 dB above 25 MHz, the signal-power splitter, $atten(f)_{bias-T}$, 0.15 dB, and the loss due to signal splitting is $atten(f)_{split} = 3$ dB. This leads to an attenuation of the system of 10.55 dB. Together with the 50 dB amplification to reach the 6σ threshold, an amplification > 60.55 dB is needed. We choose a 65 dB MITEQ LNA type AU-1014-11316-BNC. This calculates to a signal amplitude of ≈ 28 μV at the antenna for a 6σ threshold trigger. Figure 6.2 shows the signal way from surface antenna to the readout device. Chapter 5 discusses pulse heights of proton induced air showers in the Fat Wire-Dipoles used at the South Pole.

Trigger logic

After the signal would has been discriminated to a well defined NIM pulse with -800 mV amplitude and 20 ns length. Every pulse over the discriminator threshold would have started a trigger time window of 1.5 μs length. This signals would have

been fed in a multiplicity logic unit. If 4 out of the 6 channels would have received a signal over threshold in a 1.5 μs time window, the 8 μs waveforms in all digital RICE oscilloscopes would have red out and saved with RICE PC in the RICE data file format (Appendix B). The length of the trigger time window can be calculated: The maximum difference of the cable length of 200 `m` leads to a time delay of 800 `ns`. The maximum signal runtime through the air of the most distant antennas is 150 `m` or 500 `ns`. This leads to a total maximum delay of a real coincidence of 1.3 μs. The maximal sweep length of the RICE digital oscilloscopes is 8 μs at 1 `GHz` sampling speed. The dead time is estimated to be 15 s to read out one event.

There was no plan to use the MAPO roof antenna or the SPASE antenna signals to veto signals on line, but for additional information of the signal shape. It was planed to use the RICE in ice channels as a on surface software veto. As the signals would have been high pass filtered at 200 `MHz`, signals in the in ice antennas would have been a clear indicator for RFI events above the frequency band of geo-synchrotron air shower emission (cf. Fig. 2.10). A schematic of the trigger logic is given in Fig. 6.3. The time window of the trigger construction is depending on the maximum possible runtime delay of the radio signals through the surface antenna array.

VLF antenna background

As discussed in Section 4.4.3 the main background source was expected to be the very low frequency antenna (VLF). It was assumed that the main effect of the VLF antenna signals in the SPASE channels SP1 and SP2 is due to the long signal cable parallel to the VLF antenna. Thus we expected a much lower effect in the 2010 Test Array antennas. Their signal cables would have been not parallel to the VLF and none of them would have been longer than 150 `m`. To filter the VLF events, three different strategies are considered:

- A software based online timing veto.

- An efficient high pass filter.

- An offline filter algorithm.

It is well known that the VLF sends continuous signals every 15 `min` for 1 `min` starting with minute 6 of every hour. Thus it is quite easy to veto 60 `s` every 15 `min` with a software veto implemented in Labview. That would reduce the detector uptime by a factor of 6.6%.
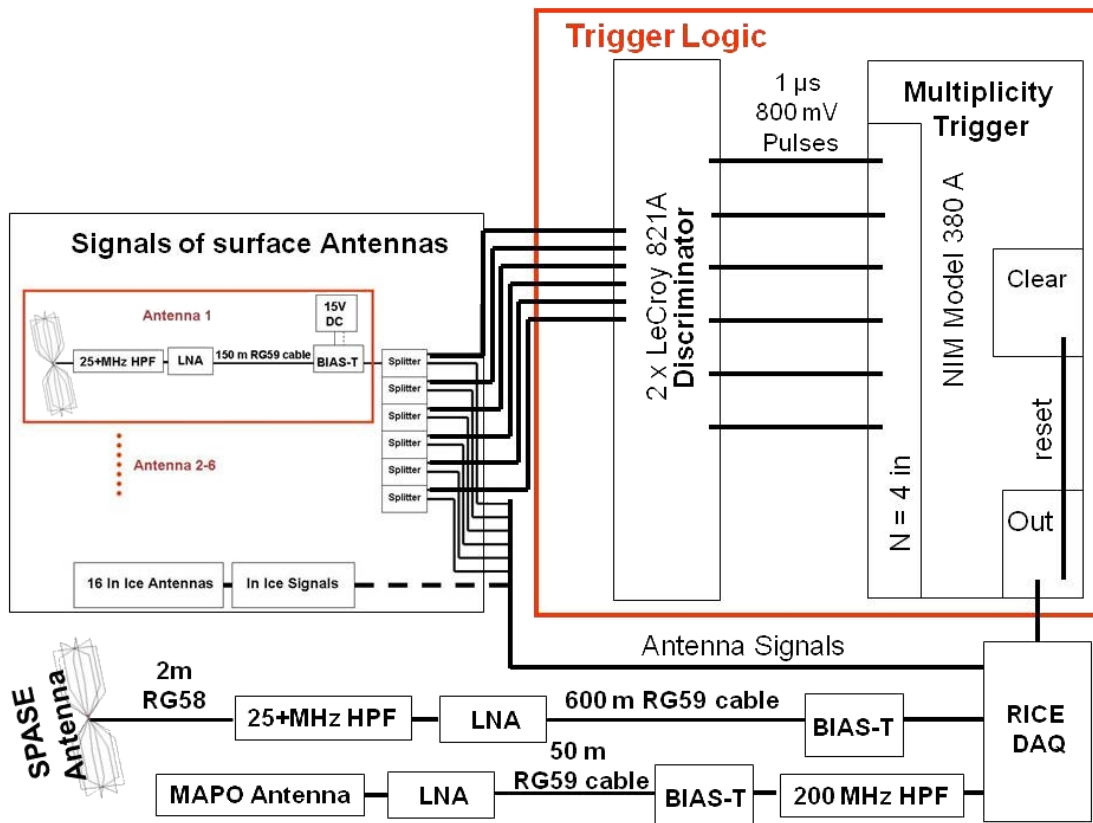
Figure 6.3: Schematic of the trigger logic for the 8 surface antennas. The signal is coming out of the splitters for each of the antennas Antenna 1-6. The antennas would have been laid on the snow surface near the MAPO building as shown in Fig 6.1. After that a 4 antenna coincidence in 1.5 μs is built. The antenna on the MAPO roof would have vetoed RFI at frequencies higher than 200 MHz. The SPASE antenna would have been red out without being part of the trigger system.

Another 25 `MHz` HPF [1] in front of the discriminator could have reduced the signal amplitude by a factor of 3000 (70 `dB`). This would have suppressed the sinus signals by a factor of 80 below the normal background for the SP1 or SP2 antennas. This would have been enough to avoid triggering, but would have led to an additional attenuation of 0.5 `dB` of the amplitude trigger threshold due to the HPF filter. Another strategy would have been to filter the events after data taking. In this case, one would have expected about 4 triggers every 15 min as a system check. This would reduce the detector uptime by 6.6%, too.

6.1.3 Estimation of the trigger rate induced by CR flux with 2010 Test Array

An estimation of the trigger rate of the 2010 Test Array depends on the effective plain A_{detect}, the CR flux Φ_{CR}, and the dead time τ_t of the detector. For a rough estimation of the trigger rate, we have to estimate these parameters. The effective plain of the experiment depends on the primary energy and the direction of the primary particle. In Section 5.2 it is discussed, which pulse height results from air showers simulated with REAS2 in our detection system. It has been shown that radio air shower signals should be detectable down to 10^{16} `eV` for very near distances like 25 `m` from the observer. But we also know from LOPES comparisons with REAS2 simulations that REAS seems to overestimate the air shower signals at low distances to the antenna [50]. To calculate whether there is a realistic chance to detect air showers, very conservative assumptions are made. Due to the simulation results and the uncertainties in comparison to experimental results, we set the energy threshold of our detector to $E_{prim} = 10^{17}$`eV` primary energy with $d_{CR} = 125$ `m` distance of the shower axis to the antenna. Figure 5.5 shows a simulated radio pulse with $E_{prim} = 10^{17}$`eV`. The lower energetic air showers with lower distances to the antenna (Fig. 5.4) are not included in the estimation. Furthermore, we choose the inclination angle to be in the range from $\theta_{incl} = 30° - 60°$ relative to the vertical as motivated in Sec. 5.3. Together with the 4 coincidence trigger strategy, the effective area of the detector is the area where 4 antennas can see a signal. For a detector geometry of three antenna places with 50 `m` distance to each other with two antennas on each place and the maximal distance of the shower axis to the antenna $d_{CR} = 125$ `m`, this leads to a detector plane of $A_{detect} \approx 35\,000$ `m`^{2}. Of course, A_{detect} depends on the real detector configuration which is not exactly known yet. Figure 6.1 shows a possible configuration. The region where two cycles overlap is A_{detect}. The required inclination angle

---

[1]The VLF sending frequency is 19.6 `kHz`. Thus the high pass filter could reject only lower frequencies. As 25 `MHz` HPF are commercial standard products, and as we filter already at 25 `MHz` we decided to use those filters again.

of $30° − 60°$ leads to an observable sky Ω_{observ} of 36.6% of the hemisphere, which is 2.29 `sr`. As the cosmic ray flux is isotrop in direction from the sky, the mean effective area A_{detect} of the experiment is sufficient to calculate the CR trigger rate. Assuming a E^{-3} CR spectrum after the knee with a flux of $\phi_0 = 6.41 ± 2 \cdot 10^{-15}$(`s sr m`^{2} `GeV`)$^{-1}$ from KASKADE (cf. Fig. 2.2) at $E_0 = 8.91 \cdot 10^6$ `GeV` the expected trigger rate of CRs of a detector with 100% efficiency is 1.5 events per day. The corresponding flux is is:

$$f_{detect} = \int\limits_{A} dA \int\limits_{0°}^{360°} d\phi \int\limits_{30°}^{60°} \cos\theta \sin\theta \; d(\theta)\phi_{int}, \tag{6.2}$$

which is:

$$f_{detect} = A_{detect} \cdot \; \Omega_{observ} \cdot \phi_{int}, \tag{6.3}$$

where the integral flux ϕ_{int} is given by:

$$\phi_{int} = \left[-1/2\phi_0 \; E_0^3 \; E^{-2} \right]_{12\,\text{GeV}}^{8\,\text{GeV}} (m^2 \; sr \; s)^{-1} = 2.27 \cdot 10^{-10} \; (m^2 \; sr \; s)^{-1}. \tag{6.4}$$

With the typical RICE trigger rate of 1/`min` and the associated dead time of 15 `s` the CR trigger rate is reduced by 25%. Together with the dead time due to the VLF discussed in Section 6.1.2 the total uptime of RICE can be estimated to be 70% which reduces the rate to 1 event per day for CR primary energy $E_{prim} > 10^{17}$ `GeV`. Figure 6.4 shows the strong dependency of the detectable flux as a funktion of the energy threshold.

The number of coincidences with IceTop would have been roughly the same, as the effective area of IceTop is 100% above 10 `PeV` even for inclination angles up to 46° [41] and the 2010 Test Array would have been surrounded by IceTop. For highly inclined showers above 46°, the reconstruction of the direction has high uncertainties. Above a primary energy of 10 `PeV` the detection efficiency for air showers of IceTop is in the oder of 100% [42]. Figure 6.5 shows the effective area of IceTop for different zenith bins from MC simulations.

6.1.4 Self Trigger Trial 2010

Logistical problems with Raytheon Polar Service lead to a limited implementation of the 2010 test array. It was not possible to deploy antennas in large distance to the MAPO building.
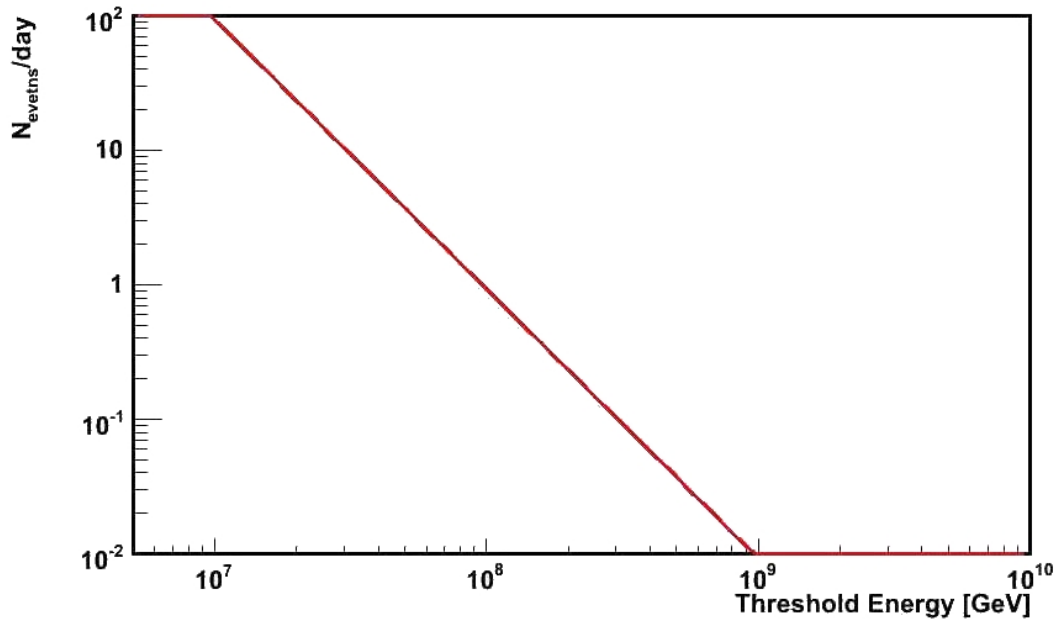
Figure 6.4: Number of detectable events/day with the 2010 Test Array versus the trigger threshold in energy of the primary particle. The detector live time is estimated to be 70% and four antennas have to be in 125 m distance from the shower axis.
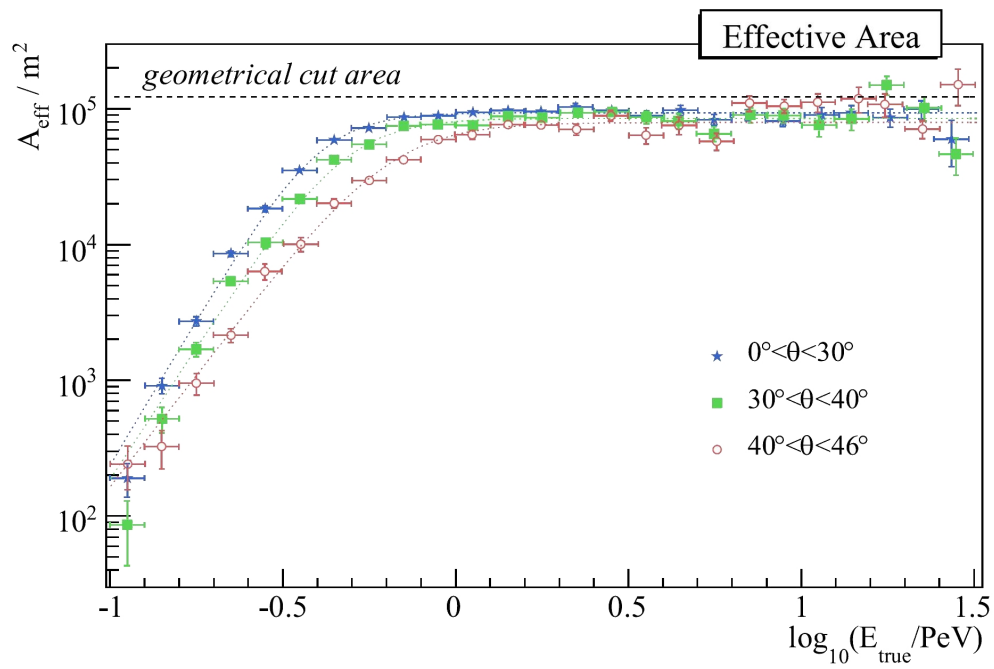
Figure 6.5: Reconstruction threshold function in terms of effective area for three zenith bins, studied with proton shower simulations of IceTop [41]. As the 2010 Test Array is surrounded by IceTop, the number of coincidences can assumed to be 100%.

Antenna	discriminator Value [mV]	cable length [m]	cable delay [ns]
FWD 1 NS	-1020 ±1	71.2 ±0.3	292 ±2
FWD 2 EW	-880 ±1	77.7 ±0.3	317 ±2
roof 1 xyz	-480 ±1	32.0 ±0.3	139 ±2
roof 2 z	-1000 ±1	36.6 ±0.3	156 ±2

Table 6.2: Discriminator threshold of the four surface antennas and the cable delays. The discriminator fires for signals with negative voltage under the threshold. The delays are calculated from delay measurements. For the roof antenna Belden RG8 M8214 cable was used. RG59 Belden 1829B cable connects the FWD with the DAQ.

Nevertheless, a 2010 self trigger tests with FWD antennas at the MAPO building were established with the RICE DAQ to estimate the trigger rate of an amplitude trigger strategy. Figure 6.6 shows the signal line of the received signals to the RICE oscilloscopes. It triggers on signals with amplitudes $< -480\,\mathrm{mV}$ to $< -1020\,\mathrm{mV}$ at the discriminators. Table 6.2 shows the discriminator thresholds. Due to amplification of the 65 dB LNAs and the attenuation of the 50 m RG59 cable, the 25 MHz high pass and the 200 MHz low pass filters, the bias-T and the signal splitting, the predicted amplitude of a detectable signal has to exceed $\approx 0.7\,\mathrm{mV}$ signal strength in the FWD antennas. For the roof antennas the signal amplitude in the antennas are 0.7 mV for the "roof 1" and 0.8 mV for the "roof 2" antenna. Table 6.3 lists the attenuation and amplification of the different components at 50 MHz for the different antenna channels. Figure 6.7 shows the schematic of the trigger logic implemented into RICE. The new event type is called "ext2". Figure 6.8 shows the positions of the antennas on the MAPO roof and on the snow ground near the building. The estimated positions are tabulated in Table 6.4. The Figures 6.9 and 6.10 show the antennas at the South Pole in 2010.

Due to shadowing effect of the MAPO building on the surface antennas one can not expect to see radio air shower signals from the direction of the MAPO. It is suspected that signals from other directions are influenced by reflection effects at the building, which complicates the interpretation of possible radio detections from air showers. Nevertheless it is expected to measure trigger rates of short pulsed RFI during the Antarctic winter. This will help to estimate the efficiency of a future radio air shower test array. Based on detailed estimation on the detectable CR flux with a 2010 test array (Section 6.1) the 2010 array is estimated to have a ten times lower detection efficiency in the order of 1 event/week.

Antenna	atten cable [dB]	atten filter [dB]	ampl LNA [dB]
FWD 1 NS	3.3 ± 0.2	0.2 ± 0.05	64.7 ± 0.75
FWD 2 EW	3.6 ± 0.2	0.2 ± 0.05	64.7 ± 0.75
roof 1 xyz	1.2 ± 0.1	0.2 ± 0.05	64.7 ± 0.75
roof 2 z	1.3 ± 0.1	0.15 ± 0.05	39.1 ± 0.6

Table 6.3: Attenuation of the system components in dB at 50 MHz. The total error on the amplitudes is < 1 dB.
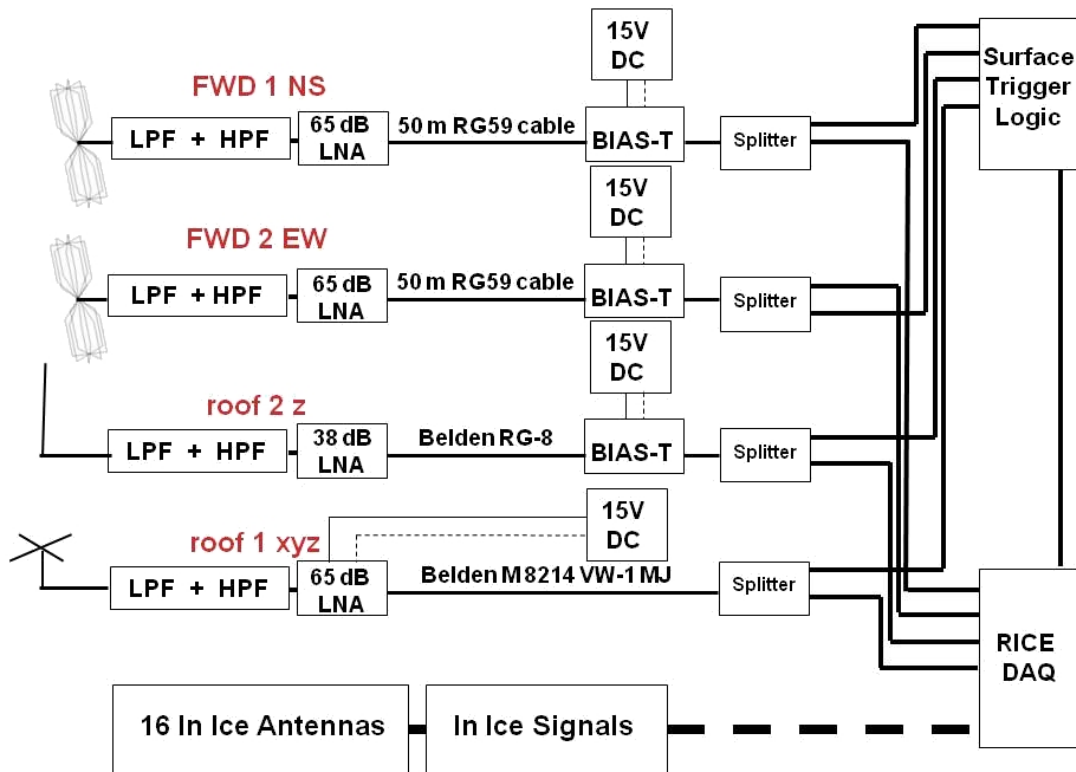
Figure 6.6: Signal path of the 4 antennas deployed in 2010 near and on top of the MAPO building. The "roof 1 xyz" is a four half arm dipole antenna and the "roof 2 z" antenna is a half-arm dipole, both on the MAPO roof. All channels are 200 MHz low pass and 25 MHz high pass filtered. The roof antennas use different cables and "roof 2 z" has a 38 dB LNA.
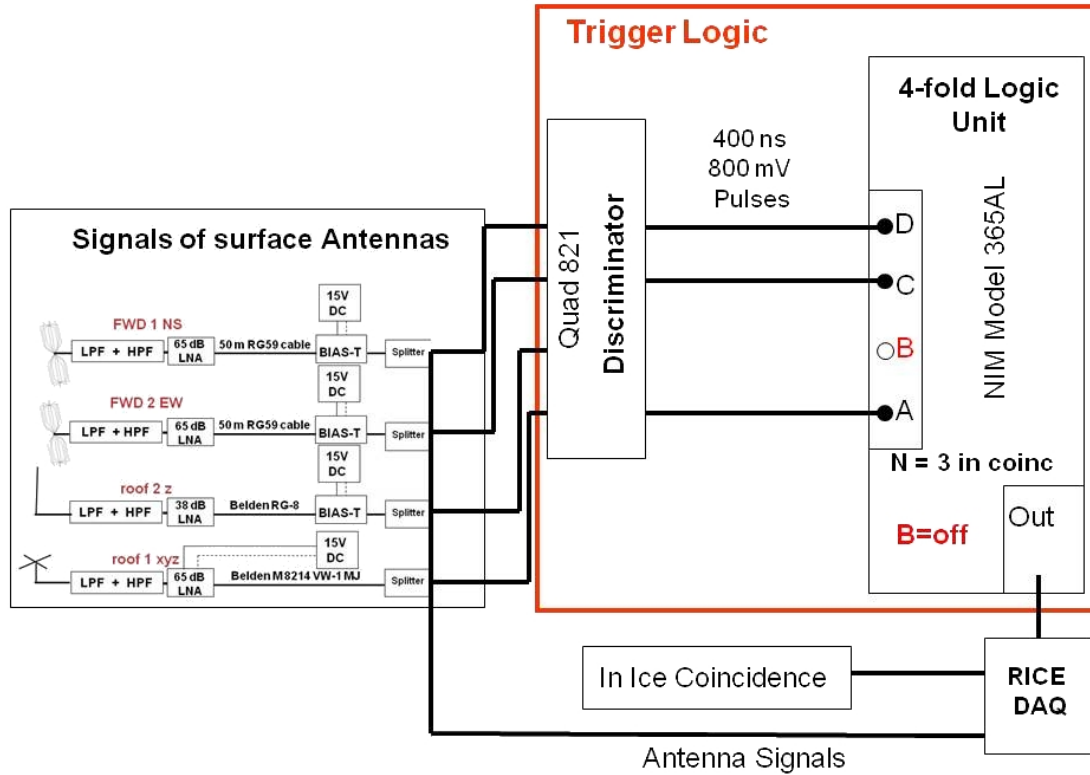
Figure 6.7: Trigger logic of the 4 surface antennas deployed in 2010 near and on top of the MAPO building. "FWD1 NS" and "FWD2 EW" and the "roof 1 xyz" are part of a three out of three coincidence logic. The "roof 2 z" antenna is not part of the trigger. The discriminator thresholds are summarized in Table 6.2.

Antenna	x[m]	y[m]	z[m]
FWD 1 NS	30 ±0.5	-9 ±0.5	0.5 ±0.5
FWD 2 EW	14.7 ±0.5	-16.8 ±0.5	0.5 ±0.5
roof 1 xyz	47.0 ±0.5	-28.0 ±0.5	18 ±0.5
roof 2 z	29.5 ±0.5	36.6 ±0.3	18 ±0.5

Table 6.4: Positions of the antennas deployed in 2010 in RICE coordinates.
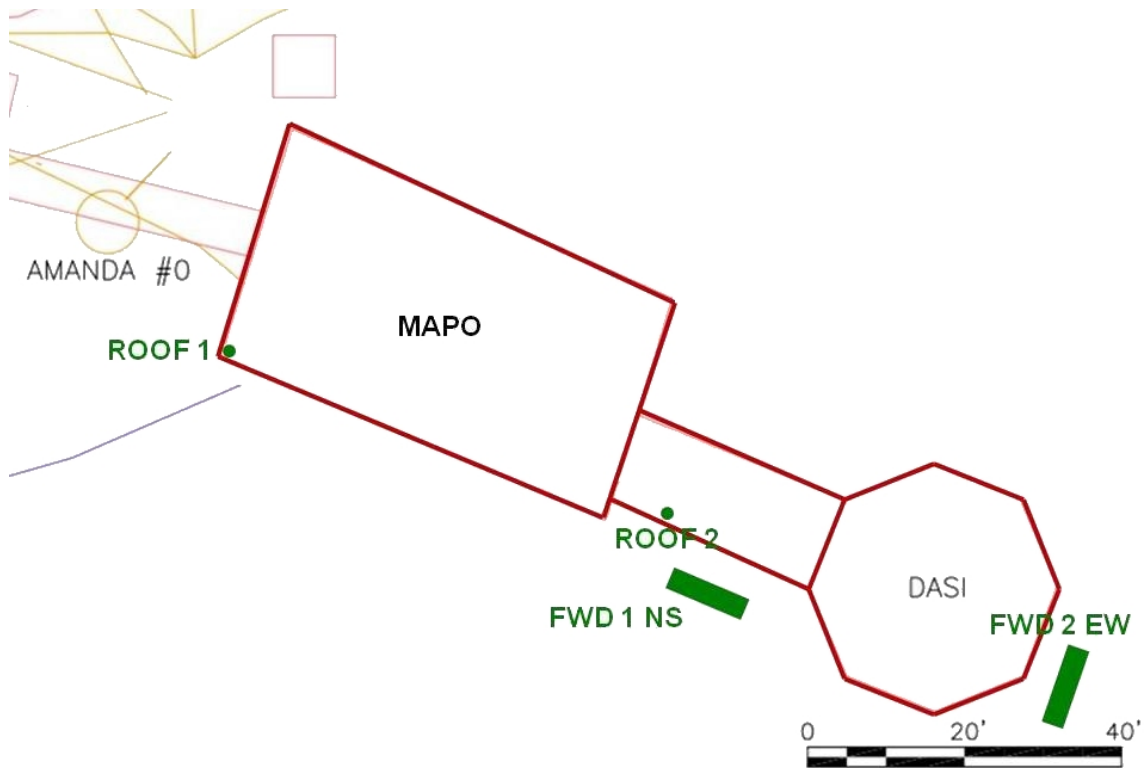
Figure 6.8: Schematic of the antenna positions in 2010. There are two antennas on the roof and two antennas on the snow ground directly in front of the MAPO building. Where "roof 1" is a crossed four half arm dipole antenna, "roof 2" is a half arm dipole in z direction and "FWD1 NS" and "FWD2 EW" are fat wire-dipoles. "FWD1 NS" and "FWD2 EW" are East-West and North-South polarized.
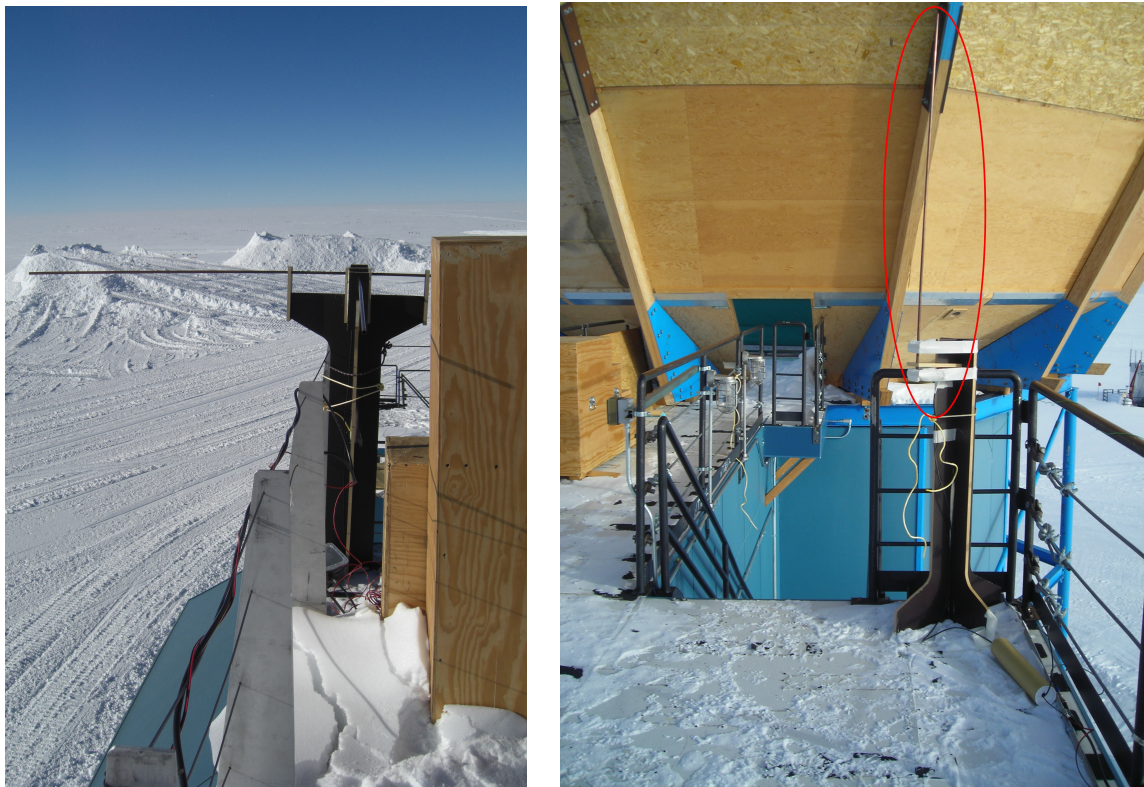
(a) The four half arm dipole antenna deployed at the front left corner of the MAPO roof called "roof 1 xyz".

(b) The half arm dipole in z direction deployed on the front right part of the MAPO roof called "roof 2 z".

Figure 6.9: The antennas deployed 2010 on the roof of the MAPO building.
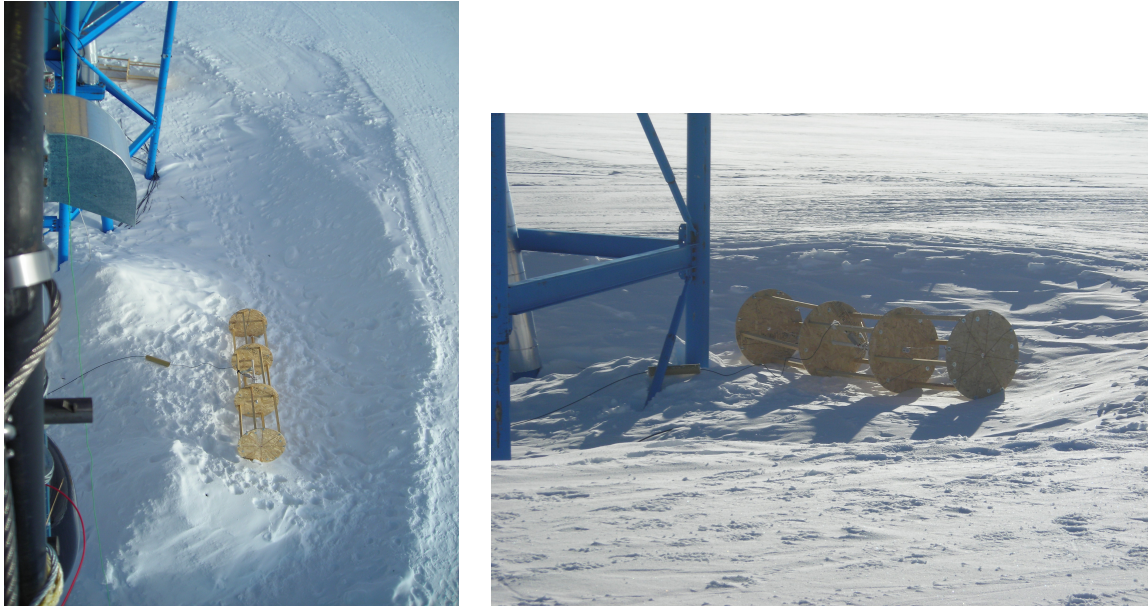
(a) The first Fat Wire-Dipole is lying on the snow ground in North-South direction to the Earths' magnetic field. It is called "FWD 1 NS".

(b) The second Fat Wire-Dipole is lying on the snow ground in East-West direction to the Earths' magnetic field. It is called "FWD 2 EW".

Figure 6.10: The antennas deployed 2010 on the ground near the MAPO building.

6.2 A Large Air Shower Array

The IceCube observatory is a unique facility not only to detect neutrino induced leptons, but also a great facility for air shower detection. Where the component IceTop is a classical surface detector, the in ice component IceCube is a unique muon detector to detect the hard component of air showers. This muonic component of air showers is a strong background source for high energy neutrino detection. Both, the potential for charged cosmic ray physics and cosmic neutrino detection of a large radio air shower detection will be described.

6.2.1 Motivations

A way to motivate the idea to construct a large radio air shower array at the South Pole is to look at the first EHE neutrino searches with IceCube-9 [1]. First analysis with this data have used the strategy of cutting the integrated number of photo electrons (NPE) deposited in the digital optical modules (DOMs) of IceCube. This reduces the muonic background of cosmic ray induced air showers in the signal of

---

[1]IceCube-9 is the 9 string configuration of the year 2006

the detector [31].

$$\text{NPE} \geq \begin{cases} 4.6 \cdot 10^5 & \text{if } \cos \theta \geq 0.1 \\ 1 \cdot 10^5 & \text{otherwise.} \end{cases} \tag{6.5}$$

This leads to a high reduction of the efficiency for EHE neutrino detection in the energy range of $10^5 < \text{E} < 10^{11}$ GeV. Another strategy, would be to cut in the inclina-
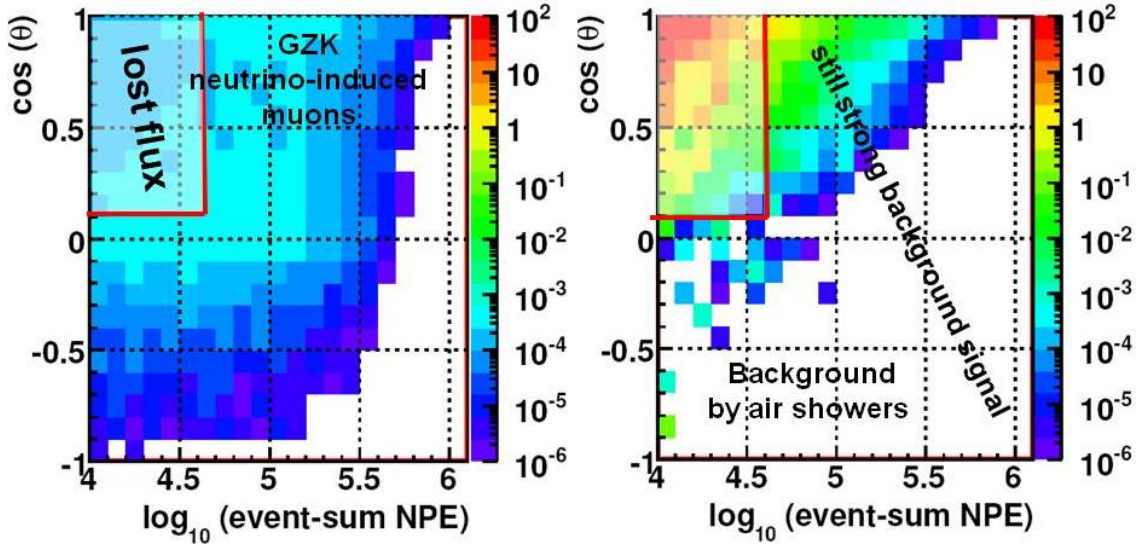
Figure 6.11: Integrated number of photoelectrons (NPE) against the inclination angle θ for a GZK neutrino-induced muon flux prediction in the energy region $10^5 < \text{E} < 10^{11}$GeV (left) and of MC studies of the cosmic ray background (right). The color code represents the number of events. The red line indicates the lost GZK neutrino flux by cutting in the NPE to reduce the air shower background [31].

tion angle of the incoming muons. Most of the air shower background is down going, while a sizable part of the GZK neutrino flux is up going with $0.1 \geq \cos \theta \geq -0.9$. Eliminating the signals with $\cos \theta \geq 0.1$ is a powerful way to reduce the air shower background, but also leads to a reduction of the detectable GZK neutrino flux (cf. Fig. 6.11).

More sophisticated analysis on IceCube-22[2] data will use an even higher cut region (cf. Fig. 6.12). The IceCube-22 cut region excludes more than 85% of the total GZK signal. A cut ending at $\cos \theta \geq 0.25$ (cf. the red line in Fig. 6.12) would already decrease the excludet flux to $< 65\%$. In terms of detectable GZK neutrino flux this would increase the detectable flux of IceCube-80[3] for optimistic GZK-models [35] from 0.50 `events/year` to 1.15 `events/year` by a factor of 2.3 or up

---

[2]IceCube22 is the 22 string configuration of the year 2007
[3]IceCube-80 is the 80 string configuration of the year 2010

to 2.14 `events/year` for the model from [73]. The total flux was estimated from IceCube-22 simulations by scaling with the IceCube80 detector volume. It was scaled to 365 days of IceCube-80 data. Of course this is somehow unrealistic, as we assume a 100% veto efficiency for this calculation. Predicting a 99% veto efficiency, the cut region would be changed to lower NPE values. Possible cut limits due to 99% veto efficiency are plotted with green lines in Fig. 6.12. The region with the highest GZK flux is within the 99% efficiency cut region. Thus the new cut value due to 99% air shower veto efficiency would still increase the number of detecable UHE kosmogenic neutrino events by a factor of 2.

A combination of both strategies to distinguish air shower induced muon bundles and neutrino induced high energy muons, is to detect and veto air showers with surface detectors with a large number of photoelectrons in IceCube and inclination angle $\cos\theta \geq 0.25$. The angular reconstruction of muon bundles in IceCube will be improved by the combination of IceTop and the Large Air Shower Array and, as well, lead to a long lever arm for the angular reconstruction of air showers and their induced muon bundles.

IceTop located on top of IceCube is a powerful instrument to veto nearly vertical air showers hitting IceCube but the limited directional acceptance of IceTop limits the veto to low inclination angles. As Fig. 6.12 shows, IceTop is not able to veto a large amount of the air shower background, as its angular acceptance is higher than $\cos\theta \geq 0.9$. To get an air shower veto detector for IceCube it is important to be able to veto air shower signals over a large part of the hemisphere in coincidence with IceCube. This veto detector system would be able to veto almost every air shower induced muon bundle instead of cutting both, GZK signals and air shower background with inclination angles above the surface.

Our idea is to construct a large area radio air shower detector, using the geo-synchrotron effect for detection, located on the surface several kilometers around IceCube. This detector could be able to flag the signals coming from air shower muon bundles by detecting the air showers in coincidence with IceCube. It would be possible to veto almost horizontal air showers (Fig. 6.12) and thus reduce the muonic background in IceCube over the full hemisphere.

Compared to currently used cuts for UHE analysis in IceCube, the detectable neutrino flux with IceCube would be increased for about a factor of 2.3 for a 100% efficient veto detector. For a lower veto efficinecy the detectable neutrino flux would decrease as one would have to cut away background again. The total number of detectable cosmogenic neutrinos would stand low, in the region of 1 `event/year`, as the total detector volume of IceCube is not increased with this technique.

Figure 6.13 is a schematic overview of how a surface radio array at the South Pole
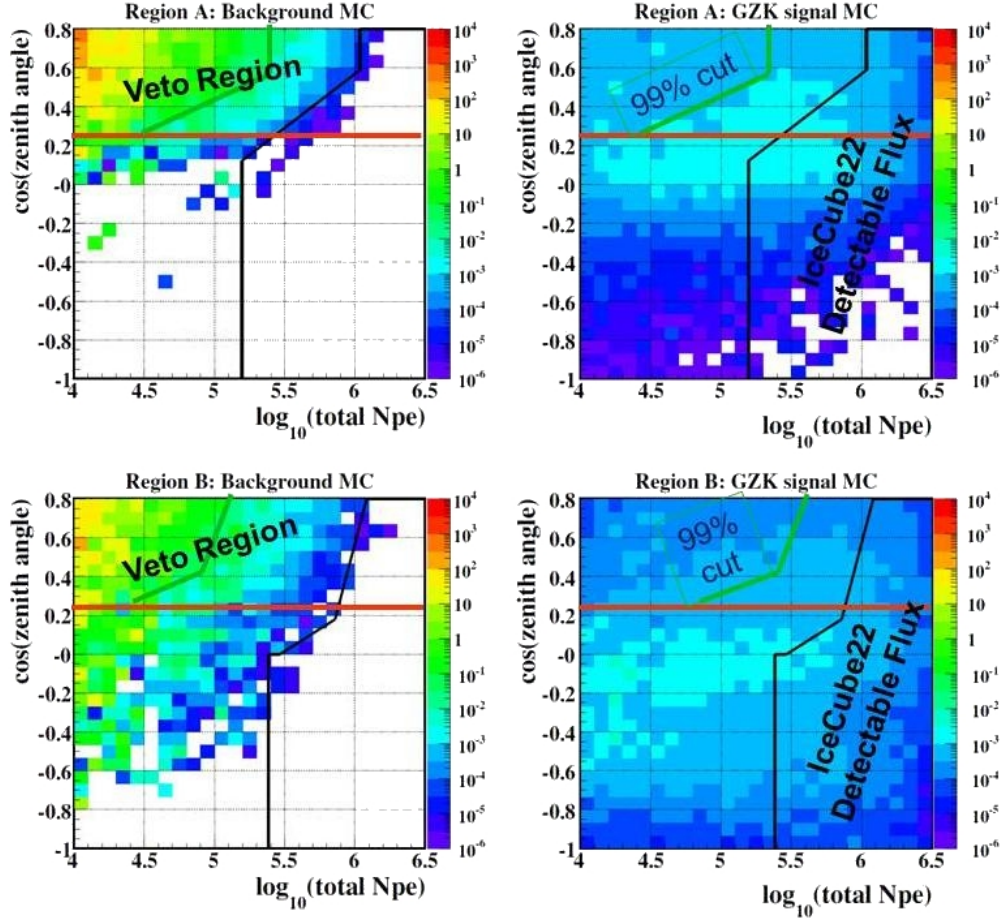
Figure 6.12: Integrated number of photo electrons (NPE) versus the inclination angle θ for a GZK neutrino-induced muon flux prediction in the energy region $10^{7.5} < E < 10^{10.6}$GeV (right) and of MC studies of the cosmic ray background (left). The color code represents the number of events. The black line indicates the lost GZK neutrino flux by cutting in the NPE to reduce the air shower background [31]. Region A and region B are different detector regions due to different optical properties. The red line indicates the region where a large radio air shower detector could veto on air showers. For a 100% efficient veto detector this region would require no cleaning cuts. A 99% efficient veto detector could lower the cut region to a limit marked with the green line. This would help to include the highest flux regions to the detectable flux region for detection region A.

around IceCube could look like. The runway near the South Pole station limits the detector plane in this scenario due to the buildings on the other side of the runway.
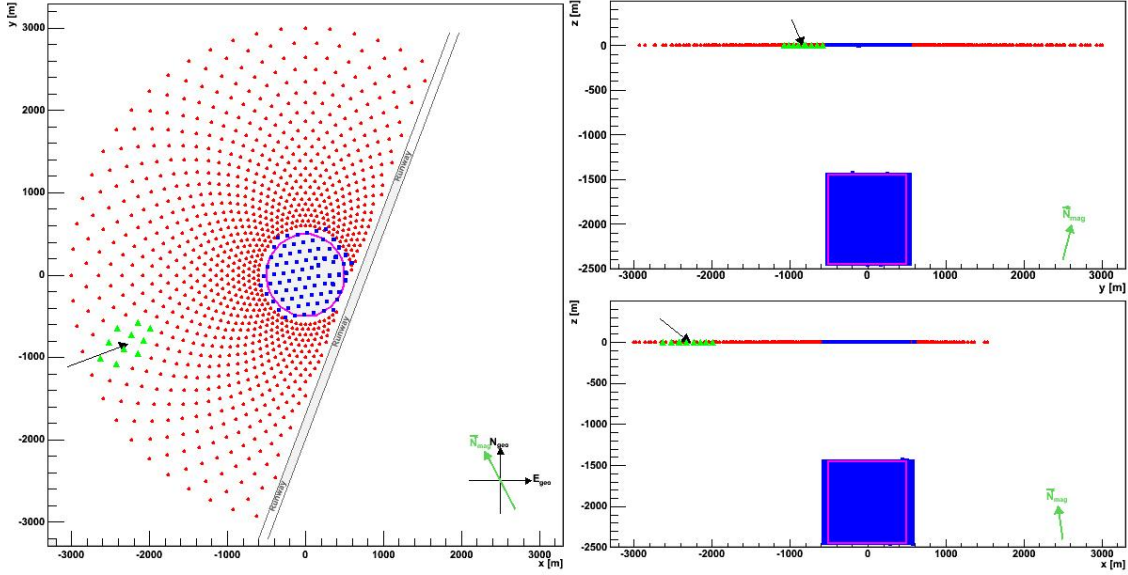
Figure 6.13: Schematic view of a large antenna array at the South Pole. Where the blue dots indicate the IceTop tank positions, the red dots are antenna positions in a half circle around IceCube. The runway near the South Pole Station limits the detector plane in this scenario. The green triangles are the radio footprint of an example 1 `PeV` air shower. The green arrow indicates the direction of the magnetic field. The blue rectangular is the IceCube detector area, where the magenta line limits the region where air showers have to point to, to get detected by IceCube [10].

6.2.2 Technical strategies

In this section an exemplary strategy to connect surface radio data with IceCube information will be discussed. The main part of the strategy is to use the known information of IceCube to reduce the amount of data of the surface radio array.

To be able to detect radio signal from air showers down to low energies a cross correlation strategy like at the LOPES experiment could be used [26]. The principle of a cross correlation beam forming, or cc-beam forming, is to multiply the data from each pair of antennas, averaging the values and square root the result while preserving the sign:

$$cc(t) = \pm\sqrt{\left|\frac{1}{N_{Pairs}}\sum_{i=1}^{N-1}\sum_{j>i}^{N}s_i(t)s_j(t)\right|}, \qquad (6.6)$$

where N_{Pairs} is the number of unique pairs of antennas ($N_{Pairs} = \frac{(N-1)N}{2}$ with N is the total number of antennas). The negative sign is taken, if the sum has a negative sign before taking the absolute values and vise versa for the positive. The advantage of the cc-beam forming is its sensitivity to the difference between coherent and incoherent pulses. Thus it is an adequate method to filter small signals out of random (e.g. thermal) noise. One of the critical points is the data handling with a huge amount of data of a large number of antennas.

To reduce the data one has to cross correlate, by using additional information from IceCube. Fastly available IceCube information could help to get a first guess of the signal region and thus reduce the data stream which has to get red out. Apart from a classical threshold trigger system to trigger on high energetic air shower pulses, clusters of antenna signals could be buffered locally. Supposing that IceCube has a signal from this direction, the clusters could send their signal to a central storage place. The total length of a signal a local cluster of antennas has to buffer is depending on the dimensions of the array and the speed of a trigger decision. Due to the dimension of the array of several `km` a time buffer in the region of `ms` (200 μ`s` for an array with 6 `km` diameter) is needed. In addition, the trigger decision speed of IceCube is in the region of one second. Three different trigger strategies could be used:

- A standalone radio air shower self trigger. If the pulsed RFI sources are low enough, the strategy can be a voltage amplitude threshold trigger described in Section 6.1.3, based on logic decisions on discriminated signals of one local cluster. Typical trigger rates could be in the region of `Hz`. The energy threshold could go down to several PeV like estimated in Chapter 5.

- IceTop trigger based on shower front reconstruction. A fast shower front reconstruction of events observed by IceTop is available in `ms` from the IceCube DAQ. The energy threshold can be > 100 `TeV` depending on the energy threshold of IceTop. Typical trigger rates would be 10 `Hz`.

- IceCube trigger based on fast direction reconstruction methods. IceCube currently uses high multiplicity filter to store events seen in a large number of DOMs. Thereby a fast reconstruction of the direction of the event is made, based on the timing of the DOM events. This direction could be used to store the right data samples. This trigger could be the basis of the veto strategy and would have an energy threshold of about 100 `TeV` and a 10 `Hz` rate, where the latency is in the region of seconds. This requires a large buffer time in the local clusters.

6.2.3 Simulation studies

A simulation effort for a large surface radio array at the South Pole in interaction with IceCube has been started with the following academic ansatz.

Geometry

Due to the intention to veto air shower signals in IceCube, the geometry of a large air shower array is proposed to be around the IceCube observatory. Caused by the South Pole infrastructure the surface radio array is limited by the runway. This is included in the array geometry. Figure 6.13 shows a possible detector plane together with the IceCube footprint in blue. If the shower axis crosses the magenta cylinder, the air shower has to be vetoed. In this scenario the distance of the rings of antennas to each other increases with increasing distance from IceCube with:

$$r_{ring} = tan(\theta_{min} - n \cdot d\theta) * depth_{IceCube},$$ (6.7)

where n is the ring number, as the radio signal of air showers is increasing $\propto \mathbf{V} \times \mathbf{B}$ and air showers with higher distance to IceCube have to be more inclined to hit the IceCube detector and thus the propagation direction is more orthogonal to the magnetic field. The minimal radius is defined with θ_{min} to be $600\ m$ where $d\theta$ is dependent on the maximal allowed radius and the number of rings. The number of antennas per ring is chosen to be constant. These parameters are variable and should be part of a detailed simulation approach.

Radio pulse parametrization

Currently there is no adequate method for mass production of radio signals from air showers. Where the REAS2 simulation is very CPU consuming, the REAS1 simulation is known to be not realistic for us due to the parametrization of REAS1 on the properties of the LOPES experiment. A first strategy to parametrize air shower radio pulses is a mixture of informations known from REAS2 and a parametrization from the REAS1 radio extensive air shower simulation. After adding a background the pulse spectrum is produced. From [28] we get the REAS1 parametrization to be:

$$
\begin{aligned}
E(r, \phi_0, \nu, E_p, X_{max}) \quad = \quad & f \times E_\theta(E_p/10^{17}\texttt{eV})^{0.96} \\
\times \quad & exp[-(200\,m(\alpha(X_{maxPole}) - 1) + l(r, \phi_0))/(\alpha(X_{max}) \cdot l_\theta)] \\
\times \quad & exp[-(\nu/\texttt{MHz} - 10)/(47.96 \cdot exp(-(r, \phi_0)/b_\theta))].
\end{aligned}
$$ (6.8)

We ignore the last term with the spectral dependence ν and replace that with a Landau function fitted to the pulse in the time domain from REAS2 simulations.
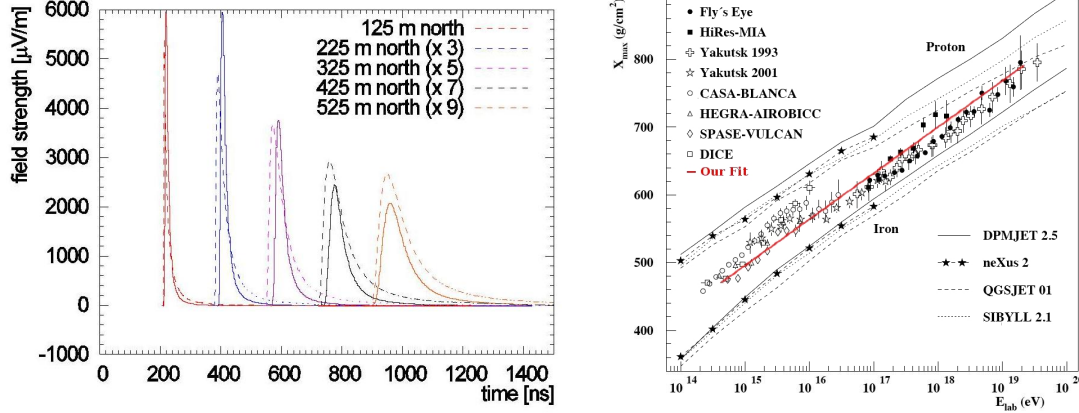
(a) Landau fit (solid line) of the REAS2 pulse prediction of a 1 PeV proton induced vertical shower at 0 altitude.

(b) Parametrization of the X_{max} of cosmic rays based on experimental data. The red line indicates the fit through the data [41].

Figure 6.14: Where the pulse shape is parametrized with a Landau fit on REAS2 simulations, the $X_{max}(E)$ for air showers is got from experimental results.

A comparison of the Landau fits with REAS2 simulations is shown in Fig. 6.14a. For vertical air showers with 10^{15} eV primary energy this prediction is in acceptable agreement.

The parameter f is used to correct for the amplitudes. E_θ, l_θ and b_θ are parametrized with data from [28] based on calibrated LOPES measurements, where θ is the inclination angle of the air shower:

$$E_\theta = 0.562 \cdot e^{(3.09 \times cos(\theta))} \left[\mu V\ m^{-1}\ MHz^{-1}\right] \tag{6.9}$$

$$l_\theta = 125/(cos(\theta)^3)\ [m] \tag{6.10}$$

$$b_\theta = 200/(cos(\theta)^{1.53})\ [m]. \tag{6.11}$$

In addition, we have to correct for the observers height at the South Pole. This is assumed to be the same as having the observer nearer to the shower maximum. Therefore, we add the difference in atmospheric depth at sea level ($X_{maxSea} = 1023$ g/cm^2) to that at South Pole ($X_{maxPole} = 680$ g/cm^2) to the depth of the shower.

$$X_{maxSea} - X_{maxPole} = (343\ g/cm^2). \tag{6.12}$$

This leads for α_{XMax} from [28] to:

$$\alpha(X_{MaxPole}) = 1.00636 \cdot ((X_{max} + 343g/cm^{2)}/631g/cm^2)^{-1.50519} \tag{6.13}$$

These pulses can be superimposed with background. The first measurements for the background at the South Pole have shown, the background is $< 10~\mu V/m$ (Sec. 4.4.3). Taking the antenna to be an ideal isotropic radiator and assuming an ideal 60dB amplifier and a `12Bit` ADC the pulses in the time domain depend on on r, ϕ_0, ν, E_p if we parametrize X_{max} like for REAS1 simulation:

$$X_{max} = -523.8~\textrm{gcm}^{-2} + 68.0 \cdot log10(E/\textrm{eV})~\textrm{gcm}^{-2}. \tag{6.14}$$

Figure 6.14b shows the chosen parametrization based on different experimental results. The result is radio pulses, together with background for each antenna position in the time domain. Figure 6.15 shows a pulse of a 10 `PeV` shower together with the cc-beam of the ten antennas closest to the shower core in red.

Figure 6.16 shows the cc-Beam of the 10 antennas closest to the shower axis of
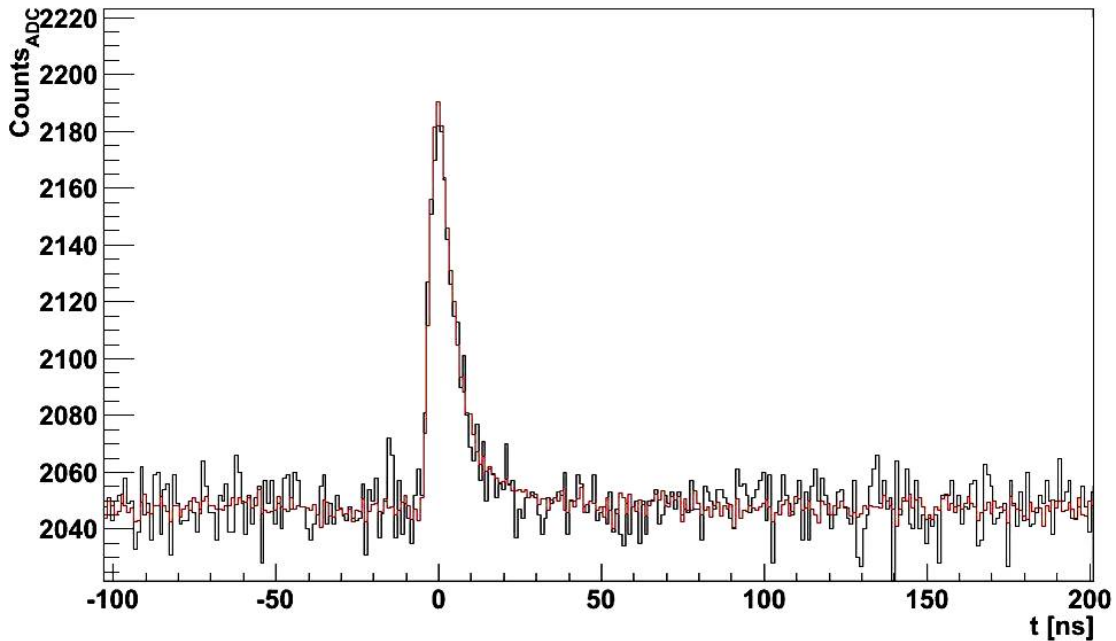
Figure 6.15: The black line is a 10 `PeV` air shower pulse coming from the geomagnetic East with 56° inclination angle together with 10 $\mu V/m$ Gaussian background. The red line is the cc-beam of the 10 antennas closest to the shower axis.

an air shower with 1 `PeV` primary energy together with the impact point on the detector. The cc-Beam has a signal amplitude over background RMS of 6 and shows 1 `PeV` primary energy air showers should be detectable.
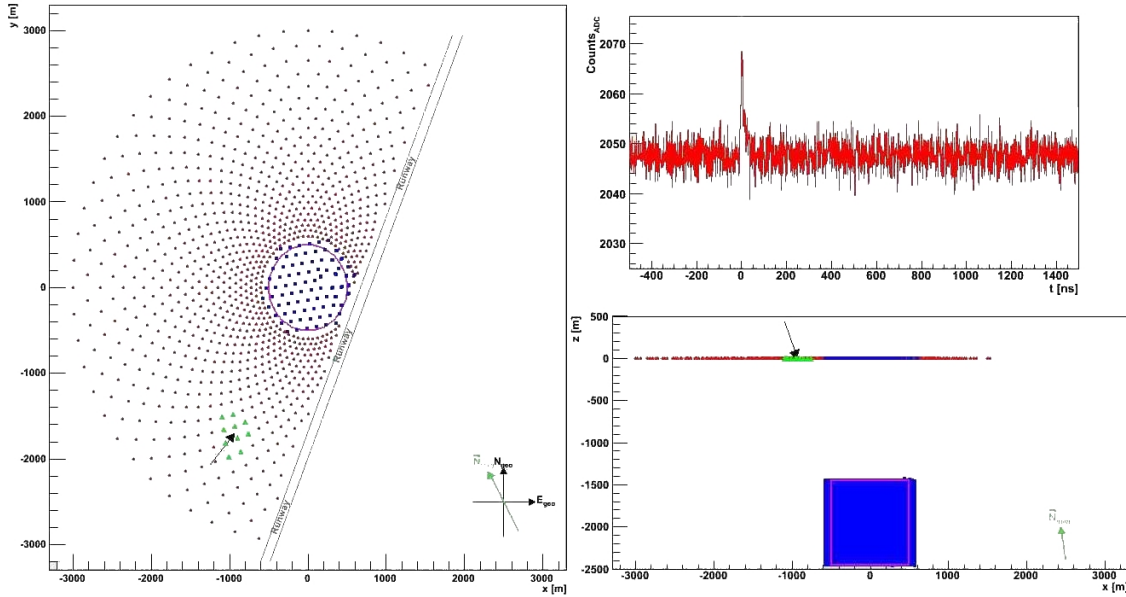
Figure 6.16: The green triangles are the 10 antenna positions of a 1 `PeV` primary energy air shower pulse nearest to the shower axis coming from the geomagnetic West. The red pulse on the upper right is the CC-Beam of the 10 antennas closest to the shower axis together with 10 μ`V`/`m` Gaussian background.

6.2.4   Discussion

A meaningful simulation of a large radio air shower array needs some improvements which will be discussed here. In addition one should mention the weak points of the veto detection idea.

Significance

To efficiently veto air showers for IceCube UHE neutrino detection, the detector efficiency of the radio air shower array has to be very high. A significant improvement of the signal to noise ratio still requires a remarkable number of UHE neutrinos itself. Actual predictions of the cosmogenic neutrino flux predict a rather small flux for the IceCube detector of a few per year [73],[35]. This weakens the arguments on the veto detection.

However, there are other arguments for a large radio air shower detector in the direct vicinity of IceCube like unique chances to detect the composition of air showers and the chance to distinguish between more electromagnetic and air showers with larger muonic component. This could open a new window for for cosmic photon detection in the $1 - 10$`PeV` regime. Of course, this requires further investiga-

tion and more simulation effort on for example photon/hadron separation with radio.

Eventbuilder

The event builder currently used in this simulation is based on several assumptions. Here we discuss some, which needs refinement for further detailed studies.

- The geometry of the air shower array takes the prediction into account that air showers emit stronger signals at larger angle between B-field and moving charge. Additional effects on the strength and the shape of the pulses are the distance from X_{max} of the shower and the beam width of the radio pulse. These are parameters which have to be implemented into the simulation to develop a radio detector with high veto efficiency as they will influence the detector geometry.

- The signal to noise suppression power of the cc-beam forming method strongly depends on the background noise distribution. Directive noise sources can lead to higher background values and decrease the detection efficiency of low signal strength. Real background data has to be implemented to consider this influence on the detector.

- The parametrization of the radio pulse extracted from the LOPES experimental results are only valid for E-W polarized antennas. The influence of their dipole antenna is not fully corrected and leads to small pulses for horizontal radio pulses. Simulations of the total E-field solve this problem.

- The X_{max} correction to South Pole conditions uses the assumption that the South Pole B-field is comparable to that at the LOPES site in Karlsruhe Germany. The X_{max} parametrization on the cosmic ray energy spectrum eliminates the influence of individual particles and fluctuations during the air showers propagation. Simulations like REAS2 use individual Corsika air showers and are able to simulate shower to shower fluctuations.

- The Landau fit on REAS2 predictions influences the frequency band of the predicted pulse.

- The real background at the South Pole in the low frequency band $< 30\,\mathtt{MHz}$ can be much higher than assumed. Reducing the frequency band of the detector can strongly influence the detectable pulse heights.

Triggered events of the 2010 setup could be the basis for a realistic background/event mixing. A next step could be the simulation of a huge parameter set of radio air shower signals with REAS3, which is currently under construction, in order to get a more realistic baseline for further detector simulations.

It should be mentioned that even the REAS2 simulation is limited to describe the measurements of currently existing radio air shower arrays. The current comparisons of LOPES results with REAS2 show REAS2 is correct within one order of magnitude [50]. The REAS3 simulation seems to describe the LOPES measurements much better. [30]

Current results

Figure 6.17 shows that the simulation predicts the best signal to noise ratio orthogonal to the B-field, where the signal to noise ratio is defined by:

$$S = \frac{Signal_{peak}^{CC}}{Noise_{RMS}^{CC}}, \tag{6.15}$$

where $Signal_{peak}^{CC}$ is the pulse hight of the cc-beam and $Noise_{RMS}^{CC}$ is the RMS of the background noise.

Due to the described assumptions of the simulation, predictions on the efficiency of the detector are not possible. On the basis of new simulations with REAS3, which is currently under construction, a more powerful simulation could be possible.

Hardware

The simulation already has the option to change the detection bandwidth, to implement antenna properties, amplification and to change the recorded frequency band. This can be the basis for describing a South Pole radio test array and for scaling its results in order to simulate a larger array. However, more important than simulation studies will be a real setup of a radio test array at the South Pole to investigate hardware opportunities and trigger strategies and to learn more about the radio frequency based detection under antarctic weather and infrastructure conditions.
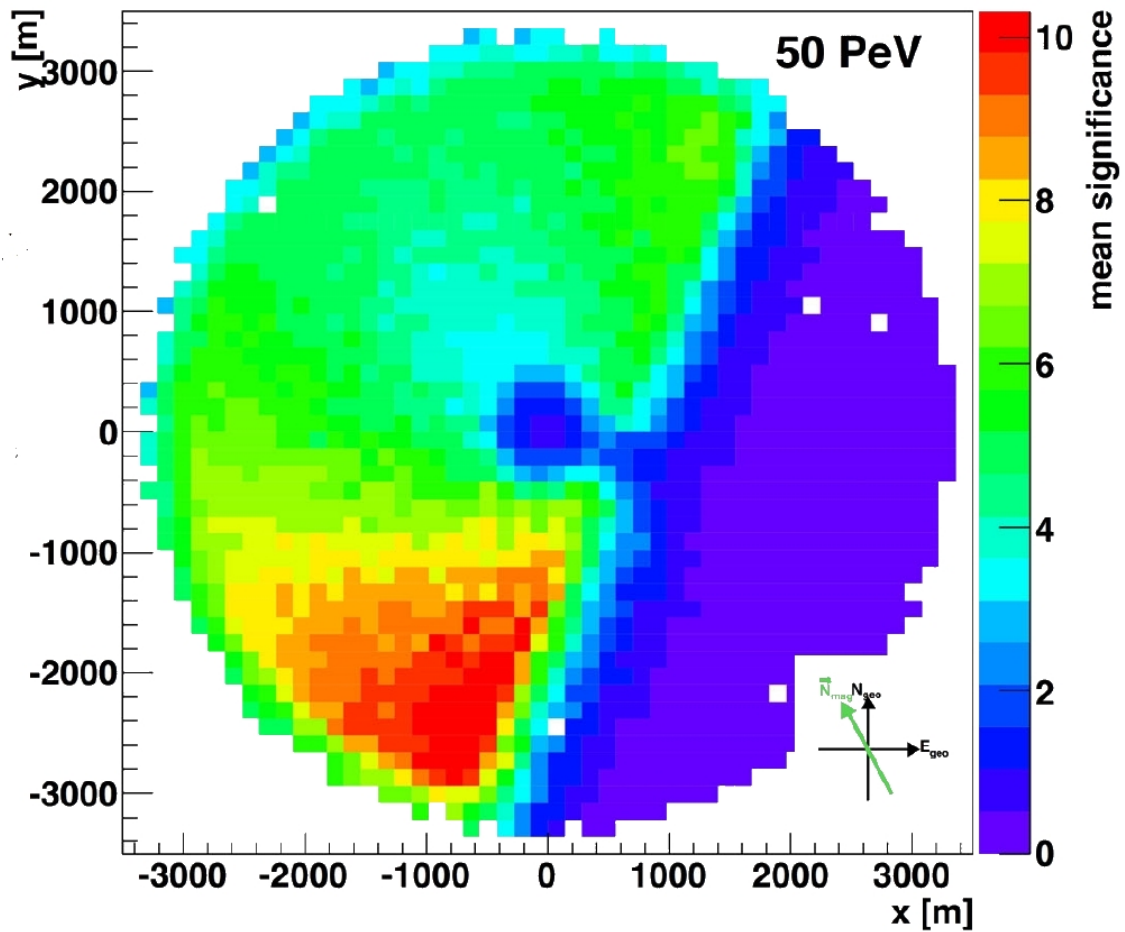
Figure 6.17: Significance plot of an exemplary array at the South Pole for air showers with 50 `PeV` primary energy. The most significant air showers have the shower axis orthogonal to the B-field [10].

Chapter 7

SUMMARY AND OUTLOOK

The presented air shower detection method using the geo-synchrotron emission at the South Pole could add a component to the IceCube observatory and thus lead to even more options to investigate particle physics, astroparticle physics and astrophysics. As explained in Chapter 6, a large radio air shower detector can significantly enhance the detection efficiency of IceCube for UHE neutrinos like the cosmogenic ones. The sensitivity on the neutrino flux could be increased by a factor of two, depending on the size and the geometry of the surface air shower array. Furthermore, the signal to noise ratio would increase dependent on the detector efficiency.

As the dominant part of geo-synchrotron emission is produced by the large number of electrons and positrons of an EAS in the region of X_{max}, a radio detector would add a component to the IceCube observatory which improves composition studies. The PMT based components, IceTop and IceCube, in a first step could help to develop and calibrate the radio detection system. This will make the radio array a complement of the IceCube observatory to get a multicomponent detector similar to systems known from accelerator particle physics experiments to get as much information as possible on the properties of the particle source.

Finally, a surface radio air shower detector at the South Pole could improve the IceCube observatory detecting all three known cosmic particle components at high energies, hadrons, photons, and neutrinos. The following blocks summarize the results of this thesis:

The first studies of the radio detection of the geo-synchrotron emission of air showers at the South Pole are described in this thesis. In Section 4, it is shown that the continuous background at the geographic South Pole is much lower than in Wuppertal and comparable to those from other deserts like Pampa Amarilla

in Argentina. Together with the properties of the Earth's magnetic field at the South Pole, we have shown that the continuous background at the South Pole is a promising low basis for the radio air shower detection in frequencies from 25-100 `MHz` and probably one of the most adequate in the world. Ongoing measurements at the South Pole during the Antarctic winter 2010 will help to investigate the amount of short pulsed RFI at the South Pole in the frequency band of interest and its properties.

The fat wire-dipole antennas (FWD) were found to be an adequate antenna for further research and development (R&D) studies at the South Pole. Its small cross section for wind, its moderate size and the simple construction are the basis of a receiving antenna in frequencies from 25-200 `MHz` under central Antarctic weather conditions. Several tests during an Antarctic winter at the South Pole with electronic components have shown that electronics which are commercial available (such as LNA, frequency filters and BIAS-Tees) work well under these conditions. It was shown that simple readout strategies with coincident recording oscilloscopes are already able to detect pulses. Reconstruction of the source is possible within 10 `ns`. A next step in testing components will be a flash-ADC based board to digitize the signals near the antenna.

The background measurements during the South Pole winter, the technological properties of antennas and electronics, as well as results from simulations were used to estimate the detectable cosmic ray flux of an eight antenna test array with RICE described in Chapter 6. It is based on an analog four out of six antenna trigger logic of FWD antennas deployed around the MAPO building. It was shown that air shower detection is feasible with this kind of detector with detection rates of one per day.

The altitude of about 2800 `m` at the South Pole, its atmosphere as well as the magnetic field inclination and strength were implemented in a field strength simulation of radio signals from air showers. CORSIKA-simulated air showers were the basis for these REAS2 simulations. The resulting pulses were corrected for the properties of a receiving system at the South Pole and pulse heights of radio signals from air showers in a FWD antenna were estimated, as described in Chapter 5. It was shown that air shower detection of geo-synchrotron pulses will be possible with the current equipment at the South Pole.

A simulation effort of a large radio air shower array is described to explain

the idea of future radio detection strategies. First trials with cc-beam techniques based on simple pulse parameterization indicate that a radio air shower array is able to detect air showers down to 10^{15} eV (Sec. 6.2). To improve this simulation effort, a more realistic parametrization of radio signals from air showers is required. The continuous background from measurements at the South Pole have to be implemented. After the implementation of digitization techniques of a test array at the South Pole the simulation could first be compared to real detector systems and later be a powerful instrument for simulation and development of a large surface radio air shower detector array at the South Pole.

Broad band radio techniques require to be a cost efficient method for air shower detection. 40 years after Jelleys discovery of radio emission from EAS, todays' technology of fast digitization and data storing give this technique new strength to get a powerful instrument complementing the limited number of currently existing CR detector strategies which are mostly dependent on photo multipliers. This thesis contains a study of the radio air shower detection technique from the perspective to complement IceCube to a multi component cosmic particle detector for moderate- and high- and ultra-high energies.

Appendix A

PROPERTIES OF ANTENNAS

This chapter gives a very short introduction into antenna properties. The interested reader is recommended to read e.g. [70] and [33].

A.1   Antenna Zones

To describe the properties of our receiving antenna we are using predictions not valid in the near field of an antenna. One distinguishes three different cases of Antenna zones, the near field, the intermediate case and the far field. All zones are defined relative to an emitting antenna. Figure A.1 shows the three different Antenna zones of a dipole antenna.

- The far field region is defined to be the distance r from the antenna where the observer sees the electromagnetic waveform to be planar ($\mathbf{E}\|\mathbf{B}$ with no phase difference) . This is hard to define, as with accurate time measurements it is always possible to reconstruct the wavefront is radial. However, this approximation is valid for the geo-synchrotron radio emission of air showers, as long as X_{max} is far enough away from the observing antenna, as most of the signal is produced there. The minimal distance from the antenna where fare field predictions are valid is $r > \frac{\lambda}{2\pi}$ and $D < \lambda$, where λ is the wavelength of the signal and D is the maximal dimension of the antenna. In this case the time difference between wavefront arrivals is negligible to the signals wavelength. In the case $D > \lambda$, r should be $r = 2\frac{D^2}{\lambda}$. Otherwise we reach the region where the dimensions of the antenna influence the measurement.

- The intermediate field region is defined to be the region, where the position of the emitter can be reconstructed to one point. Thus the observed field is circular. This can be distinguished from the near-field, if $D > \lambda$.
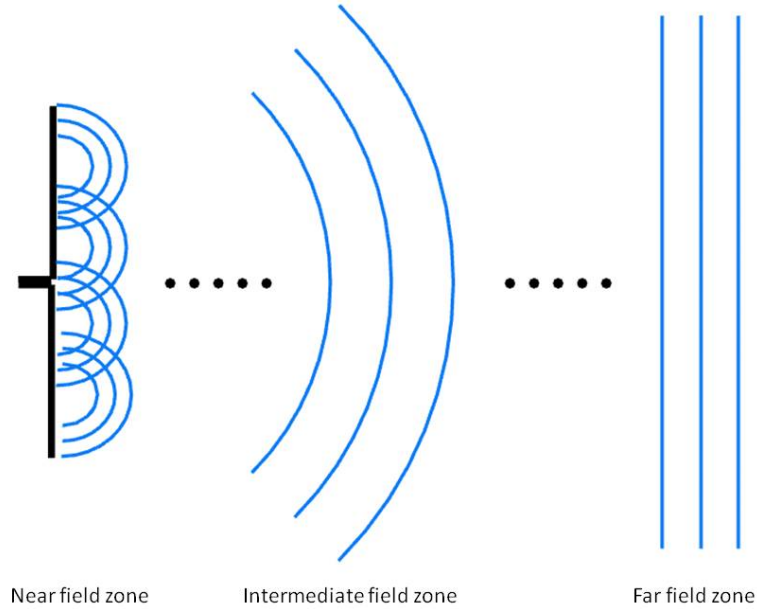
Figure A.1: Schematic of the antenna emission zones of a dipole antenna.

- The near field region is at distances from the antenna, where parts of the antenna can be seen as individual emitters. In this region the geometry of the antenna strongly influences the observed signal. In this region the phase of the received signal can strongly vary within small distances, like for the signal received from the VLF 4.4.3. In this region values like the antenna gain are not valid.

A.2   Outputpower of an Antenna

This is a short theoretical description how to get the output power P_{out} of an antenna in an electrical Field $\mathbf{E}$.
The energy flux of an electromagnetic field is described by the Poynting vector $\mathbf{S}$ for free space propagation:

$$\mathbf{S} = \mathbf{E} \times \mathbf{H}, \tag{A.1}$$

where $\mathbf{E}$ is the electrical and $\mathbf{H}$ the auxiliary magnetic field. If the emitting radio source is far away from the receiving antenna in terms of the wavelength, the far field approximation for the frequency band is valid. Using SI units, the impedance

of free space is defined by $\tilde{Z}$:

$$\tilde{Z} = \frac{|\mathbf{E}|}{|\mathbf{H}|} = \sqrt{\frac{\mu_0}{\epsilon_0}} = \mu_0 c \approx 377\Omega. \tag{A.2}$$

Equation A.1 and equation A.2 lead to,

$$|\mathbf{S}| = S = \frac{1}{\mu_0 \cdot c} E^2. \tag{A.3}$$

Now the output power P_{out} of the receiving antenna is:

$$P_{ant} = A_{eff}(f, \theta, \phi) \cdot S, \tag{A.4}$$

where A_{eff} is defined by the geometry of the antenna type used and depends on the frequency f, the zenith angle θ and the azimuth ϕ. A_{eff} is typically described by the antenna gain $G(f, \theta, \phi)$. G is commonly defined in `dBi` which is `dB` in relation to an isotropic radiator with the output power $\tilde{P}$.

$$\tilde{P} = \frac{P_{tot}}{4\pi r^2}, \tag{A.5}$$

where r is the distance of the emitter to the receiver and P_{tot} the emitting power. This leads for A_{eff} to:

$$A_{eff} = \frac{\lambda^2}{4\pi} \cdot G(f, \theta, \phi). \tag{A.6}$$

Equation A.6 inserted into equation A.4 lead to equation 4.4. Values for $G(f, \theta, \phi)$ result from antenna simulations.

Appendix B

THE DATA FORMAT OF RICE

RICE data is stored in ASCCII-files, as a part of the IceCube data transfer. The data can be found in /data/exp/RICE@data.wisc.edu . The waveforms are stored in files named data-YYYYMMDDSSSSS-test-XX.dat. YYYY is the year (e.g. 2009), MM the Month (e.g. 08), DD the day (e.g. 27) and SSSSS the second of the day, where the whole run started. The data files of each run are listed by XXX, staring with 1 and ending with 999. There is no leading 0. Each data file contains 10 "Run-Loops". Each "Run-Loop" is starting with "Forced Trigger" runs, to set the absolute threshold of the in Ice channels and the dynamic range of the oscilloscopes. The dynamic range is set to 32 times the RMS of the Forced Trigger sweep in volts. The threshold for each channel is set 6 times above this RMS. After that data is taken for maximal 10 events or 10 minutes before the next "FORCED TRIGGER" run is induced.

Figure B.1 shows the header of each event in a data file. The "Event Number" gives each event of a run a number starting with 1. After that the event time is stored in Day, Year, Universal Time and msec. The last more interesting information is the channels, which were part of the trigger (in the case of the Force Trigger every channel was participating).

```
Event number: 1
Year 2009 Day 62 Universal  Time 04:36:17  mksec count.    650158.9
DAQ PC date and time: Tue, Mar 03, 2009   5:36:16 PM
Run type: Hardware Trigger Measurement
Description:2007-data-taking
***Scope Parameters***
Trigger source: Auxiliary
Trigger type: hardware
Y-range: 2.400000E+0
Y-offset: 0.000000E+0
T-range: 5.000000E-7
T-delay: 0.000000E+0
Active channels:
1st scope: =1111
2nd scope: =1111
3d scope: =1111
4th scope: =1111
5th scope: =1111
6th scope: =1100
Number of samples: 8192
***Trigger, veto and prescale settings***
Trigger mode: FORCED TRIGGER
Discriminator #1 level: -7.500000E-1V
Discriminator #2 level: -1.000000E-1V
Trigger conditions: Generic
Veto conditions:  veto if any of the following is true
    A: exactly following channels (0:20):  0100100001001000000
    B: exactly following channels (0:20):  0101100001001000000
    C: exactly following channels (0:20):  1100001000001000000
    D: inclusive time-ordered channels:  <none>
    E: inclusive time-ordered channels:  <none>
    F: inclusive time-ordered channels:  <none>
    G: surface veto:    at least 4 of the channels 26   27   28
Prescale factors:
    General events     1
    Veto events        4
    External trigger 1  1
    External trigger 2  1
303 analysis: yes
303 save option: do not save 303 events
303 analysis channel 6
303 analysis segment length 3
303 analysis integration width 1024
303 analysis threshold 7.000000E+0
Hardware Surface Veto is enabled
HSV ON time in munites: 3000
HSV OFF time in munites: 0
***Event Summary***

Event is classified as Unbiased event
303 analysis results:No 303 detected
HSV board information based on hits in chan 26-29:
      this is an unbiased event, no HSV info saved
Number of hits in event (from TDC): 32
Full hit list:
Channel 0   time 222.5 ns
Channel 1   time 209.5 ns
Channel 2   time 213.0 ns
Channel 3   time 217.5 ns
Channel 4   time 213.0 ns
Channel 5   time 173.0 ns
Channel 6   time 219.0 ns
Channel 7   time 195.0 ns
Channel 8   time 219.5 ns
Channel 9   time 192.0 ns
Channel 10  time 207.0 ns
Channel 11  time 212.0 ns
Channel 12  time 198.0 ns
Channel 13  time 195.0 ns
Channel 14  time 216.0 ns
Channel 15  time 222.0 ns
Channel 16  time 150.0 ns
Channel 17  time 147.5 ns
Channel 18  time 134.0 ns
Channel 19  time 161.0 ns
Channel 20  time 136.0 ns
Channel 21  time 149.0 ns
Channel 22  time 150.0 ns
Channel 23  time 138.0 ns
Channel 24  time 149.5 ns
Channel 25  time 148.5 ns
Channel 26  time 166.5 ns
Channel 27  time 144.0 ns
Channel 28  time 138.0 ns
Channel 29  time 129.5 ns
Channel 30  time 139.0 ns
Channel 31  time 142.0 ns
HSV is ON
Live time statistics since the last saved event(303 time excluded):
   Live time, ms: 0.0
   Total (run) time, ms: 0.0
   Livetime fraction: NaN
True Vertex: -9.990000E+2   -9.990000E+2    -9.990000E+2
True Momentum: -9.990000E+2   -9.990000E+2   -9.990000E+2
***RICE DAQ version*** v2.11, Labview 6.0 , Jan 2009.
-------------------------------------
```

Figure B.1: The first part of each event in a data file lists is these two columns describing the properties of the event.

After the waveforms of the oscilloscopes are summarized staring with "————— —Waveform from channel 1" like in Figure B.2. The later waveforms of one event start with "—————Waveform from channel X scY" where the X is the number of the channel (1-4) of oscilloscope Y. The first leading numbers of each waveform report the oscilloscope settings. The first number is the readout time offset to the event time in seconds. The second number is the time length of one bin in seconds. The third number is the offset of the data values in Volts. The fourth number is the Voltage per ADC bin in Volts. The following numbers are the ADC values of the full waveform. It is 8194 numbers with values from -2047 to 2048 in equidistant binning.

```
---------------Waveform from channel 1        ---------------Waveform from channel 1 sc2
  -2.49100E-7                                   -2.49370E-7
   1.00000E-9                                    1.00000E-9
   0.00000E+0                                    0.00000E+0
   7.38189E-5                                    3.07579E-5
-51                                           452
64                                            128
114                                           -37
34                                            -426
45                                            -57
-33                                           158
-112                                          257
64                                            24
209                                           -121
126                                           -37
16                                            -162
-268                                          -144
177                                           363
64                                            128
-51                                           82
126                                           -107
-82                                           -342
64                                            27
0                                             323
0                                             128
-19                                           -162
34                                            -79
209                                           195
34                                            -462
-19                                           -121
-27                                           505
-112                                          323
```

Figure B.2: Every list of waveforms in a data file starts with "Waveform from channel 1" the waveform from channel 1 oscilloscope 1. After that an other waveform starts with "channel X sc Y". The first four numbers are not part of the waveform itself. The first number is the time offset to the event time in seconds, the second is the time binning in seconds, the third number is the offset in Voltage of the oscilloscope and the fourth number is the Voltage per ADC bin.

Appendix C

DISCRETE FOURIER TRANSFORMATIONS

Basic Equations

Consider a set of N real numbers $X_j \in \mathbb{R}$ ($j = 0 \ldots N-1$). We define two new sets $\tilde{X}_j \in \mathbb{C}$ and $Y_j \in \mathbb{C}$ ($j = 0 \ldots N-1$) of N complex numbers each:

$$\tilde{X}_j := \sum_{k=0}^{N-1} X_k e^{-2\pi i \frac{jk}{N}} \tag{C.1}$$

$$Y_j := \sum_{k=0}^{N-1} \tilde{X}_k e^{2\pi i \frac{jk}{N}} = \sum_{l=0}^{N-1} X_l \sum_{k=0}^{N-1} e^{2\pi i \frac{k(j-l)}{N}} = \sum_{l=0}^{N-1} X_l N \delta_{jl} = N X_j \tag{C.2}$$

Since $X_j \in \mathbb{R}$ the following relation holds:

$$\tilde{X}_{N-k} = \tilde{X}_k^* \tag{C.3}$$

so that there are only $\frac{N}{2} + 1$ independent values $\tilde{X}_j$ (For simplicity we assume N to be even).

Continuous Fourier Transform

The continuous Fourier transform $\tilde{f} : \mathbb{R} \to \mathbb{C}, \omega \mapsto \tilde{f}(\omega)$ of a real function $f : \mathbb{R} \to \mathbb{R}, t \mapsto f(t)$ is defined as:

$$\tilde{f}(\omega) = \frac{1}{\sqrt{2\pi}} \int_{-\infty}^{\infty} dt\, f(t) e^{-i\omega t} \tag{C.4}$$

with the inverse transform

$$f(t) = \frac{1}{\sqrt{2\pi}} \int_{-\infty}^{\infty} d\omega \, \tilde{f}(\omega) e^{i\omega t} \tag{C.5}$$

Since $f(t) \in \mathbb{R}$ the following relation holds

$$\tilde{f}(-\omega) = \tilde{f}(\omega)^* \tag{C.6}$$

and only non-negative frequencies ω have to be considered.

Energy conservation   It is worth noticing that the total energy in the signal in the time and freqeuncy domain are equal (Parseval's theorem):

$$\int_{-\infty}^{\infty} dt \, |f(t)|^2 = \int_{-\infty}^{\infty} d\omega \, |\tilde{f}(\omega)|^2 \tag{C.7}$$

Discrete Fourier Transform

Now consider the case of a digitized signal with N samples U_j recorded at sampling intervals Δt. Then the total length of the waveform is $T = (N - 1)\Delta t$, and the Nyquist frequency is $f_{\max} = \frac{1}{2\Delta t}$. The frequency resolution is $\Delta f = \frac{f_{\max}}{N/2} = \frac{1}{N\Delta t}$.

In comparison with (C.4) we define the discrete Fourier transform (DFT) of U_j to be:

$$\tilde{U}_j := \Delta t \sum_{k=0}^{N-1} U_k e^{-2\pi i \frac{jk}{N}} \tag{C.8}$$

Then the inverse transform is given by (compare to (C.5))

$$U_j := \Delta f \sum_{k=0}^{N-1} \tilde{U}_k e^{2\pi i \frac{jk}{N}} = \Delta f \, \Delta t N U_j = U_j \tag{C.9}$$

where for the intermediate steps equations (C.2) and $\Delta t \Delta f = \frac{1}{N}$ were used.

The unit of the Fourier coefficients $\tilde{U}_j$ is then (if U_j is measured in Volts): $[\tilde{U}_j] = \mathrm{Vs} = \frac{\mathrm{V}}{\mathrm{Hz}}$.

One should notice that the Fourier coefficients $\tilde{U}_j$ obviously depend on Δt and N so they are not a good quantity to compare different measurements or systems.

Energy conservation Notice that also in the discrete case energy is conserved (compare to (C.7)):

$$\Delta t \sum_{j=0}^{N-1} |U_j|^2 = \Delta f \sum_{j=0}^{N-1} |\tilde{U}_j|^2 \tag{C.10}$$

Power Spectral Density

The energy E of the recorded signal is given by (C.10):

$$E = \Delta f \sum_{j=0}^{N-1} |\tilde{U}_j|^2 \tag{C.11}$$

If $T = (N-1)\Delta t$ is the length of the signal the average power P is given by

$$P = \frac{E}{T} = \frac{\Delta f}{(N-1)\Delta t} \sum_{j=0}^{N-1} |\tilde{U}_j|^2 \approx \frac{2\Delta f}{(N-1)\Delta t} \sum_{j=0}^{N/2} |\tilde{U}_j|^2 \tag{C.12}$$

where in the last step (C.3) was used. For a continuous signal (e.g. noise) P is independent of the length T of the recording.

So the power P_j in the j-th freqeuncy bin of width Δf is

$$P_j = \frac{2\Delta f |\tilde{U}_j|^2}{(N-1)\Delta t}, \quad (j = 0 \ldots N/2) \tag{C.13}$$

The power spectral density PSD_j is defined as the power per unit frequency, so

$$PSD_j = \frac{P_j}{\Delta f} = \frac{2|\tilde{U}_j|^2}{(N-1)\Delta t}, \quad (j = 0 \ldots N/2) \tag{C.14}$$

which is independent of both the sampling rate Δt and the number of samples N (or equivalently Δf and N).

The unit of the power spectral density is (if U_j is measured in Volts) $[PSD_j] = V^2 s = \frac{V^2}{Hz}$.

Numerical calculation The FFTW algorithm which is e.g. used in ROOT calculates DFTs using (C.1). So when one gets values $\tilde{X}_j$ from such a calculation the PSD must be calculated as

$$PSD_j = \frac{2|\Delta t \tilde{X}_j|^2}{(N-1)\Delta t} = \frac{2\Delta t |\tilde{X}_j|^2}{(N-1)} \left(= \frac{|\tilde{X}_j|^2}{f_{\max}(N-1)} \right) \tag{C.15}$$

Be careful: There are several programs out there which do not calculate $\tilde{X}_j = \sum_{k=0}^{N-1} X_k e^{-2\pi i \frac{jk}{N}}$ but $\tilde{X}_j = \frac{1}{\sqrt{N}} \sum_{k=0}^{N-1} X_k e^{-2\pi i \frac{jk}{N}}$ or use even other normalization factors, so that (C.15) has to be adapted accordingly.

Relation between PSD and Signal RMS

If the mean value μ of a signal is zero:

$$\mu = \frac{1}{N} \sum_{j=0}^{N-1} U_j = 0 \tag{C.16}$$

then the standard deviation σ^2 of the signal is given by

$$\begin{aligned}
\sigma^2 &= \frac{1}{N} \sum_{j=0}^{N-1} |U_j|^2 = \frac{1}{N} \frac{\Delta f}{\Delta t} \sum_{j=0}^{N-1} |\tilde{U}_j|^2 \approx \frac{2}{N} \frac{\Delta f}{\Delta t} \sum_{j=0}^{N/2} |\tilde{U}_j|^2 \\
&= \frac{2}{N} \frac{\Delta f}{\Delta t} \sum_{j=0}^{N/2} \frac{(N-1)\Delta t PSD_j}{2} = \frac{N-1}{N} \Delta f \sum_{j=0}^{N/2} PSD_j \\
&\approx \Delta f \sum_{j=0}^{N/2} PSD_j
\end{aligned}$$

So the integral over the power spectral density is equal to the standard deviation (RMS) in the time domain.

List of Figures

List of Tables

Bibliography

[1] J. Abraham, P. Abreu, M. Aglietta, C. Aguirre, D. Allard, I. Allekotte , et al., for the Pierre AUGER Collaboration, "Extending the Search for Neutrino Point Sources with IceCube above the Horizon", Astropart. Phys., 29, 188, (2008).

[2] J. Abraham, P. Abreu, M. Aglietta, C. Aguirre, D. Allard, I. Allekotte, et al., for the Pierre AUGER Collaboration, "Measurement of the Depth of Maximum of Extensive Air Showers above 10^{18} eV", Phys. Rev. Lett. 104, 091101, (2010).

[3] T. Antoni, et al., "The Cosmic-Ray Experiment KASCADE". Nucl. Instr. & Meth. 513, 490-510, (2003).

[4] D. Ardouin et al., "Radio-detection signature of high-energy cosmic rays by the CODALEMA experiment". Nuc. Instr. Meth. A, 555, 148, (2005).

[5] S.W. Allen, R.W. Schmidt, A.C. Fabian, "Cosmological constraints from the X-ray gas mass fraction in relaxed lensing clusters observed with Chandra". MNRAS 334, L11, (2002).

[6] R.A. Alper, R.C. Herman, "On the Relative Abundance of the Elements". Phys. Rev. 74, 1737, (1948).

[7] T. Asch, "Self-Triggering of Radio Signals from Cosmic Ray Air Showers". PhD thesis at the Institut für Kernphysik at Forschungszentrum Karlsruhe, (2007).

[8] S.H. Neddermeyer and C.D. Anderson, "Note on the nature of Cosmic-Ray Particles". Phys. Ref. 51, pp. 884-886, (1937).

[9] G.A. Askarayan, "Coherent Radio Emmission from Cosmic Showers in Air and in Dense Media". JETP 21, 658, (1965).

[10] S. Böser, private communication, February (2010).

[11] R. Beck, A. Brandenburg, D. Moss, A. Shukurov,D. Sokoloff, "Galactic Magnetism: Recent Developments and Perspectives". ARA&A 34, 155,(1996)

[12] J. Benjamin, et al., "Cosmological constraints from the $100 - deg^2$ weak-lensing survey". MNRAS, 381, 702, (2007).

[13] D.J. Bird, et al., "The cosmic-ray energy spectrum observed by the Fly's Eye". ApJ vol. 424, no. 1, p.491-502, (1994).

[14] R. Cowsik and L. W. Wilson, "The "Nested Leaky Box" model for galactic cosmic rays". Ibid, 2, 659, (1975).

[15] L.G. Dedenko, et al., "Prospects for radio-wave and acoustic detection of ultra- and superhigh-energy cosmic neutrinos (cross sections, signals, thresholds)". Phys. Part. Nucl. 29, 266, (1998).

[16] R. Engel, D. Seckel, T. Stanev, "Neutrinos from propagation of ultrahigh energy protons". Phys. Rev. D 64, No9, p. 093010, (2001).

[17] H. Falcke et al. -LOPES collaboration, "Detection and imaging of atmospheric radio flashes from cosmic ray air showers". Nature 435, 313-316, (2005).

[18] E. Fermi, Physics Review 75, On the Origin of the Cosmic Radiation, pp. 1169-1174, (1949).

[19] T.K. Gaisser and A.M. Hillas, *Proceedings of the 15th ICRC*, Vol. 8, p. 353, (1977).

[20] K. Greisen, "End to the Cosmic-Ray Spectrum?". Phys. Rev. Letters, Vol. 16, No. 17, pp. 748 750, (1956).

[21] H. Gemmeke, et al., "Advanced Detection Methods of Radio Signals from Cosmic Rays for KASCADE Grande and Auger". International Journal of Modern Physics, A, 21, 242, (2006).

[22] P.W. Gorham, for the ANITA collaboration, "Observations of the Askarayan Effect in Ice". arXiv:hep-ex/0611008v2, (2007).

[23] P.W. Gorham, et al., "The Antarctic Impulsive Transient Antenna Ultra-high Energy Neutrino Detector: Design, Performance, and Sensitivity for 2006-2007 Balloon Flight". arXiv:atro-ph/0812.1920v1, (2008).

[24] D. Heck, et al., "CORSIKA: a Monte Carlo code to simulate extensive air showers". FZKA Report 6019, (1998).

[25] V.F. Hess, "Über Beobachtungen der durchdringenden Strahlung bei sieben Freiballonfahrten". Physikalische Zeitschrift, Vol 13,pp. 1084-1091, 1912.

[26] A. Horneffer, "Measuring Radio Emission from Cosmic Ray Air Showers with a Digital Radio Telescope". Dissertation at the Mathematisch-Naturwissenschaftlichen Fakultät der Rheinischen Friedrich-Willhelms-Universität Bonn, (2006).

[27] T. Huege and H. Falcke. "Radio emission from cosmic ray air showers". A & A, Vol. 430, No. 3, pp. 778-798, (2005).

[28] T. Huege and H. Falcke ,"Radio emission from cosmic ray air showers: Simulation results and parametrization". Astropart. Phys., 24, 116, (2005).

[29] T. Huege, R. Ulrich, and R. Engel, "Monte Carlo simulations of geosynchrotron radio emission from CORSIKA-simulated air showers". Astropart. Phys., Vol. 27, pp. 392-405 (2007).

[30] T. Huege, private communication, March (2010).

[31] A. Ishihara for the IceCube Collaboration, ICRC (2007).

[32] H.T. Janka, T. Eberl, M. Ruffert, C.L. Fryer, "Black Hole- Neutron Star Mergers as Central Engines of Gamma-Ray Bursts". Astroph. J. Lett. 527, (1999).

[33] J.D. Jackson, Classical Electrodynamics, 2nd edition. (JohnWiley & Sons, New York), (1975).

[34] Jiwoo Nam for the ANITA Collaboration, "Possible Impulsive Radio Signals from Ultra-high Energy Extensive Air Showers Detected by the ANITA Experiment". ICRC (2009).

[35] O.E. Kalashev, V.A. Kuzmin, D.V. Semikoz, and G. Sigl, "Ultrahigh-energy neutrino fluxes and their constraints". Phys. Rev. D 66, 063004, (2002).

[36] K. Kamata and J. Nishimura. "The Lateral and Angular Strucure Functions of Electron Showers". Progress of Theoretical Physics Supplements, Vol. 6, pp. 93 155, (1958).

[37] R.A. Knop, et al. "New Constraints on λ_M, λ_Ω, and w from an Independent Set of 11 High-Redshift Supernovae Observed with the Hubble Space Telescope". ApJ, 598, 102, (2003).

[38] A. Karle, for the IceCube Collaboration, "IceCube"', *Proceedings of the 31th ICRC*, (2009).

[39] N.N. Kalmykov and S.S. Ostapchenko, "Physics of Atomic Nuclei". 56:346-353, (1993).

[40] R. Klebesadel, et al. "Observations of Gamma-Ray Bursts of Cosmic Origin". Astrophysical Journal 182: L85, (1973).

[41] S. Klepser, "Reconstruction of Extensive Air Showers and Measurement of Cosmic Ray Energy Spectrum in the Range of 1-80 PeV at the South Pole", Dissertation at the Methematisch-Naturwissenschaftlichen Fakultät I Humbolt Universität zu Berlin, (2008).

[42] S. Klepser, private communication, (18.12.2009).

[43] I. Kravchenko, G.M. Frichter, D. Seckel, G.M. SpiczaK, et al. "Performance and Simulation of the RICE detector". Astropart. Phys., Vol. 19, Pages 15-36, (2003).

[44] H. Landsman for the IceCube Collaboration, "AURA -Aradio frequency extension to IceCube". arXiv:0811.2520v1, Arena (2008).

[45] K. Lange, K.H. Löcherer, "Gundlach Taschenbuch der Hochfrequenztechnik", 5. Auflage, Springer-Verlag Berlin u.a., ISBN 3-540-54714-2, (1992).

[46] M.S. Longair, High Energy Astrophysics, vol. 2. Cambridge University Press, second ed., (1994).

[47] A. MacFadyen, S. E. Woosley, "Collapsars - Gamma-Ray Bursts and Explosions in Failed Supernovae". Astroph. J. 524, p. 262, (1999).

[48] D.D. Marco and T. Stanev, "On the shape of the ultrahigh energy cosmic ray spectrum". Phys. Rev. D, Vol. 72, No. 8, p. 081301, (2005).

[49] P. Meszaros, "Gamma-Ray Bursts: Accumulating Afterglow Implications, Progenitor Clues, and Prospects". Science 291, January, pp. 79-84, (2001).

[50] S. Nehls, "Calibrated Measurements of the Radio Emission of Cosmic Ray Air Showers". PhD thesis at the Institut für Kernphysik at Forschungszentrum Karlsruhe, (2008).

[51] P. Miocinovic et al., "Tuning into UHE neutrinos in Antarctica: The ANITA experiment". eConf C041213 2516, (2004).

[52] G. Moliere, 1948, Z. Naturforsch., 3a, (1978).

[53] W.L. Poulsen, U.S. Inan, and T.F. Bell, "A multiple-mode three-dimensional model of VLF propagation in the earth-ionosphere waveguide in the presence of localized D region disturbances". J. Geophys. Res., 98, 1705-1717, (1993).

[54] A.A. Penzias and R.W. Wilson. "A Measurement of Excess Antenna Temperature at 4080 `MC/s`". AsJ, Vol. 142, pp. 419-421, (1965).

[55] V.S. Ptuskin , S.I. Rogovaya , V.N. Zirakashvili, L.G. Chuvilgin, G.B. Khristiansen, E.G. Klepach, G.V. Kulikov , A&A, 268, 726, (1993).

[56] J.P. Ralston, D.W. McKay and G.M. Frichter, "The Ultra High Energy Neutrino-Nucleon Cross Section". astro-ph/9606007, (1996).

[57] G.D. Reeves, T.E. Cayton, R.H. Friedel, K.L. McAdams, "Extreme Relativistic Electron Events and Their Associated Geomagnetic Activity". Solar Max 2000, EOS, p. S369, (2000).

[58] H.J.A. Rottgering , et al., "LOFAR-Opening up a new window on the Universe", ArXiv astro-ph/0610596, (2006).

[59] D.N. Spergel , et al., "Three-Year Wilkinson Microwave Anisotropy Probe (WMAP) Observations: Implications for Cosmology". ApJS, 170, 377, (2007).

[60] F.W. Stecker, C. Done, M.H. Salamon, and P. Sommers, "High-ernergy neutrinos from active galactic nuclei". Phys. Rev. Lett. 66, pp. 2697-2700, (1991).

[61] F.W. Stecker, "Note on high-energy neutrinos from active galactic nuclei cores". Phys. Rev. D, 72(10):107301, (2005).

[62] T.A. Thompson, P. Chang, E. Quataert, "Magnetar Spindown, Hyper-Energetic Supernovae, and Gamma Ray Bursts". Astroph. J. 611, (2004).

[63] H. Ulrich, et al. "Energy Spectra of Cosmic Rays in the Knee region". Nucl. Phys. B. Proceedings, Vol. 122, pp. 218-221, (2003).

[64] H. Ulrich, et al. "Indirect measurements around the knee – recent results from KASCADE" Int. J. of Mod. Phys. A20 6774-6777, (2005).

[65] J. Vandenbroucke, et al. "Measurement of acoustic properties of South Pole ice for neutrino astronomy", Nucl. Instr. and Meth. A, doi:10.1016/j.nima.2009.03.064, (2009).

[66] G.S. Varner et al."The large analog bandwidth recorder and digitizer with ordered readout (LABRADOR) ASIC", Nucl. Instr. Meth. A583 447, (2007).

[67] G. Zatsepin and V. Kuz'min. "Upper Limit of Cosmic Rays". Journal of Exp and Therm. Phys. Letters, Vol. 4, p. 78ff, (1956).

[68] O.C. Alkhofer , "Introduction to cosmic radiation", Verlag Carl Thiemig München, (1975).

[69] R.D. Blandford & J.P. Ostriker, ApJ, 221, L29, (1979).

[70] K. Rothammel, "Rothammels Antennenbuch". Franckh-Lomos Verlags-GmbH & Co., 11th edition, (1995).

[71] J.D. Jackson, "Classical Electrodynamics". 3nd edition, (1999).

[72] V.F. Petrenko, R.W. Withworth, "Physics of Ice", Oxford University Press, (1999).

[73] S. Yoshida and M. Teshima, "Energy Spectrum of Ultra-High Energy Cosmic Rays with Extra-Galactic Origin". Prog. Theor. Phys. 89, 833, (1993).

[74] http://www.auger.org/news/PRagn/about_AGN.html. (2010)

[75] http://icecube.wisc.edu. (2010)

[76] http://www-star.stanford.edu/~vlf/south_pole/south%20pole.htm. (2010)

Curriculum Vitae

PERSONAL DATA

Name: **Jan Auffenberg**

Address: Kluser Höhe 21

42119 Wuppertal

Germany

E-Mail: jauffenb@uni-wuppertal.de

Nationality: German

PROFESSIONAL ACTIVITIES

since 8/2006: Research assistant and Ph.D. student at the Bergische Universität Wuppertal, Germany, department for Astroparticle Physics (Head: Prof. Dr. Klaus Helbing).

5/2006–8/2006: Graduate assistant at the Institut für Kernphysik of the Westfälische Willhelms Universität Münster, Germany, for administration of computers (Head: Prof. Dr. Johannes Wessels).

1/2003–4/2006: Student assistent of the IVV4 (physiks department) for system administration of computers at the Westfälische Willhelms Universität Münster, Germany (contact person Dr. Wolfgang Zierau).

UNIVERSITY STUDIES

currently: Ph.D. student in astroparticle physics at the department
                    for Astroparticle Physics of the Bergische Universit"at
                    Wuppertal, Germany.

6/2006:   Graduation as German Diplom Physiker at the depart-
                    ment of Kern und Teilchenphysik of the Westfälische
                    Willhelms Universität Münster, Germany.

                    Title of thesis: "Direct Photons in Ultra Relativistic
                    Heavy d + Au Collisions with the PHENIX experi-
                    ment at RHIC" (Referee: Prof. Dr. Johannes Wessels,
                    Co-referee: Prof. Dr. Christian Weinheimer).

ALTERNATIVE CIVILIAN SERVICE

7/1998–9/1999   Intensive Care Unit of the Katholisches Krankenhaus
                    Lippstadt, Germany

EDUCATION

1998   Evangelisches Gymnasium Lippstadt, Germany
                    Graduation: Abitur (University-entrance diploma).

LANGUAGES

                    German, English, Latin.

Publications

IceCube

1. R. Abbasi et al.: Extending the search for neutrino point sources with IceCube above the horizon, submitted to Phys. Rev. Lett.

2. R. Abbasi et al.: Measurement of sound speed vs. depth in South Pole ice for neutrino astronomy, submitted to Astropart. Phys., arXiv:0909.2629 [astro-ph.IM].

3. R. Abbasi et al.: Search for muon neutrinos from Gamma-Ray Bursts with the IceCube neutrino telescope, submitted to Astrophys. J., arXiv:0907.2227 [astro-ph.HE].

4. R. Abbasi et al.: First neutrino point-source results from the 22 string IceCube detector, Astrophys. J. 701 (2009) L47, arXiv:0905.2253 [astro-ph.HE].

5. R. Abbasi et al.: Limits on a muon flux from neutralino annihiliations in the Sun with the IceCube 22-string detector, Phys. Rev. Lett. 102 (2009) 201302, arXiv:0902.2460 [astro-ph.CO].

6. R. Abbasi et al.: Determination of the atmospheric neutrino flux and searches for new physics with AMANDA-II, Phys. Rev. D 79 (2009) 102005, arXiv:0902.0675 [astro-ph.HE].

7. R. Abbasi et al.: Search for high-energy muon neutrinos from the "naked-eye" GRB 080319B with the IceCube neutrino telescope, Astrophys. J. 701 (2009) 1721, arXiv:0902.0131 [astro-ph.HE].

8. R. Abbasi et al.: The IceCube Data Acquisition System: Signal Capture, Digitization, and Timestamping, Nucl. Instrum. Meth. A 601 (2009) 294, arXiv:0810.4930 [physics.ins-det].

9. R. Abbasi et al.: Search for point sources of high energy neutrinos with final data from AMANDA-II, Phys. Rev. D 79 (2009) 062001, arXiv:0809.1646 [astro-ph].

10. R. Abbasi et al.: Solar energetic particle spectrum on 2006 December 13 determined by IceTop, Astrophys. J. 689 (2008) L65, arXiv:0810.2034 [astro-ph].

11. M. Ackermann et al.: Search for Ultra High Energy Neutrinos with AMANDA-II, Astrophys. J. 675 (2008) 1014, arXiv:0711.3022 [astro-ph].

12. A. Achterberg et al.: The Search for Muon Neutrinos from Northern Hemisphere Gamma-Ray Bursts with AMANDA, Astrophys. J. 674 (2008) 357, arXiv:0705.1186 [astro-ph].

13. A. Achterberg et al.: Detection of Atmospheric Muon Neutrinos with the IceCube 9-String Detector, Phys. Rev. D 76 (2007) 027101, arXiv:0705.1781 [astro-ph].

14. A. Achterberg et al.: Multiyear search for a diffuse flux of muon neutrinos with AMANDA-II, Phys. Rev. D 76 (2007) 042008, arXiv:0705.1315 [astro-ph].

15. A. Achterberg et al.: Search for neutrino-induced cascades from gamma-ray bursts with AMANDA, Astrophys. J. 664 (2007) 397, arXiv:astro-ph/0702265.

LOPES

1. Frequency spectra of cosmic ray air shower radio emission measured with LOPES Nigl, A. et al. - LOPES collaboration 2008, Astronomy & Astrophysics 488, 807-817

2. Direction identification in radio images of cosmic-ray air showers detected with LOPES and KASCADE Nigl, A. et al. - LOPES collaboration 2008, Astronomy & Astrophysics 487, 781-788

3. Amplified radio emission from cosmic ray air showers in thunderstorms Buitink, S. et al. - LOPES collaboration 2007, Astronomy & Astrophysics 467, 385-394

4. Radio emission of highly inclined cosmic ray air showers measured with LOPES Petrovic, J. et al. - LOPES collaboration 2007, Astronomy & Astrophysics 462, 389-395

PROCEEDINGS

1. J. Auffenberg, D. Besson, T. Gaisser, K. Helbing, T. Karg, A. Karle and I. Kravchenko: Study of electromagnetic backgrounds in the 25-300 MHz frequency band at the South Pole, in Proceedings of the 31st International Cosmic Ray Conference (2009).

2. J. Auffenberg, D. Besson, T. Gaisser, K. Helbing, T. Karg and A. Karle: A radio air shower detector as an extension for IceCube and IceTop, Nucl. Instrum. Meth. A 604 (2009) S53.

3. J. Auffenberg, T. Gaisser, K. Helbing, T. Huege, T. Karg and A. Karle: A radio air shower surface detector as an extension for IceCube and IceTop, in Proceedings of the 30th International Cosmic Ray Conference, Vol. 5 (2008) 917, arXiv:0708.3331 [astro-ph].

DIPLOMA THESIS

1. Jan Auffenberg. *Direct Photons in Ultra Relativistic Heavy d + Au Collisions with the PHENIX experiment at RHIC*. Diplomarbeit am Lehrstuhl für Physik, Prof. Dr. Johannes Wessels, Westfälische Willhelms Universität Münster, 2006.

Conference Talks

DPG 2007, Heidelberg, Germany
"Messung des niederfrequenten Radiountergrundes in Wuppertal, Argentinien und am Südpol im Hinblick auf Luftschauernachweiß""

DPG 2008, Freiburg, Germany
"Ein Radio-Luftschauerdetektor als Erweiterung für IceTop""

Arena 2008, Rome, Italy
"A radio air shower detector as an extension for IceCube and IceTop""

DPG 2009, München, Germany
"Langzeitradiountergrundmessungen am Südpol im Frequenzbereich von 1-500 MHz""

ICRC 2009, Lodz, Poland
"Study of electromagnetic background from 25-150MHz at the South Pole""

I had the chance to give talks in several countries and continents at collaboration meetings and workshops of IceCube, LOPES and AUGER like Argentina, USA, and European countries. I was visiting researcher in Madison (UW), Malargue (Pierre Auger experiment), South Pole (IceCube), and several German Universities and research centers.

Acknowledgment

The total number of people who helped me with this thesis is too big to not forget someone. Thus, my strategy to include all the people is quite simple: I just thank everybody who knew me during my thesis and is reading this acknowledgment. Those I did not include with this sentence will never know if you don't tell them... However, I have in particular to thank Professor Klaus Helbing, my doctor father, for enormous support. He answered me not only any physical question and focused me on the fundamental points, but was a great supervisor, too

Nearly the same importance has Dr. Timo Karg. He always had to listen to my daily questions and private stories, and is a patient listener with impressive knowledge in astroparticle physics.

I got a lot of support from an enormous number of other scientists:

- Professor Karl Heinz Kampert involved me into the LOPES experiment and the Auger radio effort. This was my main access to get started with radio air shower detection.

- Professor Dave Besson who allowed supported my large impact to the RICE experiment with my "surface radio stuff"; Professor Illya Kravchenko for a lot of answers on technical questions.

- Professor Albrecht Karle for political support as well as Professor Tom Gaisser.

- Thanks to Dr. Tim Huege gently providing the REAS2 simulation. He was very helpful to answer all my questions regarding the geo-synchroton mechanism.

- Dr. Julian Rautenberg. He always supported my Auger radio efforts.

- Andrew Laundrie who helped me to develop the FWD antenna.

- Dr. Sebastian Böser who did the "fast radio simulation effort" with me and gained the surface air shower detection idea at the South Pole a lot.

...and this is only a small fraction of the enormous number of scientists who helped me.

Many other members of the work group in Wuppertal, Karlsruhe and Madison would have to be mentioned.
Hagar Landsman and Perry Sandstrom are examples in Madison,- All Andreas', Benjamin, all the Daniels, and Daniel Kruppke-Hansen in particular, as scientist and friend, both Nils', Oana, Nicol, Jonas, Martin, and all the others from Wuppertal.
Both Andreas in Karlsruhe, Daniel, Thomas and Oliver as examples for people from Karlsruhe and the LOPES collaboration who helped me a lot.

This enumeration is wrong and incomplete...

In addition, there is a lot of friends who remembered me to enjoy life.

My parents are always great supporters of all my dreams and needs. My whole family deserves many thanks. That includes my grandmother, uncles and aunts and particularly Ruth, Helmut, Felix and Tobias.

And there is my wife. Having her at my side is the best thing in my life.

Selbständigkeitserklärung

Hiermit versichere ich, dass ich diese Arbeit nur unter Zuhilfenahme der angegebenen Quellen und Hilfsmittel selbständig angefertigt habe.

Ort, Datum	Jan Auffenberg